Three-dimensional local reference frames for precise neuroanatomical modeling

Dissertation

zur Erlangung des Grades eines

Doktors der Naturwissenschaften

der Mathematisch-Naturwissenschaftlichen Fakultät

und

der Medizinischen Fakultät

der Eberhard-Karls-Universität Tübingen

vorgelegt

von

Mythreya Mysore Seetharama

aus Mysore, Indien

2025

Tag der mündlichen Prüfung: 16.05.2025

Dekan der Math.-Nath. Fakultät: Prof. Dr. Thilo Stehle

Dekan der Medizinischen Fakultät: Prof. Dr. Bernd Pichler

1. Berichterstatter: Prof. Dr. Cornelius Schwarz

2. Berichterstatter: Prof. Dr. Marcel Oberlaender

Prüfungskommission: Prof. Dr. Marcel Oberlaender

Prof. Dr. Cornelius Schwarz

Prof. Dr. Andrea Burgalossi

Prof. Dr. Anna Levina

Erklärung / Declaration:

Ich erkläre, dass ich die zur Promotion eingereichte Arbeit mit dem Titel: “ Three-dimensional local reference frames for precise neuroanatomical modeling ” selbständig verfasst, nur die angegebenen Quellen und Hilfsmittel benutzt und wörtlich oder inhaltlich übernommene Stellen als solche gekennzeichnet habe. Ich versichere an Eides statt, dass diese Angaben wahr sind und dass ich nichts verschwiegen habe. Mir ist bekannt, dass die falsche Abgabe einer Versicherung an Eides statt mit Freiheitsstrafe bis zu drei Jahren oder mit Geldstrafe bestraft wird.

I hereby declare that I have produced the work entitled “ Three-dimensional local reference frames for precise neuroanatomical modeling ”, submitted for the award of a doctorate, on my own (without external help), have used only the sources and aids indicated and have marked passages included from other works, whether verbatim or in content, as such. I swear upon oath that these statements are true and that I have not concealed anything. I am aware that making a false declaration under oath is punishable by a term of imprisonment of up to three years or by a fine.

Norderstedt, den 06.06.2025 .....

Datum / Date Unterschrift / Signature

Abstract

Reference frames provide a method of registering anatomical and functional data collected across multiple specimens and experimental setups into a common coordinate system in order to perform further analysis. Global reference frames define a brain-wide coordinate system and are useful when studying multiple brain regions. However, when a precise neuroanatomical model of a specific brain region is required, the precision provided by the global reference frames is insufficient and thus we require local reference frames, where the region is modeled using its local anatomical landmarks. Such a 3D local reference frame has previously been developed for the rat barrel cortex that has been applied to model its geometric, cellular and morphological organization, culminating in the generation of a dense statistical connectome of the region which predicts the connectivity between neurons of the region. I, first developed an algorithm to detect putative synaptic contacts between *in vivo* labeled pairs of neurons and applied them to neuron pairs of the rat barrel cortex. The resulting number and distribution of putative synaptic contacts were in-line with the prediction of the connectome model, thus validating the model. Therefore, I extended the 3D local reference framing approach to the rat facial nucleus and applied it to obtain the organization of vibrissal motoneurons that innervate the intrinsic whisker muscles, which formed whisker row-specific slabs in the ventro-lateral facial nucleus. In order to extend the local reference framing approach to regions that lack salient anatomical features, I came up with a novel way to define a functional brain region: based on its synaptic distance from a terminal muscle. I validated the trans-synaptic spread of rabies virus using the facial nucleus reference frame, following its administration into an intrinsic whisker muscle. I defined the region spanned by rabies labeled neurons in the layer 5 of the motor cortex as vibrissal motor cortex and generated a 3D local reference frame of it. I applied the reference frame to delineate the cellular and morphological organization of the region. The precision of these 3D local reference frames - barrel cortex ($\pm 45\,\mu m$), facial nucleus ($\pm 60\,\mu m$) and vibrissal motor cortex ($\pm 70\,\mu m$) - were more than 6 times higher compared to the global reference frame.

Acknowledgments

First and foremost, I would like to thank Prof. Dr. Marcel Oberlaender for giving this opportunity to pursue my doctoral studies in his group and his continued support throughout the studies. His in-depth domain knowledge, unwavering focus and communication skills have been an inspiration.

I would like to thank my advisory committee, Prof. Dr. Cornelius Schwarz and Prof. Dr. Matthias Bethge, for their insightful comments and timely discussions.

I would like to thank Dr. David A. Slabik for performing the experiments and providing the morphological reconstructions as well as manual synapse ground truths for the putative synapse detection project; Alison Smyth for introducing me to the earlier efforts regarding the detection tool; Dr. Daniel Udvary for comparing the results of the detection tool with the statistical connectome model.

I would like to thank Dr. Jason M. Guest for performing experiments and providing all the data related to facial nucleus, including the data related to the cholera toxin-beta subunit and the trans-synaptic rabies virus tracings along with the manual markings of rabies labeled neurons; Dr. Arco Bast for suggesting the parameterization of facial nucleus with an ellipsoid.

I would like to thank Dr. Rajeevan T. Narayanan and the students (Maksims Ivanovs, Amir H. Kayvanjoo, Amina javadova) who aided in his effort, for providing the reconstructions of motor cortex morphologies; Aman Maharjan for providing the aligned 2D cortical contours as well as the aligned rabies landmarks, in addition to the aligned 2D contours of various cortical regions for comparison with the rabies labeled regions; Hyoungjun Park for developing algorithm for aligning 2D cortical contours.

I would also like to thank all the former and current members of Prof. Dr. Marcel Oberlaender's group for creating a friendly and stimulating environment. I will always cherish these memories.

Last but not the least, I would like to express gratitude from the depths of my heart to my family, specifically my wife, Vaishnavi Vaidyanathan; without her unconditional love, unwavering faith and constant support, I would not have been able to complete my doctoral studies.

Statement of Contributions

This thesis was carried out under the guidance of Prof. Dr. Marcel Oberlaender, who initially conceived the idea of developing a technique that detects putative synaptic contacts between *in vivo* labeled pairs of neurons. He also suggested the possibility of extending the local reference framing approach of the rat barrel cortex to other regions of the rat brain. I developed the algorithm to detect putative synaptic contacts between *in vivo* labeled pairs of neurons, as well as developed and analyzed local reference frames for two more regions of the rat brain. The anatomical data that I analyzed as part of my thesis were primarily generated within the lab by fellow lab members: Dr. David A. Slabik, Dr. Jason M. Guest and Dr. Rajeevan T. Narayanan. Other lab members who have contributed to my projects by providing data or discussions are Dr. Robert Egger, Dr. Daniel Udvary, Dr. Arco Bast, Alison Smyth, Aman Maharjan, Hyoungjun Park, Maksims Ivanovs, Amir H. Kayvanjoo and Amina Javadova. Dr. Guest carried out some of the experiments in collaboration with Elizabeth S. Wendel under the guidance of Prof. Peter L. Strick.

Detection of putative synapses between *in vivo* labeled pairs of neurons
I developed an algorithm to detect proximity zones, where the distance between the axon of a neuron and the dendrite of another neuron is less than 4 µm, given the 3D digital reconstructions of their morphologies. I developed software to crop 3D image stacks having volumes of 10 μm^3 around each detected proximity zone, in order to inspect whether there is an overlap between spine and axon (touch point) or an overlap between spine and bouton (putative synapse). I determined the optimal proximity radius to be 4 µm through systematic testing. I generated consensus ground truth along with Dr. Slabik, in order to evaluate the accuracy, false positive and false negatives of the detection method. I developed an algorithm to compute the path lengths and branch orders of the putative synapses from their pre and post synaptic soma locations. I analyzed the cell-type specific putative synapse patterns.

Dr. Slabik, under the guidance of Dr. Narayanan, carried out the experiments, wherein, he performed the *in vivo* Biocytin filling of multiple neurons within an

animal and repeated the procedure for several rats. Dr. Slabik performed the subsequent histology, slicing and high resolution confocal imaging. Further, he reconstructed the 3D neuronal morphologies using the algorithm developed by Prof. Dr. Oberlaender (Oberlaender, Bruno, Sakmann, & Broser, 2007) and the Filament editor extension in Amira software (Dercksen, Hege, & Oberlaender, 2014). He registered the resulting 3D morphologies to the standard model of the barrel cortex using registration routines developed by Dr. Egger (R. Egger, Narayanan, Helmstaedter, de Kock, & Oberlaender, 2012). Dr. Slabik has reported the entire method in his thesis (Slabik, 2018). Alison Smyth introduced me to the earlier attempt of detecting putative synapses and also aided Dr. Slabik in reconstructing the neuron morphologies. Dr. Udvary compared the number and distribution of the putative synapses with the connectivity predictions made by the statistical connectome model of the rat barrel cortex (R. Egger, Dercksen, Udvary, Hege, & Oberlaender, 2014; Udvary et al., 2022).

3D local reference frame of the rat facial nucleus I identified the rat facial nucleus (FN) using the diameter of the somata of the FN neurons, which are bigger than their surrounding neurons. I contoured the FN in each brain stem section image and aligned section images to each other using the mid-line. I marked all FN somata; marked all vibrissal motoneuron (vMN) somata that were labeled by the mono-synaptic tracer injections into the intrinsic whisker muscles. I approximated the FN geometry by fitting an ellipsoid, quantified the variability of the FN across animals in terms of their volume, extent and orientation of principal axes and number (density) of neurons. I quantified the precision of FN geometry and generated an average (standard) model of the rat FN, which is its 3D local reference frame. I developed registration routines to register anatomical data of the FN from different animals and experiments into the reference frame. I applied the FN reference frame to combine data from different experiments, where the vMNs were labeled by injecting mono-synaptic tracers into specific whisker muscles. I analyzed the whisker row-specific organization of vMNs in the rat FN and generated standard row-specific vMN slabs under the guidance of Prof. Dr. Oberlaender. I reconstructed the vMN dendrite morphologies labeled by the rabies virus, with help from colleagues and registered these morphologies to the FN reference frame.

I analyzed their organization with respect to vMN row-specific slabs and the FN with guidance from Prof. Dr. Oberlaender.

Dr. Guest carried out all the experiments. He injected the mono-synaptic (cholera toxin beta subunit) as well as the trans-synaptic (N2c strain of the rabies virus) tracers into the intrinsic whisker muscle of rats. The rabies virus experiments were carried out in collaboration with Wendel under the supervision of Prof. Strick. Dr. Guest performed histology, slicing and high resolution imaging of brain stems. He also performed the high resolution imaging for reconstruction of rabies labeled dendrites. Him and Prof. Dr. Oberlaender identified the neurons that were labeled by the rabies virus in the brain stem of the second order animals and identified the brain stem regions that were labeled by the rabies virus. Prof. Dr. Oberlaender quantitatively analyzed the trans-synaptic spread of the rabies virus and defined orders of spread. Many lab members contributed to the reconstruction of vMN dendrites in varying degrees: Dr. Oberlaender, Dr. Guest, Dr. Bast, Dr. Narayanan, Dr. Udvary, Park, Ivanovs and Kayvanjoo. Dr. Bast suggested the possibility of representing the FN geometry with an ellipsoid.

3D local reference frame of the rat vibrissal motor cortex I generated Pia and WM surface triangulations for the third-order rabies labeled (rabies restricted to the layer 5 of the cortex) cortical hemispheres (LHS and RHS). I clustered the rabies labeled neurons into motor and sensory clusters and removed outliers using density based thresholding. I extracted the rabies labeled regions and quantified their variability in terms of their volume, extent and orientation of their principal directions. The motor region in the LHS was most consistently labeled across animals and represented the vibrissal motor cortex (vM1). Hence, I generated average (standard) model of the vM1 and quantified its precision. I quantified the number of neurons (NeuN labeled) within the vM1 in 2D image sections and a sample 3D image stack using the algorithm developed by Prof. Dr. Oberlaender (Oberlaender, Dercksen, et al., 2009). I obtained scaling factor (2D to 3D) to estimate the number of neurons and derived the layer borders of the vM1 using the neuronal density profile. I analyzed the cellular and laminar organization of the vM1 by quantifying the number and density of neurons within each layer along with their variabilities. I generated barrel columns and compared the barrel centre

depth, barrel column height and orientation with a previous study (R. Egger et al., 2012). I also derived the layer borders of the barrel cortex and compared them with a previous study (Meyer et al., 2010). I developed registration routine to register data into the vM1 reference frame and used it to register 3D neuronal morphologies of the motor cortex neurons (soma, dendrite and axon) into the vM1. I grouped registered neurons into layer specific cell types and visualized them as galleries.

Dr. Guest carried out the rabies related experiments in collaboration with Wendel under the supervision of Prof. Strick. Dr. Guest performed histology, slicing (coronal and tangential) and high resolution imaging of the third-order cortical hemispheres and also marked the rabies positive somata in some animals. Maharjan contoured the Pia, WM and barrels of the third-order cortical hemispheres; marked the rabies labeled neuron somata in the cortex and aligned 2D Pia, WM and barrel contours (along with the rabies labeled somata) using the blood vessel and barrels in the tangentially sliced animals and using the method developed by Park in the coronally sliced animal. He identified and contoured various cortical brain regions as defined by the Paxinos rat brain atlas (Paxinos & Watson, 2006). He also imaged a region around the central axis of the vM1 in high resolution for 3D counting of neuronal somata. Dr. Narayanan performed *in vivo* filling and the subsequent histology, slicing and high resolution imaging of the motor cortex morphologies. He also reconstructed 3D morphologies using the method developed by Prof. Dr. Oberlaender (Oberlaender et al., 2007) and performing manual proof editing using the Filament editor extension in Amira software (Dercksen et al., 2014). Ivanovs, Kayvanjoo and Javadova assisted Dr. Narayanan in the reconstruction process. Dr. Narayanan also aligned the 2D Pia, WM and barrel contours to each other using the blood vessels and barrel contours.

Contributions to the published article As an equal first author of the article, I analyzed anatomical data; generated local reference frame of the rat FN; registered FN data from different experiments into the FN reference frame; analyzed and generated whisker row-specific vMN slabs; registered and analyzed the dendritic organization of vMNs (Guest, Seetharama, Wendel, Strick, & Oberlaender, 2017).

Contents

List of Figures

List of abbreviations

2D	Two-dimensional
3D	Three-dimensional
Amb	Ambiguus nucleus
BOLD	Blood oxygen level dependent
CTB	Cholera toxin beta subunit
CV/CoV	Coefficient of variations
DPGi	Dorsal paragigantocellular nucleus
DSC	Dense structural composition
D-V	Dorsal - ventral axis
fMRI	Functional magnetic resonance imaging
FN	Facial nucleus
Gi	Gigantocellular reticular nucleus
IC	Insular cortex
IOD	Inferior olive, dorsal nucleus
Irt	Intermediate reticular nucleus
L1/2/3/4/5/6	Cortical layer 1/2/3/4/5/6
L2PY/L3PY/L4PY	L2 pyramidal neuron / L3 pyramidal neuron / L4 pyramidal neuron
L4sp/L4ss	L4 star pyramidal neuron / L4 spiny stellate neuron
L5IT/L5PT	L5 slender-tufted intratelencephalic neuron / L5 thick-tufted pyramidal tract neuron

$L6_A$CC/$L6_B$CC/L6CT	L6A corticocortical pyramidal neuron / L6B polymorphic corticocortical pyramidal neuron / L6 corticothalamic neuron
LHS	Left hemisphere
L-M	Lateral - medial axis
LPGi	Lateral paragigantocellular nucleus
M1	Primary motor cortex
M2	Secondary motor cortex
MdD	Medullary reticular nucleus, dorsal part
MdV	Medullary reticular nucleus, ventral part
Mve	Medial vestibular nucleus
PC(s)	Principal component(s)
PCA	Principal component analysis
PCRt	Parvicellular reticular nucleus
PFA	Paraformaldehyde
PMn	Paramedian reticular nucleus
PnC	Pontine reticular nucleus
POST	Postsynaptic structures (e.g., spines of excitatory neurons)
Pr	Prepositus nucleus
Pr5	Principal sensory trigeminal nucleus
PRE	Presynaptic structures (i.e., boutons)
PreBotC	Pre-Botzinger complex
R-C	Rostral - caudal axis
RHS	Right hemisphere
S1 BF	Primary somatosensory cortex, barrel field
S1 FL	Primary somatosensory cortex, forelimb
S1 UL	Primary somatosensory cortex, upper lip
S2	Secondary somatosensory cortex
SBF	Standard barrel field
SD/STD	Standard deviation
SEM	Standard error of the mean

Sol	Solitary tract
Sp5C	Spinal trigeminal nucleus, caudal part
Sp5I	Spinal trigeminal nucleus, Interporalis
Sp5O	Spinal trigeminal nucleus, Oralis
SpVe	Spinal vestibular nucleus
ts	Tectospinal tract
vM1	Vibrissal part of the motor cortex (informally: vibrissal motor cortex)
vMN(s)	Vibrissal motoneuron(s)
VPM	Ventral posterior medial nucleus of the thalamus
vS1	Vibrissal part of the primary somatosensory cortex (informally: barrel cortex)
WM	White matter tract

1 | Introduction

1.1 Reference frames for neuroanatomical modeling

1.1.1 Neuroanatomical modeling of brain regions

How do the brain-wide, interconnected, neuronal networks generate behavior? This is a key question that motivates many neuroscientific studies (Ahrens et al., 2012; Yuste, 2015; Perich & Rajan, 2020; Shenoy & Kao, 2021). Owing to the complexity of the brain, it is typical for researchers to focus on a particular behavior and the interconnected brain regions that produce it. Many studies further restrict the focus on a particular brain region of interest and investigate the structure-function relationship between the anatomy of the brain region and its function (Stanford & Sherman, 1984; Harms, Wang, Csernansky, & Barch, 2013; Khalsa, Mayhew, Chechlacz, Bagary, & Bagshaw, 2014). Brain regions are defined either anatomically by using distinct anatomical landmarks that distinguish them from their surroundings or functionally by their connectivity to other brain regions. As an example, some major brain regions involved in the human visual system are depicted in Figure 1.1 A.

The neuroanatomy of brain regions can be modeled at several spatial scales: geometrical, cellular, sub-cellular and synaptic. Consequently, the resolution required for modeling at various scales range from centimeters (for modeling the brain region geometry) to nanometers (for synaptic level modeling). Modeling the geometry of the brain region of interest typically involves the following steps. First, the contours of the brain region are delineated using either the salient anatomical

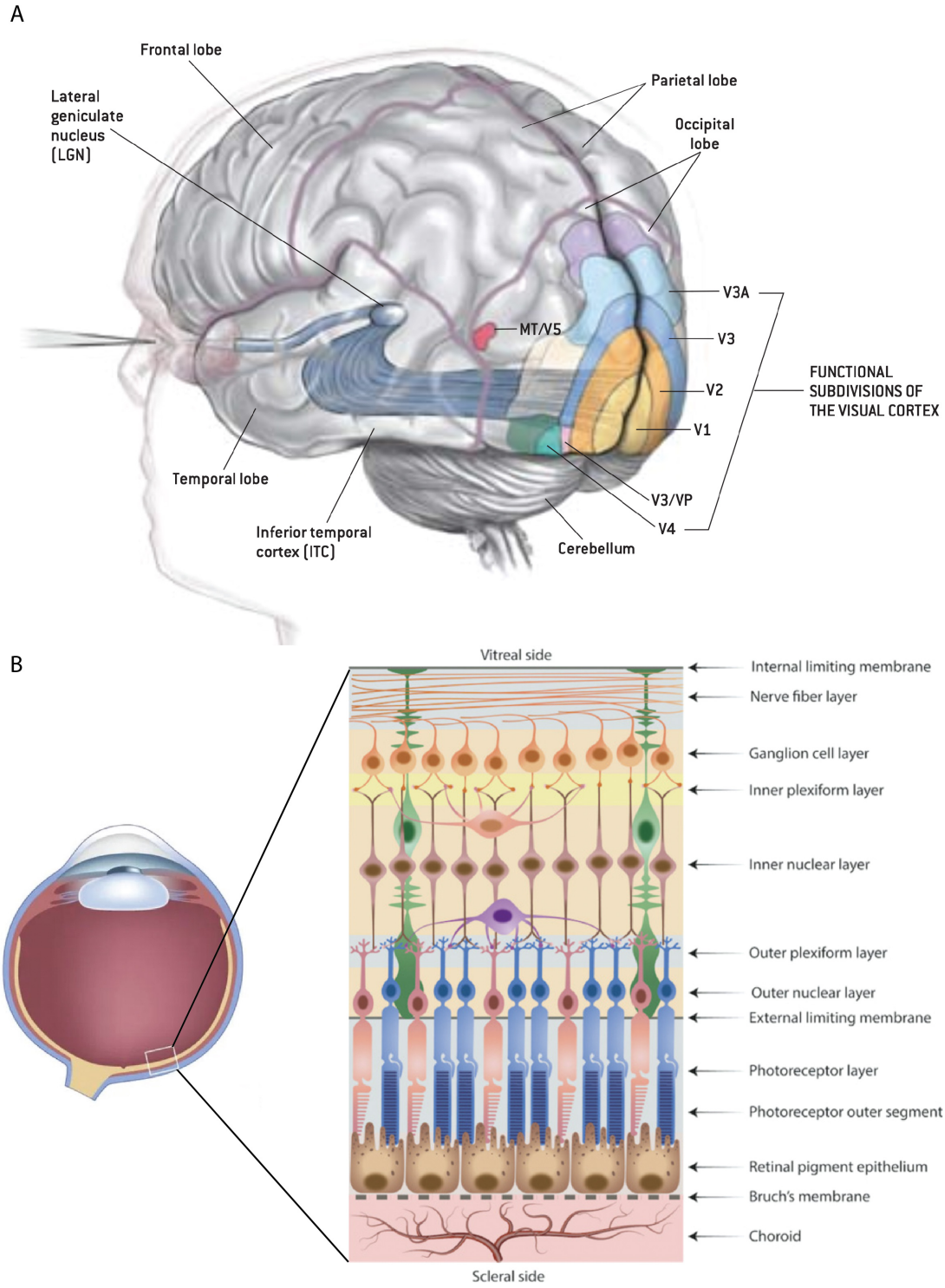

Figure 1.1. Neuroanatomical modeling of brain regions. A. Illustration of some important brain regions involved in the human visual system. It depicts the input pathway (eye, optic nerves, LGN and optic radiations) along with the functional

Figure 1.1. subdivisions of the visual cortex (V1, V2, V3, V3A, V3/VP, V4, MT/V5). Additionally, different lobes of the cerebral cortex have also been labeled. This panel has been adopted from (Logothetis, 1999). B. Schematic illustration of the neuroanatomical model of the retina. Left: Top view of the eye. Right: Profile of a small portion of retina (from left panel) depicting the major cell types along with their layer-wise organization and connectivity. This panel has been adopted from (Ferrara et al., 2021)

features (landmarks) or their synaptic distance from other brain regions, and the 3D geometry of the brain region is extracted. Optionally, the 3D geometry of the brain region can be simplified into a pre-defined geometrical shape with appropriate parameterization. Second, inter-animal variability of the brain region across animals is quantified along with the quantification of the geometrical precision of these models by aligning them to one another. If the variability is low, in other words, if the brain region is consistent across animals, then an average model of the brain region can be generated. The cellular organization of the brain region can be modeled by quantifying the number (density) and distribution of excitatory and inhibitory neurons. Furthermore, the region specific features such as laminar or somatotopic organization can be delineated along with the determination of the variability of such features. Modeling the sub-cellular or morphological organization entails digital reconstruction of neuronal morphologies and classifying them into canonical cell-types using axonal and dendritic features. Modeling at the synaptic level requires delineating the local synaptic connectivity between various cell-types of the region along with their number, strength and distribution. Furthermore, the pre-synaptic neuronal populations that provide synaptic inputs to and the post-synaptic neuronal populations that receive outputs from the neurons of the brain region can be identified using retrograde or anterograde tracer injections. Figure 1.1 B illustrates the internal organization of the retina as an example, wherein the major cell types, their layer-wise organization and their connectivity have been depicted schematically.

1.1.2 Reference frames

Role of reference frames In most neuroscientific enquiries, irrespective of whether the focus of the study is entire brain or specific brain regions, it is imperative to combine experimental data (functional or anatomical) from multiple specimens to arrive at consistent results. The need for sampling multiple specimens exists due to the inherent variability involved in these studies - arising from experimental conditions and/or from the biology itself. Reference frames provide a common coordinate system to incorporate data obtained across multiple experimental conditions and specimens in such studies. Reference frames can be global or local. Global reference frames define a brain-wide common coordinate system, whereas local reference frames define brain region specific coordinate systems.

Reference frames perform two main functions. First, they allow targeting the brain region of interest across multiple specimens by providing coordinates of its location. Figure 1.2A illustrates this with a global reference frame of the mouse brain, where the location of the desired brain region is given by the stereotaxic coordinate system. Stereotaxic coordinates are defined with respect to the Bregma (the intersection point of coronal and sagittal sutures) and Lambda (the intersection point of lambdoid and sagittal sutures). Second, they provide a way of registering data sampled from multiple specimens into the common reference frame, providing an effective way of combining data obtained across animals and experimental conditions. This is exemplified in Figure 1.2B, which illustrates the combining of blood oxygen level dependent (BOLD) signals obtained from different subjects during a fMRI experiment. The data from each subject is then registered to an average model of the brain (common reference frame) in order to determine the brain regions that were on average active during a specific task.

Global reference frames Brain atlases demarcate different brain regions through out the brain, by identifying the cell clusters using histochemical staining (such as Nissl staining) and combining it with the prior knowledge about the location of brain regions (Swanson, 2004; Paxinos & Watson, 2006). Figure 1.3B shows Nissl staining (left half) and annotation of various regions (right half) in a coronal section though a mouse brain as per (Hawrylycz et al., 2014). A 3D brain atlas of

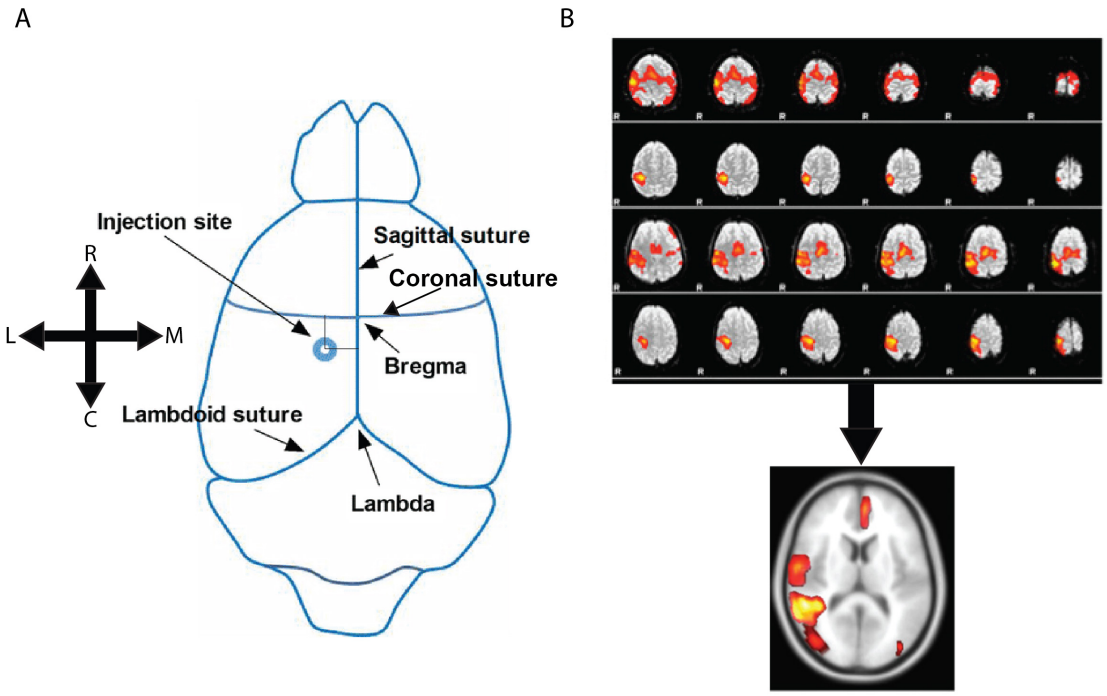

Figure 1.2. Functions of reference frames. A. Schematic of the stereotaxic coordinate system. This top view of the mouse brain illustrates the sagittal, coronal and lambdoid sutures on the skull. The intersection of the sagittal and coronal sutures - Bregma, as well as the intersection of sagittal and lambdoid suture - Lambda are depicted in the figure. The injection site shown in the figure can be specified in this stereotaxic coordinate system by its distance from Bregma (or Lambda) along the lateral-medial and caudal-rostral axes. This figure panel has been adopted from (Yin et al., 2020). B. Illustration of a typical fMRI experiment. The rows represent each subject and the columns represent different z-slices. The BOLD signals from each subject during the task are registered to the average brain (shown in axial view at the bottom) in order to determine the brain regions that are on average active during the given task. Image credit: Mr. Chris Rorden [1].

the entire mouse brain illustrating various annotated brain regions is shown in Figure 1.3A, which has been developed from annotated brain sections like the one shown in 1.3B (Hawrylycz et al., 2014). Such whole brain atlases function as global reference frames by achieving the following. First, they enable targeting the desired brain region by providing their stereotaxic coordinates. Second, they provide a way to combine data sampled across multiple brains into the global reference

[1] https://mriquestions.com/registrationnormalization.html

frame by aligning the individual brains to the reference brain atlas using rigid, similarity or affine transformations. In a rigid transformation only translation and rotations are allowed. Similarity transformation allows isotropic scaling (uniform scaling in all three dimensions) in addition to the rigid transformations. Affine transformation allows anisotropic scaling (independent scaling in each dimension) in addition to the rigid transformations. Global reference frames aid neuroanatomical modeling when the entire brain or several regions within the brain are being studied. Furthermore, atlases provide a way to model long range connectivity between brain regions.

Global reference frames play a crucial role in the modeling of brain-wide neuroanatomy. However, when we aim to generate a detailed model of a specific brain region, several challenges arise. The brain region of interest could be typically an order of magnitude smaller compared to the whole brain. For example, the brain of a male Wistar rat (weighing 290 g) is about 21.3 mm long in the R-C axis. Whereas, the VPM region of the brain is about 2.2 mm long in the same axis (Paxinos & Watson, 2006). This order of magnitude difference in scale between the whole brain and the region under study adversely impacts the modeling of the brain region in several ways. First, attempting to target the desired brain region for experimental intervention (such as labeling of cell population using tracer injections) using the globally defined stereotaxic coordinates could lead to wrongly targeting the adjacent brain regions instead. Second, during the registration of individual brain regions into the global reference frame, the anatomical landmarks of the brain region of interest (such as labeled cell populations or neuronal morphologies) could incorrectly get registered to the adjacent brain regions in the atlas, since the whole brain tissue is used as landmark during the registration instead of the brain region under study. In both the above cases the characterization of the brain region under study would end up being incorrect, unless we independently verify that the brain region of interest has been accurately targeted, using other means. Third, the true biological variability of the brain region of interest (the consistency of the region across specimens) cannot be accurately measured

[2]Allen Institute for Brain Science: https://connectivity.brain-map.org/3d-viewer?v=1

[3]Allen Institute for Brain Science: https://atlas.brain-map.org/atlas?atlas=1&plate=100960244#atlas=1&plate=100960244&resolution=16.75&x=5508&y=3904&zoom=-4

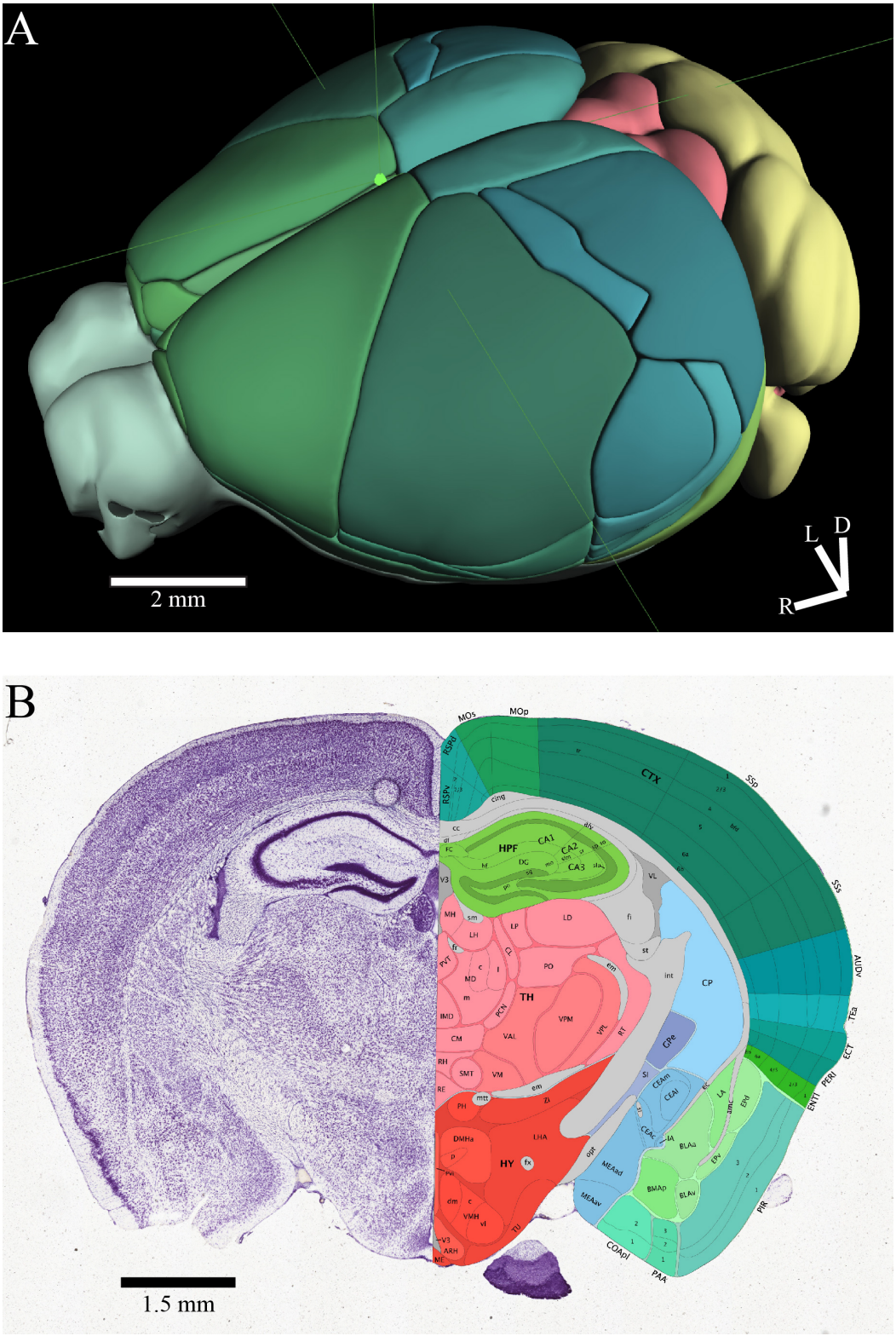

Figure 1.3. Brain atlases are global reference frames. A. Image credit [2].

Figure 1.3. A 3D atlas of the mouse brain illustrating various annotated brain regions. The orientation is indicated by the axes on the bottom right corner. B. A coronal section though a mouse brain, wherein the left half is showing the Nissl staining and the right half is annotating various brain regions within this section. Image credit [3].

using the global reference frame, since it is difficult to distinguish between the variability introduced due to the experimental artifacts (such as distortion during the slicing and histology of the whole brain tissue) and the biological variability of the brain region under study. Fourth, studying the cellular and morphological organization of the brain region of interest requires resolutions in the range of a few micro meters, which is several orders of magnitude smaller compared to the scale of the whole brain. Therefore, global reference frames are inadequate when a precise model of geometrical, cellular and morphological organization of a specific brain region is required.

Local reference frames Aforementioned shortcomings of the global reference frames are addressed by the local reference frames, wherein a region-specific coordinate system is defined for the brain region under study as opposed to defining a brain-wide coordinate system. The advantages of this approach are as follows. First, the brain region under study is identified and defined in each animal individually. Thus making it possible to verify whether the anatomical or functional data sampled across animals indeed belong to the target region in each animal (either during the experiments or during the post-hoc analysis). Therefore, the resulting analysis will accurately characterize the region under study. Second, since the brain region is locally identified in each animal, the impact of experimental artifacts of whole brain tissue processing (slicing angle, histology, etc.) will be minimal on the accuracy of region being modeled as opposed to global reference frames. Therefore, the true biological variability of the brain region across animals can be quantified using local reference frames. Third, since the brain region of interest is extracted from each individual animal, by aligning these regions locally with one another, we can quantify the precision of the brain region. Thus, local reference frames provide a higher precision compared to global reference frames,

where the whole brain is used for aligning the regions. Therefore, when precise modeling of the geometrical, cellular and morphological organization of the brain region under study is required, local reference frames are needed.

Neuroanatomical modeling of desired brain regions using the local reference frame approach, typically involves the following steps. First, the brain region of interest is identified using a pre-defined criteria. Salient anatomical landmarks that help distinguish the region from its surroundings can generally be used as this criteria. Second, the region is digitally reconstructed, and if viable, the 3D digital model of the region is represented by a suitable geometrical shape. Third, the 3D digital models of the region sampled across different animals are compared with one another and the biological variability of the region is determined. If the variability is low (the region is well conserved across animals), an average (standard) 3D model of the region is generated with known precision, which defines the local reference frame of the region. Fourth, anatomical or functional data belonging to the region (such as soma distributions, neuronal morphologies, etc.) sampled across animals are registered to the reference frame by aligning the individual models to it using rigid or affine transformations. The higher precision of registered data enables modeling and analysis of the organization (such as cellular or morphological organization) of the brain region of interest.

1.2 Overview of the rat barrel cortex reference frame

In the previous section, I introduced the concept of using local reference frames for precise neuroanatomical modeling of desired brain regions. In this section, I will elucidate this approach with the example of a local preference frame. In a series of studies conducted by Dr. Marcel Oberlaender's lab, 3D local reference frame has been developed for the rat barrel cortex and has been applied to delineate its cellular and morphological composition. Furthermore, a model of the dense structural composition of the rat barrel cortex as well as its statistical connectome have also been derived. Here, I provide a brief overview of these studies.

1.2.1 3D local reference frame of the rat barrel cortex

Nocturnal rodents, such as rats and mice, use the whiskers on their snout as sensory organs to explore their environment. These whiskers are organized in a grid like fashion into rows (numbered A-E and the greek row) as well as arcs (numbered 1-7 and greeks - α, β, γ, δ) (see figure 1.4A). Sensory information from whiskers flow into sensory cortex called the primary vibrissal somatosensory cortex (vS1) via brain stem and thalamus (VPM). Layer 4 of the vS1 (granular layer) consists of dense neuron clusters called "barrels" which are somatotopically organized following the arrangement of whiskers on the snout (see figure 1.4B), wherein neurons within each barrel respond most strongly to the deflection of the assigned whisker. Extrapolation of such barrels to Pia and WM, encompassing all six layers, forms barrel columns ((Welker, 1976; Woolsey, 2016)), which are equivalent to cortical columns, thought to be the discrete functional units of sensory cortices (Hubel & Wiesel, 1959; Mountcastle, 1957). Due to the whisker somatotopy, the laminar organization and the ease of experimental access, the rodent barrel cortex is a popular brain region for neuroanatomical studies (see reviews (Feldmeyer et al., 2013; Petersen, 2007)) and thus was a natural starting point for the generation of precise 3D local reference frame.

Such a precise 3D local reference frame of the rat barrel cortex has been developed and reported in (R. Egger et al., 2012). In order to accurately extract the barrel contours, tangentially sliced brain sections were stained using Cytochrome-oxidase and imaged at high resolution. Automated image processing algorithms identified the contours of barrels by enhancing the contrast between barrels and septa (low density space between barrels). 2D image sections were then aligned using the blood vessels as landmarks and the resulting 3D barrel contours were smoothed in the Z direction (see figure 1.4C). The geometry of 3D barrel reconstructions were then represented by cylinders; the axis of the cylinder were extended to Pia and WM to form the barrel column (see figure 1.4D). Across 12 rats, the 24 barrels varied in their parameters such as mean *barrel area* and mean *barrel column height* ranging between 64 800 µm^2 - 158 900 µm^2 and 1600 µm - 2117 µm respectively (see figure 1.4E). However, the variability of each barrel across animals were very small. For example, the variability of the C2 column (as given by

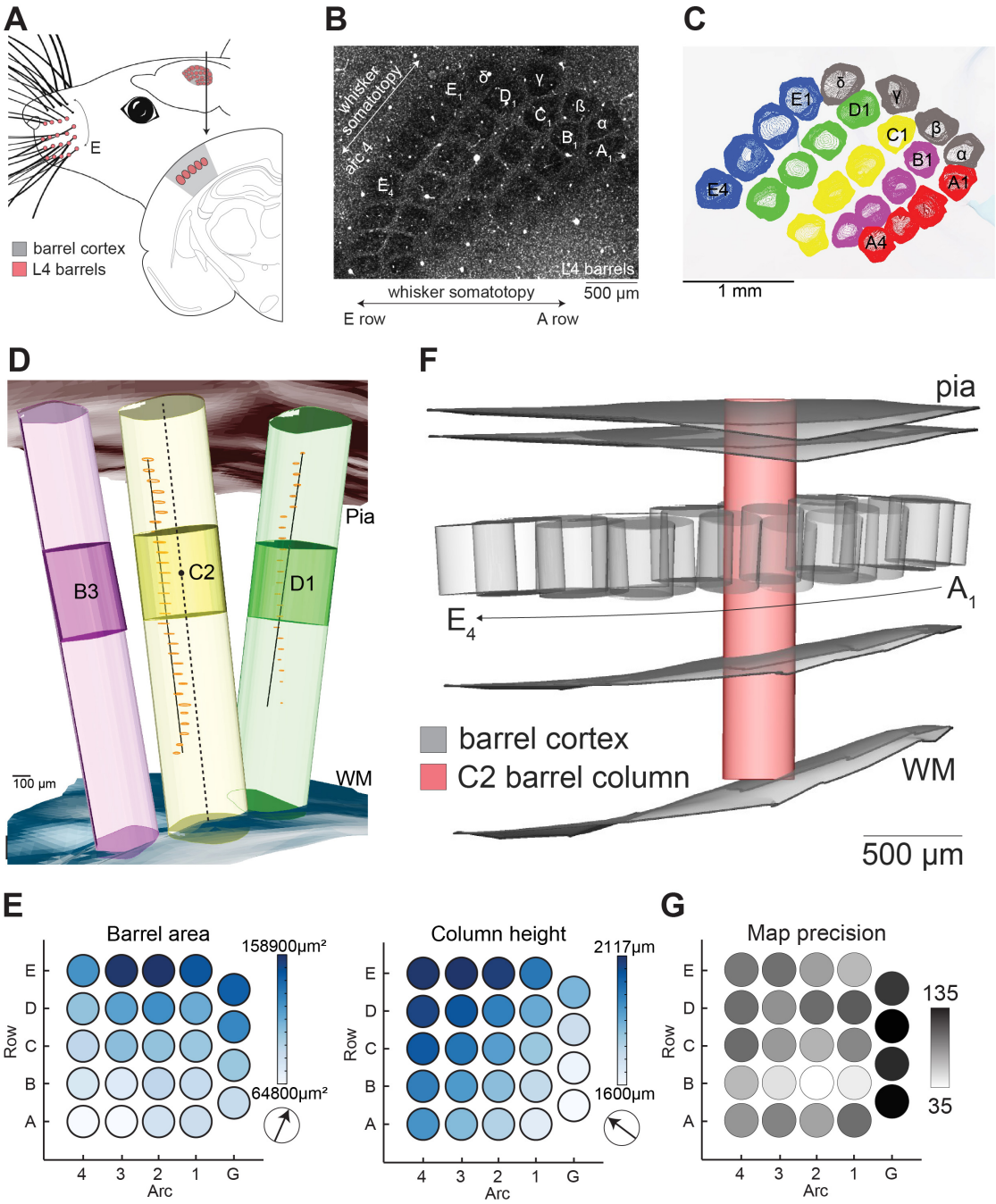

Figure 1.4. Geometric organization of the SBF. A. Schematic of the rat vibrissal somatosensory cortex (vS1) shows that the organization of the barrels follow the arrangement of whiskers on the animal's snout. Inset: coronal section showing neuron dense clusters (barrels) in layer 4 of the barrel cortex. B. High resolution image of a tangential section through layer 4 of the barrel cortex, depicting the organization of barrels into rows and arcs. C. Tangential view of automatically segmented barrel contours (limited to arc number 4). D. Side (semi-coronal) view

Figure 1.4. of 3 (B3, C2, D1) barrel columns. The barrels have been replaced by the equivalent cylinder and its axis extrapolated to Pia and WM to form barrel columns. Blood vessels used for the alignment of 2D sections is also shown. E. The variability of barrels within the barrel cortex, illustrated by mean barrel area (left) and mean barrel column height (right) (N=12). The gradient along which the values increase is also shown along with the color bar. F. Side (semi-coronal) view of the average model of the barrel cortex geometry (SBF) with all standard barrels and C2 barrel column displayed. In this local reference frame of the barrel cortex, the center of the C2 barrel is the origin and the axis of the C2 barrel column is the vertical (Z) axis. G. Precision of the geometric map of the barrel cortex ranges between 35 µm and 135 µm. These precisions were obtained by registering individual barrel cortices to the average model. Figure panel A, B, F and G were adopted from (Udvary, 2021), whereas panels C, D and E were adopted from (R. Egger et al., 2012)

the SD and CV) with respect to the five parameters - *barrel area*, *barrel top*, *barrel bottom*, *barrel column orientation* and *barrel column height* - were 13 700 µm^2 (13%), 43 µm (9%), 37 µm (4%), 4.9° (average of C1 and C3) and 100 µm (5%) respectively. Since the barrel cortex is well preserved across animals, an average model was generated with center of C2 barrel as the origin of this reference frame (see figure 1.4F), henceforth referred as the standard barrel field (SBF). The precision of registering barrel cortices to the SBF using rigid transformations ranged from 35 µm to 135 µm (see figure 1.4G) having an average euclidean precision of 90 µm and orientational precision of 4.5°.

1.2.2 Applications of the SBF

The local reference frame thus developed was then applied to delineate the cellular and morphological organization of the SBF. Furthermore, a dense structural model of the anatomy was developed, yielding a statistical connectome of the SBF.

Cellular organization of the SBF The cellular organization of the SBF has been delineated in a series of studies (Meyer et al., 2010, 2011, 2013). In (Meyer et al., 2013), four Wistar rats aged P28-29 were sliced into 50 µm thin sections tangential to the barrel cortex and double-immunolabeled for NeuN (Mullen, Buck, &

Smith, 1992) and GAD67 (Julien, Samama, & Mallet, 1990; Kaufman, McGinnis, Krieger, & Tobin, 1986; Kobayashi, Kaufman, & Tobin, 1987); before undergoing high resolution (0.36075 × 0.36075 × 0.5 µm/voxel) imaging using a laser confocal microscope (see figure 1.5A,B). NeuN and GAD67 positive somata were detected automatically using the algorithm reported in (Oberlaender, Dercksen, et al., 2009; Meyer et al., 2013) (see panel insets of figure 1.5A,B). The number of neurons thus counted within 24 barrel columns (α-δ, A1–E4) and septa between them was 529,715 ± 39,104 (mean ± SD, N=4) and volumes were 6.60 ± 0.58 mm^3; thus the neuronal densities varied by less than 5% (80,419 ± 3,688 mm^{-3}). The soma distribution showed whisker barrel specific clusters (see Figure 1.5C,D). The number of neurons per barrel column showed whisker row specific organization, ranged between 9700 to 29600, increasing gradually as we travel from whisker row A to E. Since the barrel column volumes also show the same whisker row specific organization (ranging between 0.12 mm^3 to 0.36 mm^3), the resulting neuron density per barrel column was more uniform, ranging between 72800 and 84700 per mm^3 (see Figure 1.5G). The soma distributions also display laminar organization, having all 6 cortical layers (see Figure 1.5E). The layer borders were defined using the neuronal density profile of barrel columns (Meyer et al., 2010) (see Figure 1.5F). Although, the neuron counts varied within each barrel cortex, the variability across animals was limited, ranging between 4% to 23%. Similarly, the laminar precision varied within a narrow range of 19 µm to 63 µm (see 1.5H,I).

Morphological organization of the SBF The morphological organization of the SBF has been delineated in (V. Egger, Nevian, & Bruno, 2008; Bruno, Hahn, Wallace, de Kock, & Sakmann, 2009; Oberlaender et al., 2011, 2012; Narayanan et al., 2015). In (Narayanan et al., 2015), *in vivo* cell-attached recording and juxtasomal Biocytin filling (Pinault, 1996; Narayanan et al., 2014) was performed for 153 neurons. Following the histology, sectioning and high resolution imaging, the 3D morphologies were reconstructed either manually or automatically using custom developed algorithm (Oberlaender et al., 2007) (see Figure 1.6A). Resulting 3D morphologies were registered to the SBF by first aligning their anatomical landmarks (Pia, WM and barrels) to the SBF and then fine tuning by correcting for different slicing orientation and tissue shrinkage (R. Egger et al., 2012) (see Figure

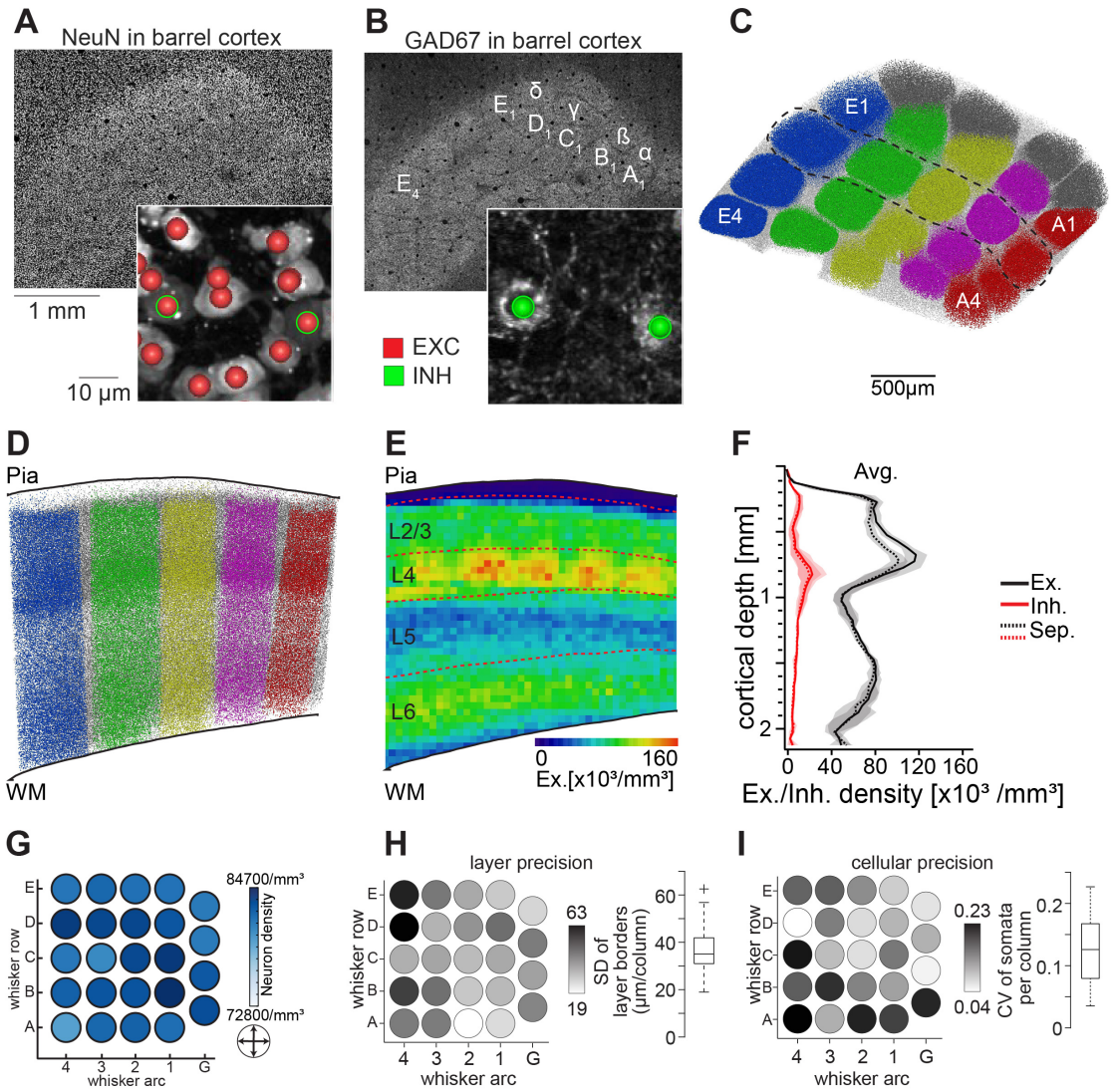

Figure 1.5. Cellular organization of the SBF. A. A high resolution optical section sliced tangential to the layer 4 of the barrel cortex that has been immunolabeled with NeuN for soma counting. Inset: Zoom-in to a part of the image, showing the automatically detected soma locations with red landmarks. B. Same as in panel A, but with GAD67 staining for labeling inhibitory neurons. Inset: Zoom-in to a part of the image showing detected inhibitory soma location with green landmarks. C. Tangential view of soma locations of all neurons in the barrel cortex of an animal. High neuronal density barrel column clusters with the low density septa between them are visible; whisker rows are color-coded. D. Semi-coronal (side) view of the soma locations of the barrel columns encircled by the dotted line in panel C. E. 2D projection of average density of excitatory neurons of the barrel cortex. Barrels are visible as high density regions. Density variation along the vertical (barrel column) axis delineates layer borders. F. Average neuronal density profiles of

Figure 1.5. excitatory and inhibitory neurons within the barrel columns as well as the septa; averaged across 24 barrels of 4 rats. G. Neuronal density of barrel columns of 24 whiskers were relatively uniform, showing no whisker specific organization; and varied in a narrow range between 72800 and 84700 neurons per mm^3. H. Precision of the laminar organization of 24 barrels ranged between 19 µm and 63 µm (averaging 50 µm). I. The variability of number of neurons per barrel column across 4 rats were between 4% and 23% (averaging 7% for the entire barrel cortex). Panel A,B,H and I are adopted from (Udvary, 2021). Panel C,D,E,F and G are adopted from (Meyer et al., 2013)

1.6B). Those registered morphologies were then assigned to 10 morphological cell-types using 22 morphological, topological, and reference-frame-dependent features with OPTICS algorithm (Ankerst, Breunig, Kriegel, & Sander, 1999; Oberlaender et al., 2012) (see Figure 1.6C). Representative morphological samples (with dendrites and axons) for each cell-type is visualized within the SBF in Figure 1.6D.

Dense structural composition of the SBF Since the geometric map and the laminar organization of the SBF varied by less than 100 µm (±50 µm), a cubic sub-volume of 50 $µm^3$ was used as the resolution limit for further analysis of the SBF. A dense structural model of the SBF was generated by combining the geometric, cellular and morphological data of the SBF ((R. Egger et al., 2014; Udvary, 2021; Udvary et al., 2022)). This was achieved as follows. First, each 50 µm cube of the SBF was populated by the average number of neuron somata assigned to its nearest barrel column and cortical layer. The cell type of the somata were assigned based on the relative frequency of cell types within the region. Second, each soma was replaced by registering an *in vivo* labeled neuronal morphology in its place (see Figure 1.7A). The soma depths (±50 µm), orientations and relative path length distributions were preserved during this process. For each cube, the axonal and dendritic path lengths that each neuron in the model contributed was quantified (see Figure 1.7B). The soma and neurite packing density as well their diversity (cell types) varied based on the location of the cube within the model (see Figure 1.7C). Third, the neurite densities of axons and dendrites in each cube were replaced by bouton and spine densities respectively and the *dense structural*

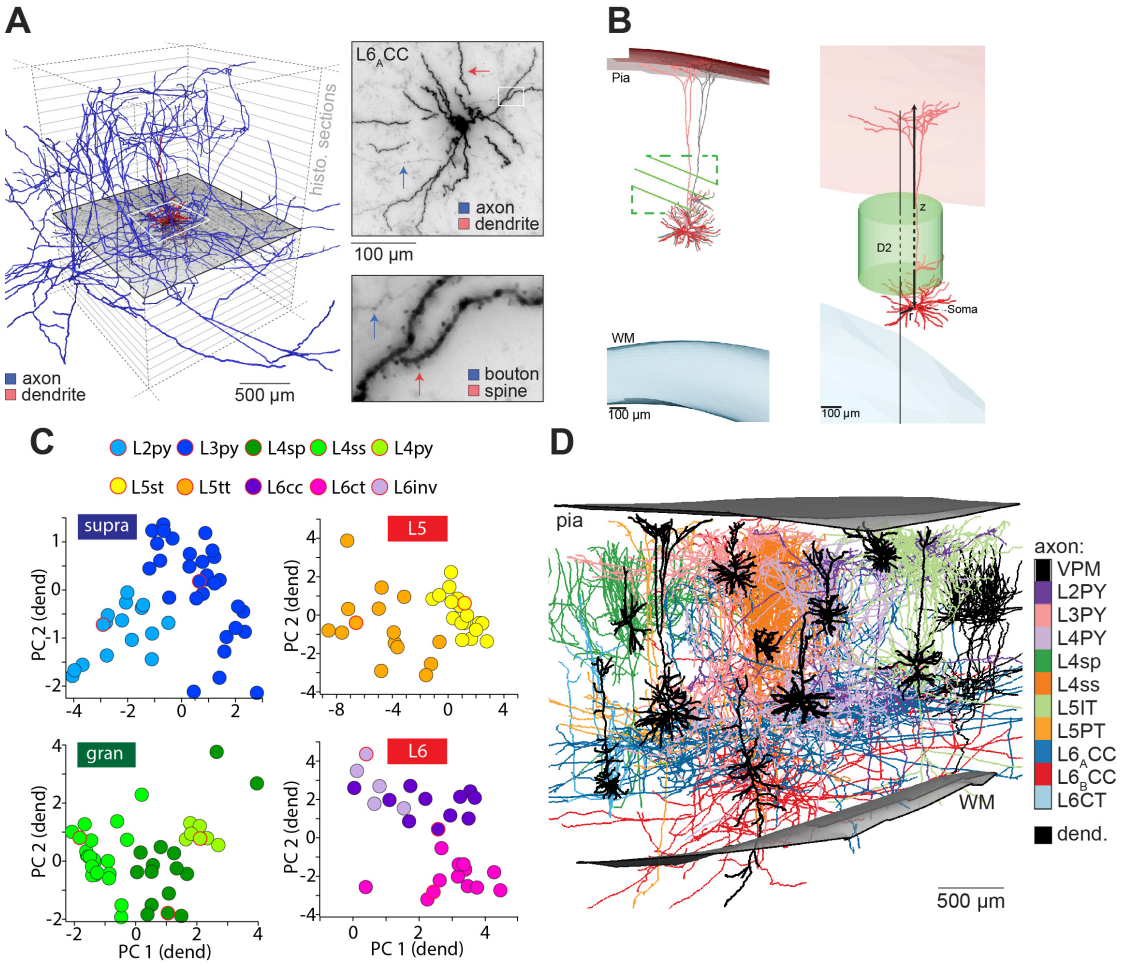

Figure 1.6. Morphological organization of the SBF. A. Left: 3D digital reconstruction of an *in vivo* labeled neuronal morphology. Dendrites are shown in red and axon in blue. The histological sections from Pia to WM are indicated in dotted lines. Top-right: High-resolution image of a section containing soma, dendrites and axon. Bottom-right: Zoom-in of a crop from the image above, showing spines and boutons. B. Illustration of registering neuronal morphologies to the SBF. Left: Side (semi-coronal) view of a L5tt dendrite that has been registered to the SBF by aligning its barrel field to the SBF (grey). The orientation of the apical dendrite is not perpendicular to the original slicing angle (green lines). The registered neuron is further rotated to match the direction of apical dendrite to the registered barrel column's axis (red). Right: Registered landmarks are scaled using supra-granular, granular and infra-granular scaling factors in order to match the respective landmarks of the SBF, resulting in the final SBF registered neuron. C. Raster plots of soma-dendritic features along the first two PCs that discriminate between supra-granular (top left), granular (bottom left), layer 5 (top right) and layer 6 (bottom right) cell types. D. 10 major cell-types of the SBF: L2PY, L3PY, L4PY, L4sp, L4ss, L5IT (L5st), L5PT (L5tt), $L6_ACC$ (L6cc), $L6_BCC$ (L6inv), L6CT.

Figure 1.6. Additionally, the VPM axons are also shown. Figure panels A and D are adopted from (Udvary, 2021); panel B from (R. Egger et al., 2012); panel C from (Narayanan et al., 2015).

composition (DSC) of each 50 µm cube $\hat{x}$ between neuron a and b was computed as:

$$\mathrm{DSC}(a, b, \hat{x}) = \mathrm{PRE}(a, \hat{x}) \cdot \frac{\mathrm{POST}(b, \hat{x})}{\sum_{i \in N} \mathrm{POST}(i, \hat{x})} \tag{1.1}$$

Here, PRE(a,$\hat{x}$) and POST(b,$\hat{x}$) are number of pre-synaptic (boutons of a) and post-synaptic (spines of b) structures present within cube $\hat{x}$ respectively; the total number of post-synaptic structures within cube $\hat{x}$ is $\sum_{i \in N} \mathrm{POST}(i, \hat{x})$.

Statistical connectome of the SBF From the *dense structural composition* of the SBF described above, its cell type specific connection probabilities were derived by making two assumptions about the synapse formation. First, any pre-synaptic structure (bouton) can form connection with any post-synaptic structure (spine) available within the cube. Hence, the probability that neuron a makes n connections with neuron b within the cube $\hat{x}$ is given by:

$$p(a, b, \hat{x}, n) = \frac{(\mathrm{DSC}(a, b, \hat{x}))^n}{n!} \cdot \exp(\mathrm{DSC}(a, b, \hat{x})) \tag{1.2}$$

Second, formation of a connection in any cube does not affect the formation of connection in any other cube. Thus, the probability of neuron a making at least one synapse with neuron b is given by:

$$P(a, b) = 1 - \exp(-\sum_{\hat{x}} \mathrm{DSC}(a, b, \hat{x})) = 1 - \prod_{\hat{x}} \exp(-\mathrm{DSC}(a, b, \hat{x})) \tag{1.3}$$

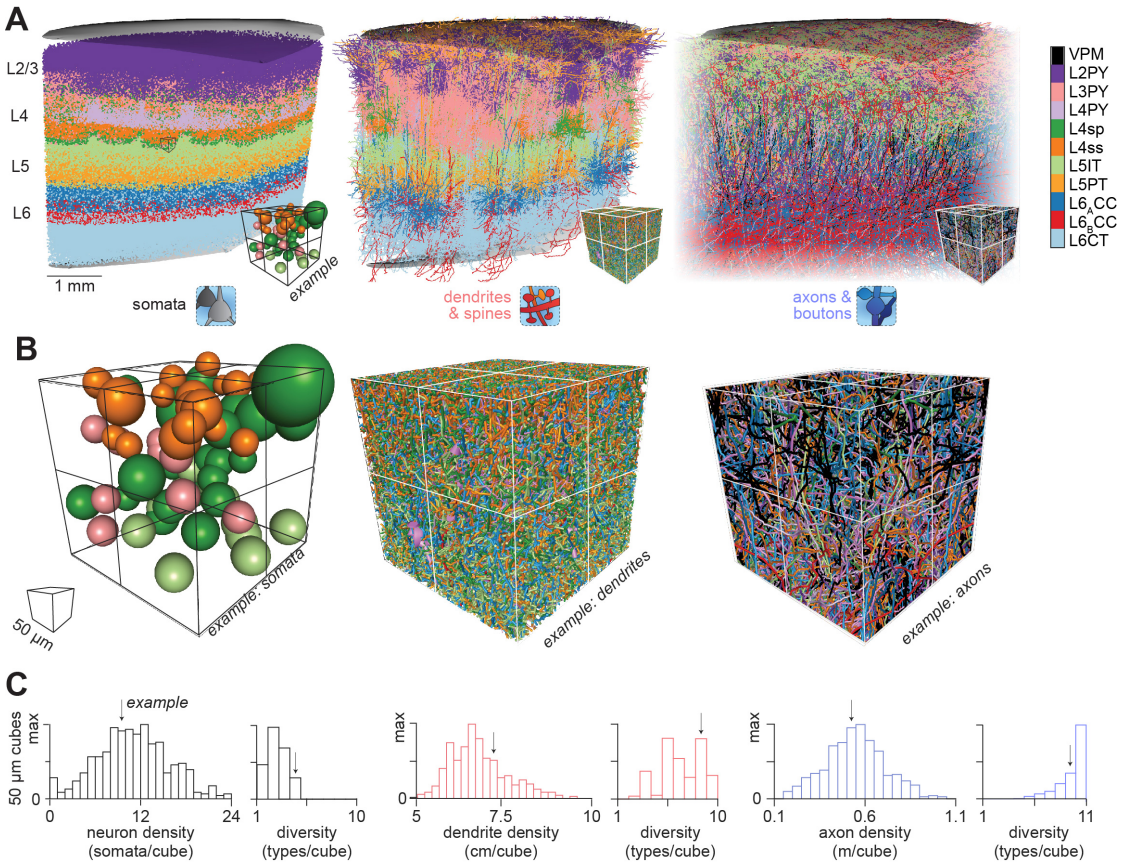

Figure 1.7. Dense structural composition of the SBF. A. Left: Dense model of somata of the SBF, where each 50 µm cube is populated with its average number of somata, assigned to nearest barrel column, and layer. Cell types are assigned based on the relative frequency of cell types in the region. Middle: Each soma is replaced by a dendritic morphology of same cell type. Right: Soma locations replaced by the axonal morphologies of the same cell type. In addition to the 10 cell types, VPM axons are also included in the model. B. Zoom-ins of exemplary 8 50 µm cubes from panel A that show soma, dendrite and axon packing density distributions (from left to right respectively). The color coding represents the cell types. C. Histograms of packing densities of somata, dendrites and axons as well as cell type diversities within each 50 µm cube. This figure is adopted from (Udvary, 2021)

Applying equations 1.2 and 1.3 to the *dense structural composition* of the SBF, yielded its statistical connectome, which provides the probability that any two neurons within the SBF are connected to one another. These connection probabilities can be grouped by the identity of the neurons, such as the barrel columns they

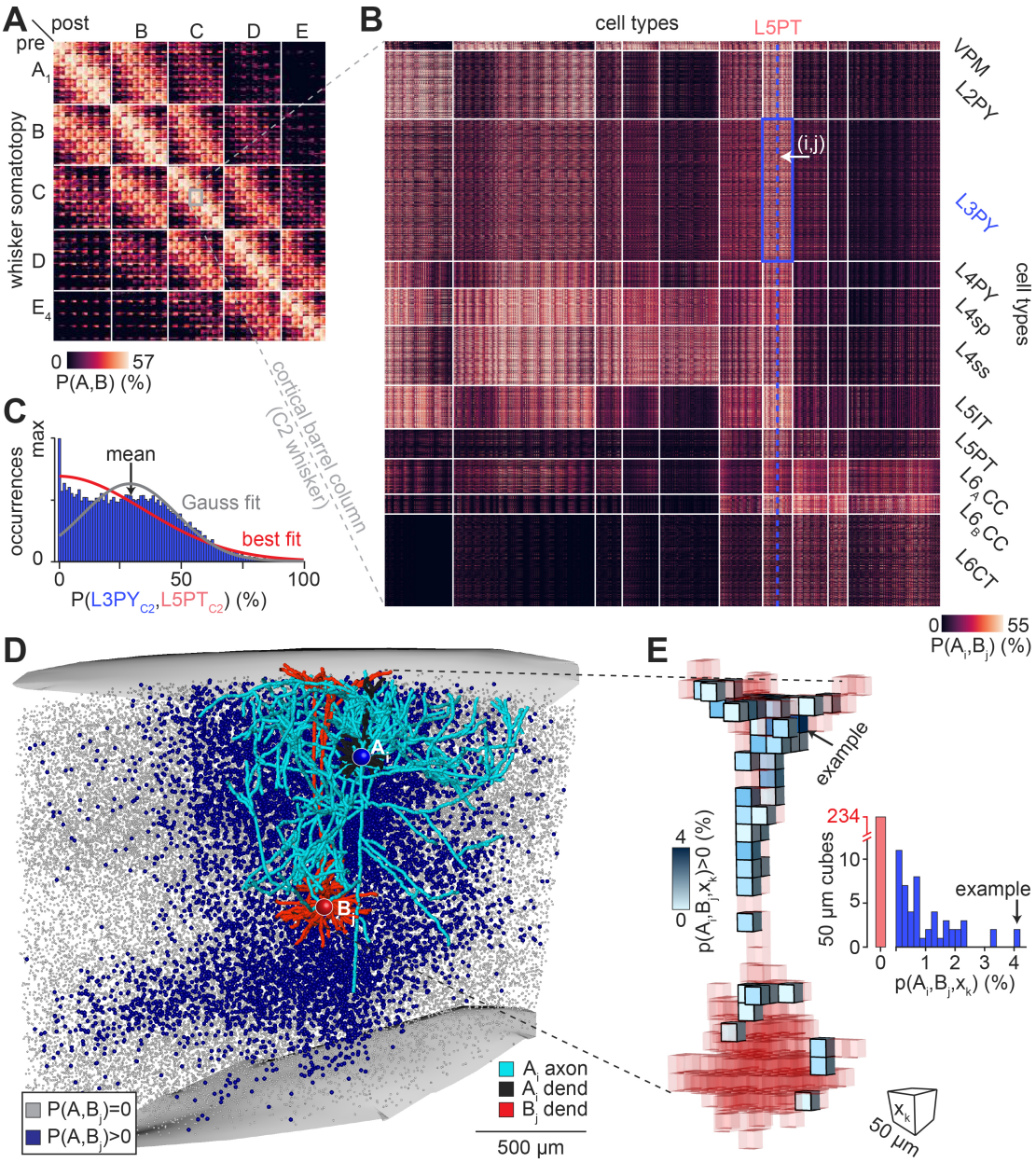

Figure 1.8. Statistical connectome of the SBF. A. Connection probabilities between all excitatory neurons of the SBF, organized into a connectivity matrix, grouped by the barrel columns and cell types. B. Connectivity matrix of C2 barrel column, organized based on cell types, magnified from panel A. C. Connection probability distribution between L3PY and L5PT neurons (highlighted in panel B as blue rectangle). D. All somata that can in principle be connected (shown as blue dots) to an exemplary L5PT neuron (red dendrite; shown as blue dotted line in panel B). An exemplary L3PY neuron that could provide inputs to this L5PT neuron is also shown (dendrite - black; axon - blue). Only 50% of pre-synaptic somata (blue dots) and 10% of all neuron somata (grey dots) are visualized here.

Figure 1.8. E. Pair-wise connection probabilities between example L3PY and L5PT neurons shown in panel D, visualized at the resolution of 50 µm cubes (left). Connection probabilities varied from 0 to 4%, with majority of cubes (234) receiving no input connection from the pre-synaptic neuron. This figure is adopted from (Udvary, 2021).

belong to (see 1.8A) or their morphological cell type (see 1.8B). Furthermore, the connection probability distributions between any two subgroups can be determined (see 1.8C). Additionally, the statistical connectome model can estimate which two neurons could in principle be connected to one another (see 1.8D) and where along the dendrite (in which cube) can these connections occur (see 1.8E).

1.3 Outline of the thesis

In the previous section, the dense statistical connectome model of the SBF has been introduced, which predicts the connection probabilities between pairs of neurons. I developed a method to detect putative synaptic contacts between *in vivo* labeled pairs of neurons, so that we can validate the model by comparing its connectivity predictions with the empirical synapses. The method and the results are presented in sections 2.1 and 3.1 respectively. Having thus verified the utility of local reference framing approach, I developed 3D local reference frames for two more regions of the rat brain: facial nucleus (FN) and vibrissal motor cortex (vM1). The method for developing the FN reference frame as well as the results obtained are presented in sections 2.2 and 3.2 respectively. I applied the FN reference frame to verify the trans-synaptic spread of the rabies virus following its administration into the intrinsic whisker muscle of rats and the results are presented in 3.2.3. Using the rabies-positive cortical neurons that are three synapses away from the terminal muscle, I defined and generated the reference frame of the vM1. The methods and results are presented in sections 2.3 and 3.3 respectively. A comparison of the precisions of local and global reference frame approaches are presented in section 3.4. Finally, I discuss the implications, limitations and the future outlook of the methods and results mentioned above.

2 | Methods

I developed software for image processing, data analysis and registration in C++, python and MATLAB languages. I used ITK[1] and VTK[2] libraries for image processing and visualization. Code that has been developed and used in this thesis can be found on Github[3].

2.1 Detection of putative synapses between *in vivo* labeled pairs of neurons

In this section, I describe a method for detecting putative synapses between *in vivo* labeled pairs of neurons in an unbiased and cell type-specific manner. The *in vivo* labeling and the subsequent reconstruction of multiple neuronal morphologies from a single animal has been carried out by my colleague Dr. David Slabik. I have developed the computational method for detecting putative synapses between these pairs of neuronal morphologies. Earlier attempts for detecting putative synapses and boutons have been reported previously (Smyth, 2015; Mysore Seetharama, 2015).

2.1.1 *In vivo* labeling and morphological reconstruction

The method for *in vivo* labeling and morphological reconstruction of one neuron per animal has been previously established in multiple studies (Pinault, 1996; De Kock, Bruno, Spors, & Sakmann, 2007; Narayanan et al., 2014, 2015). Dr. David

[1] https://itk.org/
[2] https://vtk.org/
[3] https://github.com/mythreyams/PhD

Slabik has modified this method to perform *in vivo* labeling and reconstruction of multiple neurons from a single animal in order to find putative synapses between those neurons. See (Slabik, 2018) for a detailed description of the method.

Here, I reproduce the major steps involved in this method as described in (Narayanan et al., 2014; Slabik, 2018). Male Wistar rats (Charles River laboratories) of 27 days or older are anesthetized by treating with Isoflurane and subsequent intraperitoneal injection of 20% Urethane. Then craniotomy is performed to remove 0.5 mm x 0.5 mm area of skull bone above the left hemisphere barrel cortex using stereotaxic coordinates (2.5 mm posterior and 5.5 mm lateral to bregma). Now the animal is ready for *in vivo* labeling. In order to perform the juxtasomal biocytin labeling, a glass pipette is filled with normal rat ringer supplemented with 2% biocytin and the pipette is mounted on a micromanipulator. The manipulator is set at an angle of 34° to the sagittal plane and hence perpendicular to the barrel cortex (specifically D2 barrel column). The pipette is lowered into the brain in steps of 1 µm till a single neuron is approached (indicated by an increase in electrode resistance) and action potential waveforms are recorded. After recording, the juxtasomal filling is carried out by applying positive square pulse current and gradually increasing the current applied. Membrane opening is indicated by the sudden increase in the frequency of action potentials. The biocytin electroporation sessions are repeated to get high quality axon fillings, which typically takes 5-10 minutes per neuron. Once the neuron is filled, pipette is moved back a few steps and the action potentials are recorded to observe whether normal waveform shape and frequency is returned, thus ensuring the recovery of neuron to normal condition. Now, in order to fill another neuron in the same animal, pipette is pulled back by 500 µm and shifted 20 µm - 50 µm in X-Y direction. Then the pipette is lowered again to locate another neuron at a desired depth and the filling process is repeated. The entire procedure is continued until 3 to 6 neurons are filled within the same animal. Figure 2.1A depicts the *in vivo* labeling procedure schematically.

After the completion of *in vivo* filling, the animal is transcardially perfused with 0.9% saline followed by 4% Paraformaldehyde (PFA). Then brain is surgically removed and post fixed with 4% PFA for 24 hours, transferred to 0.05 M phosphate buffer and stored at 4°C. Then, the left hemisphere of the brain is sliced tangential to the barrel cortex (at 45° angle). The thickness of each section is 50 µm and slices

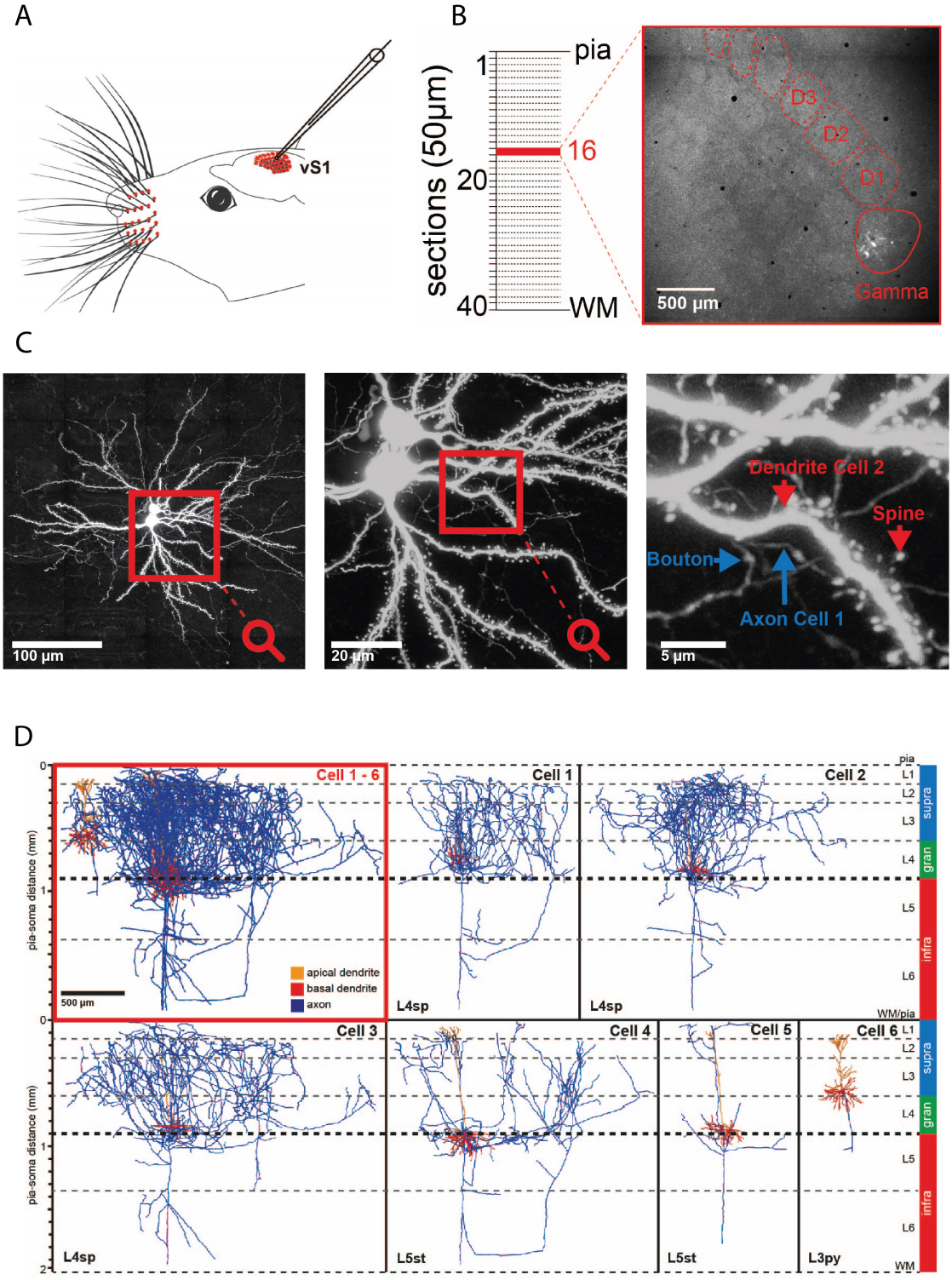

Figure 2.1. In vivo labeling and morphological reconstruction. A. Schematic of *in vivo* labeling of neurons in the barrel cortex. B. Maximum projection image of a

Figure 2.1. tangential cross section showing barrels and the labeled neurons (in the γ barrel). C. Somata of two labeled neurons shown at higher magnification. Zoomed panels to the right demonstrate high quality labeling, evidenced by the visibility of spines on the dendrites and boutons on the axons. D. Reconstructed neurons from an experiment. A total of six neurons are fully reconstructed from a single animal and disentangled using a semi-automated reconstruction process. Their morphological cell type has been identified.

range from pia to WM. Each section is then stained using Streptavidin Alexa Fluor™ 488 conjugate and mounted on a microscope slide. The slides are stored at 4°C.

A confocal laser scanning microscope (Leica TCS SP5 II, HCX PL APO) is used for imaging these tissue slides. To obtain the overview image of entire section 4x magnification is used, which provides a pixel resolution of 2.355 µm in the XY direction. At this magnification the barrels as well as the labeled neurons are visible (see Figure 2.1B). From this image the area of tissue that needs to be imaged at higher resolution is determined so as to ensure full coverage of all labeled neurites. A 3D image stack is then generated for each section using a step size of 0.5 µm in the axial direction (Z direction) and resolution of 0.092 µm in the XY direction. At this high resolution, not only the dendrites and axons but also the spines and boutons are visible, enabling the detection of putative synapses (see Figure 2.1C). Confocal microscope settings are detailed in (Slabik, 2018).

From these high resolution 3D image stacks, neuronal morphologies are reconstructed using an automated tracing software (Oberlaender et al., 2007). This software has been validated by analyzing the reconstructed neuronal morphologies, which have been presented in multiple publications (Bruno et al., 2009; Oberlaender et al., 2011, 2012). The software produces skeletal tracing of neurons in each section. These sectional tracings are manually proof edited and aligned across sections to form 3D neuronal morphologies, using a custom designed software (Dercksen et al., 2014). The manual proof editing involves the removal of excess spurious tracings and additional splicing of missing neurite tracings. During this process, the neurites are assigned to the respective neuron morphology using the image stack as reference, thus disentangling multiple neurons that are in close

proximity to one another. After reconstruction, these neurons are registered to the standard barrel field as described in (R. Egger et al., 2012). After registration, neurons are classified into morphologically defined cell types (Oberlaender et al., 2012; Narayanan et al., 2015). One such experiment where 6 barrel cortex neurons are reconstructed from a single animal and their cell type classification is shown in Figure 2.1D.

2.1.2 Putative synapse detection

I developed an algorithm to detect putative synapses between *in vivo* labeled, cell type identified, pairs of neuronal morphologies. The process has three distinct steps.

First, proximity zones are detected. Proximity zones are areas where the axon of one neuron is within a predefined distance from the dendrite of another neuron, while both axon and dendrite belong to the same animal (see Figure 2.2A). This proximity distance is determined to be 4 µm after systematic testing. Second, for each of the proximity zones detected, an image volume of 10 μm^3 is cropped from the section's image stack, with the mid point between the axon and dendrite apposition points being the center of the cropped volume (see Figure 2.2B). Third, each of the proximity zone image stack is manually inspected for one of the three following categories. One, there is no contact between dendrite and axon (as in Figure 2.2C). Two, there is an overlap of one voxel or more between spine and axon, but no bouton is visible (as in Figure 2.2D). These are called as "touch points" here-on. Third, there is an overlap of one voxel or more between spine and bouton (as in Figure 2.2E). These are termed as "putative synapses".

2.2 Generation of the facial nucleus reference frame

In this section, I describe the method used for verifying the trans-synaptic spread of the rabies virus following its administration into the intrinsic whisker muscle. This technique enables the delineation of brain-wide poly-synaptic networks that terminate at the intrinsic whisker muscle of rats. In order to achieve this, I developed a 3D local reference frame of facial nucleus (FN), since it is the termi-

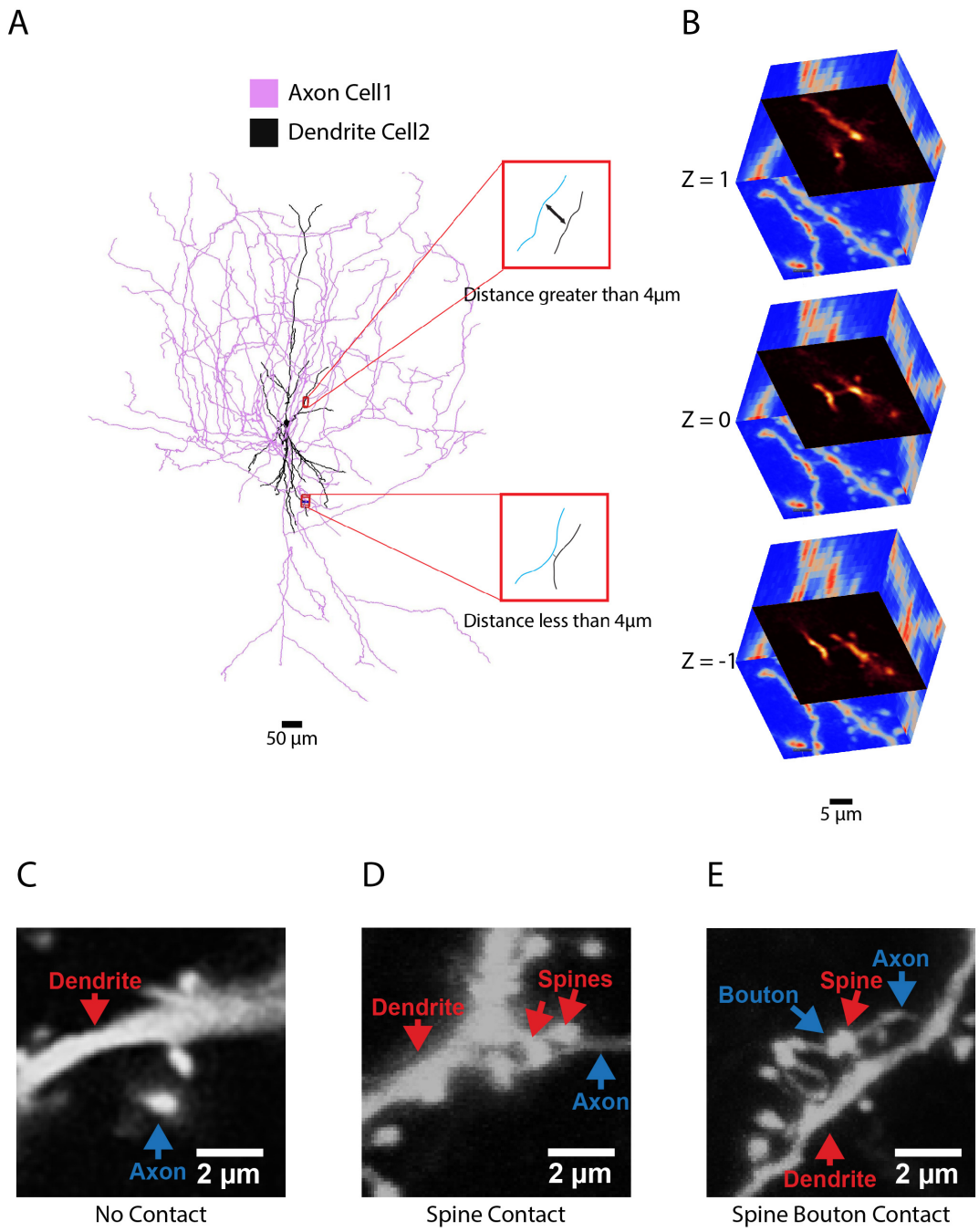

Figure 2.2. Putative synapse detection. A. Proximity zone detection scheme. Axon of cell 1 and dendrite of cell 2 are shown. All regions where the axon of cell 1 is more than 4 µm away from the dendrite of cell 2 are discarded (see example shown in the top in-set). All regions where distance is less than or equal to 4 µm are selected for further inspection (one such proximity zone is shown in the bottom in-set).

Figure 2.2. B. Putative synapse detection scheme. Each proximity zone image stack is manually inspected using the orthogonal image projections and scrolling through individual optical sections to see if there is any overlap between spine and axon/bouton. Three consecutive optical sections of one such proximity zone are shown here; where the central image (z=0) shows the overlap between spine and bouton. There are three possibilities for each proximity zone as shown in panels C,D,E. C. There is no overlap between axon and dendrite in the given proximity zone. D. There is an overlap between axon and spine but there is no bouton, also called as a "touch point". E. There is an overlap between bouton and spine, i.e., a "putative synapse".

nal brain region for the brain-wide whisker motor related networks and it houses motoneurons that innervate the whisker muscles and bring about whisker movement. I also developed the corresponding registration routine so that anatomical data from multiple experiments can be combined into a single reference frame in order to uncover the organizational principles of the FN. My colleague, Dr. Mike Guest carried out the experimental procedure, which includes: injecting retrograde cholera toxin and replication competent rabies viruses into the intrinsic whisker muscles, histology and image acquisition. I performed the following: detection of somata and contours of brain stem structures, reconstruction of vibrissal motoneuron (vMN) dendrites (with help from colleagues), generation of standardized FN reference frame, development of registration routines to combine anatomical data from different experiments into the standardized FN reference frame and generation of vMN map within the FN reference frame. This study was published in (Guest et al., 2017) and I am reproducing an abridged version of the method here.

2.2.1 Experimental procedure

Injections of retrograde tracers Male Wistar rats aged between 28 to 35 days were anaesthetized and placed in a stereotaxic frame. Targeted whiskers were identified by visualizing under surgical stereoscope (Leica MZ6) and marked at the base of the snout with a surgical pen. After clearing the fur around the target whisker and trimming the whisker, a small incision was made next to the target whisker follicle. A needle was inserted into the incision approximately 1

mm below the skin of the whisker pad using a manual micromanipulator. 500–700 nL of cholera toxin beta subunit (CTB) conjugated to AlexaFluor 488, 594 or 647 (Molecular Probes 1 mg/ml in PBS) or N2c strain of rabies virus (1 x 10^9 pfu/mL, 0.25–1.0 mL) was pressure injected either close to the base of the target whisker follicle (for CTB) or injected at the base of C3 whisker (for rabies virus) under visual control. Rats underwent a survival period of 6 days (for CTB) or 3-5 days (for rabies). The schematic of retrograde tracer injections into the whisker-specific intrinsic muscle is shown in Figure 2.3A. The rabies injection experiments were carried out by Dr. Guest at the University of Pittsburgh, under the guidance of Prof. Peter L Strick's lab. The handling of both the rabies virus as well as the infected animal has been detailed in previous studies (Kelly & Strick, 2000, 2003).

Histology After transcardial perfusion of rats, brains and right whisker pads were removed, fixed in Paraformaldehyde, blocked in 10% gelatin and fixed in 4% PFA overnight. Using a Vibratome, the brain stem was cut coronally with a section thickness of 50 µm and the whisker pad was cut sagittally with a section thickness of 150 µm. For rats injected with the rabies virus, sections were immunolabeled to visualize and count rabies labeled neurons (Alexa-488) and all NeuN labeled neuron somata (Alexa-647) in the brain stem. All sections were then mounted on glass slides and enclosed with cover slips.

Image acquisition Images of these slides were acquired using either a confocal laser scanning microscope (Leica SP5 for rabies experiments) or a fluorescence widefield microscope (BX51, Olympus for CTB experiments). For the CTB experiments sequential channel widefield images were obtained for the FN and whisker pads. 2 x 2 fields of view of the FN were imaged using a 10x dry objective (which provides a voxel resolution of 0.926 x 0.926 x 0.5 µm) and 7 x 9 fields of view of the whisker pad were imaged using a 4x dry objective (at a voxel resolution of 2.303 x 2.303 x 0.5 µm). For rabies experiments, dual channel confocal mosaic scans were obtained (one for rabies and one for NeuN), spanning the entire brain stem, using a glycerol objective having 10x magnification which translates to a pixel resolution of 0.868 x 0.868 µm. For counting NeuN labeled neuron somata within the FN, single channel confocal mosaic image stacks of volumes up to 3 x

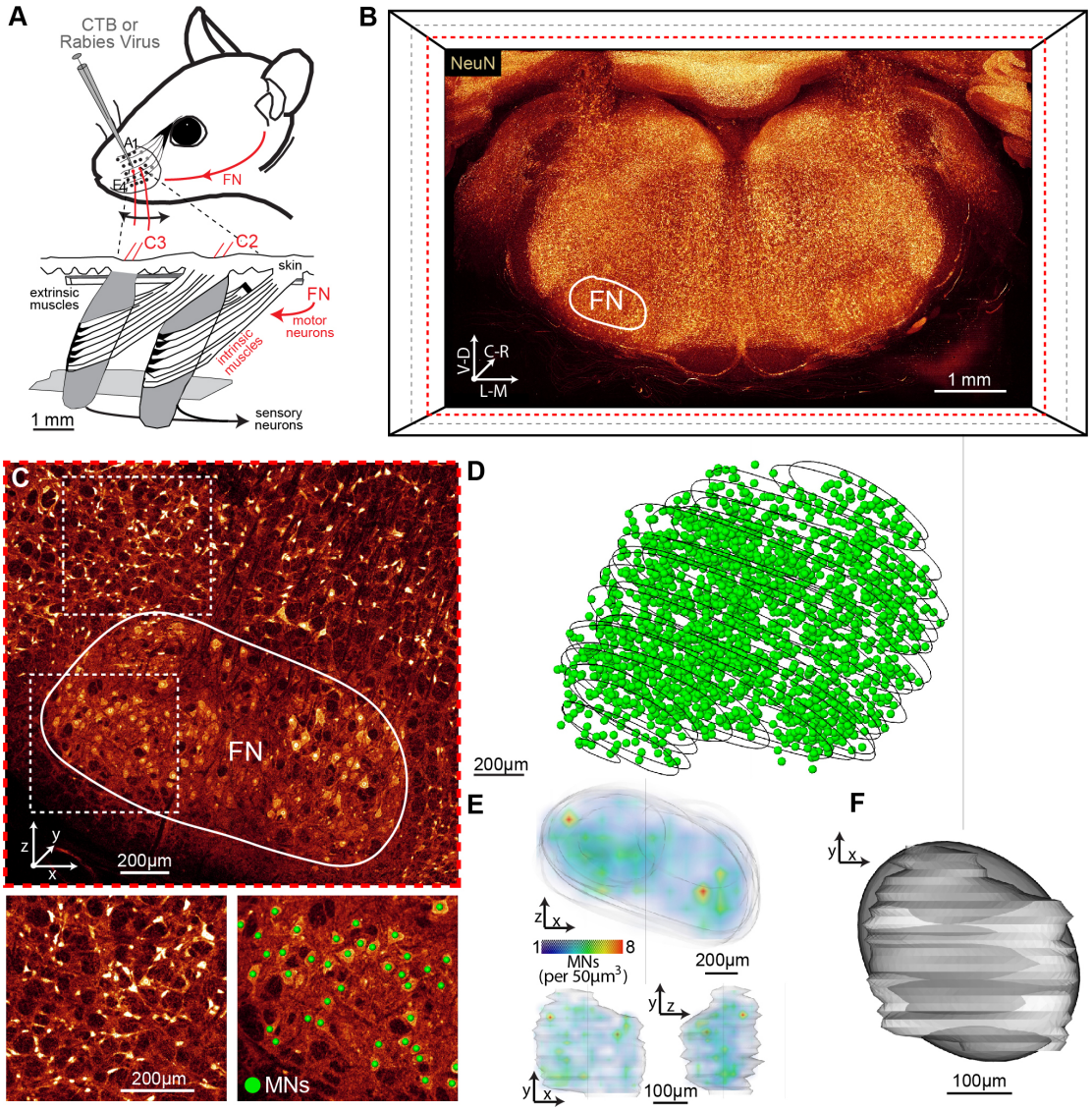

Figure 2.3. Generation of the FN reference frame. A. Schematic of whisker musculature, illustrating the intrinsic and extrinsic muscles involved in whisker motor control (adopted from (Berg & Kleinfeld, 2003)). CTB and trans-synaptic rabies virus were injected into the intrinsic whisker muscle in order to delineate the organization of the vMNs within the rat FN. B. The coronal view of brain stem, showing the maximum projection image across all histological brain sections that comprise the FN. Orientation convention followed is such that the lateral-medial (L-M) is along the x-axis, caudal-rostral (C-R) axis is along the y-axis and ventral-dorsal (V-D) axis is along the z-axis. Brain stem images are reflected about the mid-line so that the targeted FN (right hemisphere) is seen on the left hemisphere. All brain stem sections have been labeled with NeuN so that all somata can be located. C. Higher magnification view of the FN from panel B. It also shows the

Figure 2.3. contour of the FN, which has been drawn using the criteria exemplified in the below panels. Neurons inside the FN have bigger somata (bottom-right panel) compared to those outside the FN (bottom-left panel). The soma centers of neurons inside the FN are marked with green spheres. D. 3D contours of the FN with all somata inside it marked by green spheres for the example shown in panels B and C. E. 3D locations of the FN somata shown in the previous panel are converted into a 3D density map using a resolution of 50 μm^3. The density map shows that there are two areas of higher density, one medial and the other lateral, separated by an area of lower density in between. F. The FN volume has been approximated by an ellipsoid. This figure is adopted from (Guest et al., 2017).

1.5 x 0.05 mm were acquired using a 20x glycerol objective (at a voxel resolution of 0.361 x 0.361 x 1 µm). In order to obtain the dendritic reconstructions of the rabies-positive vMNs in the FN, maximum magnification 63x glycerol objective (providing a voxel resolution of 0.092 x 0.092 x 0.5 µm) was used to obtain single channel confocal mosaic image stacks of volumes up to 1 x 1 x 0.05 mm.

2.2.2 Detection and reconstruction of anatomical data

Detection of somata/contours of the brainstem structures The center location of all NeuN and rabies labeled somata in the brain stem as well as all CTB labeled neuron somata in the FN are detected manually using the visualization software Amira (Stalling, Westerhoff, & Hege, 2005). All brain stem images were aligned to each other with respect to the mid line and the ventral edge (see Figure 2.3B). Contours of the brain stem were drawn using Filament Editor tool of the Amira software (Dercksen et al., 2014). Contours of FN were detected based on the size differential between the somata of vMNs in the FN and the somata of other neurons outside the FN (vMNs are bigger in size). Then, contours of the FN were drawn using the Filament Editor software. Other brain stem nuclei were contoured by comparing them to the Paxinos Rat Atlas (Paxinos & Watson, 2006). This soma detection and contouring scheme has been illustrated in Figure 2.3C,D. Furthermore, NeuN somata density was calculated using a resolution of 50 μm^3 in order to delineate the cellular organization of the FN (see Figure 2.3E).

Reconstruction of dendrites In order to reconstruct the dendrites of rabies labeled neurons, the high resolution image stacks were deconvolved using linear Tikhonov-Miller algorithm and a point spread function (that is calculated based on the confocal microscope's parameters) using Huygens software (SVI, Netherlands). This method has been published previously (Oberlaender, Broser, Sakmann, & Hippler, 2009). Manual tracing was performed in these deconvolved image stacks to obtain neuronal structures using the Filament Editor in the Amira software. These tracings were then aligned and spliced across consecutive histological slices using the Filament Editor to obtain 3D reconstructions of rabies labeled dendrites.

2.2.3 Generation of the facial nucleus reference frame

Ellipsoid approximation of the FN Contours of the FN were approximated by an ellipsoid, solving the following equation of quadric surfaces:

$$A'x^2 + B'y^2 + C'z^2 + 2D'xy + 2E'xz + 2F'yz + 2G'x + 2H'y + 2I'z + J' = 0 \quad (2.1)$$

Equation 2.1 has 10 parameters. By multiplying this equation by $-1/J'$ we can reduce the number of parameters to 9 as follows:

$$Ax^2 + By^2 + Cz^2 + 2Dxy + 2Exz + 2Fyz + 2Gx + 2Hy + 2Iz = 1$$

Which can be written in the form of matrices:

$$PQ = R$$

Where,

$P_i = [x_i^2, y_i^2, z_i^2, 2x_iy_i, 2x_iz_i, 2y_iz_i, 2x_i, 2y_i, 2z_i]$; is the i^{th} row of Nx9 matrix P

$Q = [A, B, C, D, E, F, G, H, I]^T$; is the vector of unknown parameters

$R = [1, ...1]^T$; is the unit vector of length N

N = Number of data points defining FN contours

In order to obtain an ellipsoid that best approximates the FN volume, Q must minimize the squared errors between P and R. In closed form, Q is estimated by linear least squares (LLSQ) method as:

$$Q = (P^TP)^{-1}P^TR$$

An ellipsoid is a special case of quadric surfaces and is defined as:

$$x^2/a^2 + y^2/b^2 + z^2/c^2 = 1 \tag{2.2}$$

Where, a,b and c are half axes or radii of the three principal axes of the ellipsoid. Comparing equation 2.2 with 2.1, A,B and C represent inverse squares of the ellipsoid half axes.

Equation 2.1 can then be written in matrix form as:

$$X\beta X^T = 0$$

Where,

$X_i = [x_i, y_i, z_i, 1]$; i^{th} row of Nx4 input data matrix X

$$\beta = \begin{bmatrix} A' & D' & E' & G' \\ D' & B' & F' & H' \\ E' & F' & C' & I' \\ G' & H' & I' & J' \end{bmatrix}$$; 4x4 symmetric matrix of known quadric parameters

The ellipsoid principal axes (PAs) and their radii are computed by the Eigen decomposition of the first 3 rows and columns of β. The Eigen vectors represent the PAs and Eigen values represent the radii. Ellipsoid approximation of FN volume has been illustrated in Figure 2.3F.

Generation of the FN reference frame The aforementioned ellipsoid approximation method was applied to three facial nuclei of three different rats. The resulting FN ellipsoids are then combined to create an average ellipsoid which serves as the standard FN reference frame. The lengths and orientations of the PAs of this reference ellipsoid are determined to be the average of the lengths and orientations of the PAs of the input ellipsoids. The centroid of this average ellipsoid serves as the origin of the reference frame. The three orthogonal axes of the reference coordinate system (X,Y,Z) are chosen to be the PAs of the average ellipsoid that are most parallel to L-M, C-R and V-D axes respectively.

Registration to the FN reference frame The anatomical data (like soma distributions or morphological reconstructions) obtained from the FN of different animals can be registered into the standard FN reference frame using affine transformations as follows. For the animal of interest, FN contours are drawn as

mentioned above. The FN contours are then approximated by an ellipsoid. This ellipsoid is first translated to match its center with that of the standard ellipsoid. Then it is rotated to match its PAs with that of the standard ellipsoid. The PAs are then scaled independently so that each PA length matches the corresponding lengths of the PAs of the standard ellipsoid. The resulting affine transformation is then applied to the anatomical data that needs to be registered, thus incorporating data from different FN into the standard FN reference frame.

2.3 Generation of the vibrissal motor cortex reference frame

In the previous section, I described the method for generating the rat FN reference frame, where the criteria used for identifying the FN was the size differential of neuronal somata (MNs within the FN were bigger than the somata surrounding the FN). In this section, I will describe a method for defining and generating local reference frame for a brain region which has no visible anatomical landmarks for identifying its boundaries. In order to do so, I use the synaptic distance of the neuronal population (of the brain region under consideration) from a terminal muscle as the defining criteria. Specifically, I define and generate the vibrissal motor cortex (vM1) reference frame using third-order rabies labeled cortical neurons as defining landmarks. The methods for injecting replication-competent rabies virus into the intrinsic whisker muscle as well as the subsequent histology and imaging have been described in the previous section. The time-dependent retrograde progression of rabies virus and the definitions of trans-synaptic orders of labelling are described in the results section (see 3.2.3). In the current section, I focus on the third-order animals (where the rabies labeling is limited to layer 5 of the cortex) and describe the methods for the following: generation of vM1 reference frame using third-order rabies-positive cortical neurons, definition of vM1 layer borders using soma density profiles and registration of neuronal morphologies onto the vM1 reference frame.

2.3.1 Generation of the vM1 reference frame using third-order rabies-positive cortical neurons

Quantification of third-order rabies-positive cortical neurons After injecting the replication-competent rabies virus into the intrinsic muscle of C3 whisker, rats were sacrificed after a survival period of 3-5 days. Cortices were sliced coronally (or tangential to the barrel cortex) into 50 µm thick sections and doubly immunolabeled for rabies and NeuN quantification. These sections were imaged using a laser confocal microscope at a voxel resolution of 0.361 x 0.361 x 1 µm (see 2.2.1 for details of these methods). In each section, Pia and white matter (WM) contours were traced using the Amira software (Stalling et al., 2005). Rabies-positive neurons were quantified manually by marking the center location of their somata in high resolution 2D images of brain sections using the Amira software. NeuN stained neuronal somata were quantified using a custom designed algorithm, which has a 96% accuracy in detecting NeuN positive neuronal somata and has been reported previously in (Oberlaender, Dercksen, et al., 2009). Figures 2.4B-D depict the high resolution imaging and the subsequent quantification of NeuN and rabies labeled somata. Brain sections that were sliced tangential to the barrel cortex were aligned to one another using barrels and blood vessels as reference landmarks as describe in (R. Egger et al., 2012). Coronally sliced brain sections were aligned using the method outline in (Park, 2018). Briefly, this method involves two main steps. First, the consecutive coronal sections are aligned to one another based on the mid-line. Second, alignment is refined in the sagittal plane by moving each section up or down in the sagittal plane to best match the reference curvature of the cortex in the sagittal plane as per the Paxinos rat atlas (Paxinos & Watson, 2006). Along with each brain section's Pia and WM contours, rabies-positive (and NeuN labeled) cortical soma locations belonging to that brain section were also aligned. Figure 2.4A shows the top (axial) view of the aligned Pia contours. A 3D iso-surface of Pia and WM are generated from the aligned 2D Pia and WM contours using the method described in (R. Egger et al., 2012). Briefly, it involves the following steps. First, the aligned 2D contours of Pia and WM are converted into respective binary image volumes using a distance transform, such that the voxels inside the Pia (or WM) are set to be high and voxels outside are

set to be low. A voxel resolution of 50 µm was used to generate the image volume. Second, the 3D binary image volume is converted into an iso-surface using the "marching cubes" algorithm (Lorensen & Cline, 1987). The surface triangulations were then smoothed to the desired level by using a low-pass filter which uses a windowed sinc function as the interpolation filter. The filter was iterated 20 times with a pass band value of 0.01 to obtain a smoother surface mesh with a more uniform distribution of vertices. The details of this algorithm can be found in (Taubin, Zhang, & Golub, 1996). Figure 2.4E shows axial view of the 3D Pia surface of a third-order rat brain along with its rabies-positive cortical soma locations, whereas 2.5A shows the same surface after smoothing. The image processing and surface generation algorithms utilized here were implemented in ITK (Johnson, McCormick, & Ibanez, 2015) and VTK (Schroeder, Martin, Lorensen, & Kitware, 2006) software libraries.

Clustering of the third-order rabies-positive cortical neurons The exact number and location of the third-order cortical neurons labeled by the rabies virus can vary across different third-order animals. Therefore, in order to find the cortical regions labeled consistently across animals, I have removed outliers by clustering rabies-positive cortical neurons. The method involves two major steps. First, the cortical neurons are segregated into two clusters (in each hemisphere) using the "k-means" clustering method (MacQueen, 1967). Figure 2.5A shows the resulting two clusters, color coded for sensory cortex and motor cortex respectively, in each hemisphere. The initial cluster centers are set near the barrel cortex and motor cortex (rostral) respectively in each hemisphere. Second, the tentative sensory and motor cortex rabies clusters obtained from the previous step are converted into a density image volume (see 2.5B). This is done by counting the number of neurons within each voxel with a grid resolution of 400 µm. This density image is created individually for each of the four clusters (vM1 left, vM1 right, vS1 left and vS1 right) for each animal. The peak densities vary across clusters as evidenced by the density color maps of each cluster (see 2.5B). The density image volumes are then binarized using a lower threshold which is a percentage of peak density. The iso-contours corresponding to the binary image volumes obtained using lower thresholds which are 100%, 50% and 10% of peak density are shown in yellow, red

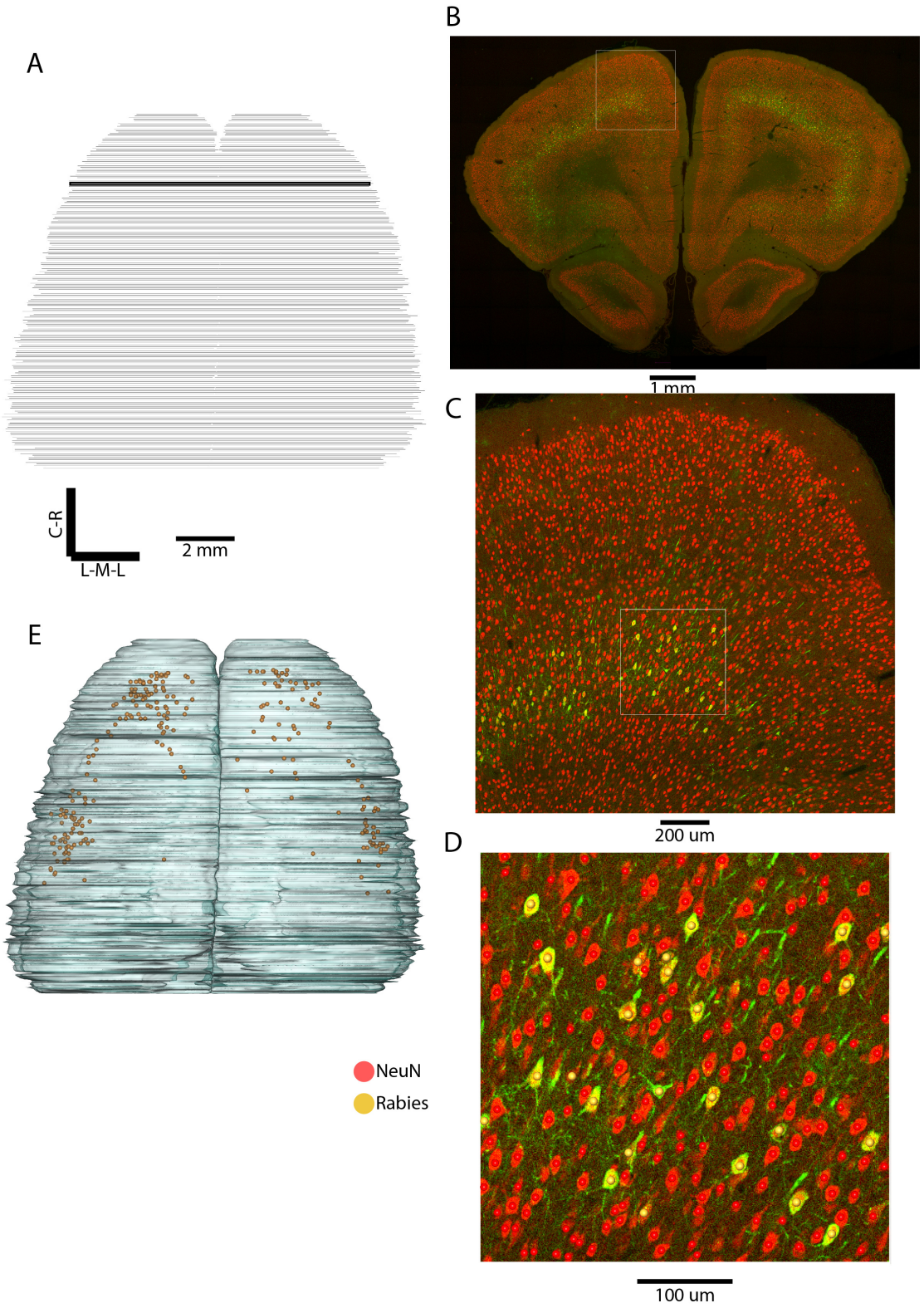

Figure 2.4. Quantification of NeuN and rabies-positive cortical neurons. A. Top

Figure 2.4. (axial) view of aligned Pia contours of a third-order rat brain. B. High resolution confocal image of a coronal brain section (highlighted in panel A) that has been doubly immunolabeled with Alexa Flour florescent dyes for identifying NeuN and rabies-positive neuronal somata. C. Higher magnification zoom-in of an image crop highlighted in panel B, showing the NeuN and rabies-positive somata. D. Zoom-in of a small image snippet from panel C, where the center location of NeuN and rabies-positive somata have been marked and color coded (red for NeuN and yellow for rabies-positive neurons). The images have been color enhanced for better visualization. E. 3D iso-surface of Pia generated from the aligned 2D Pia contours shown in panel A. The 3D locations of the third-order rabies-positive somata are also shown.

and blue colors respectively in 2.5B. A threshold of 10% of peak density is used for removing the outliers, which means that neurons belonging to density image voxels that have a value greater than 10% of peak density are selected as valid and rest of the neurons are treated as outliers.

Generation of the rabies defined vM1 reference frame After clustering and removing the outliers, the brain regions spanned by the third-order rabies-positive cortical neurons are extracted to generate the local reference frames as follows. For each validated rabies cluster, the principal axes (PAs) of the soma distribution are obtained through the PCA. In the case of the vM1 cluster, the first (and the largest) PA is most parallel to the sagittal plane (along C-R axis), the second PA is most parallel to the coronal plane (along L-M axis) and the third is most perpendicular to the axial plane (along V-D axis) (see 2.5C). The first and second PAs are extended from the center of the cluster till the farthest rabies-positive neuron of the cluster in each direction. The third principal axis is extended to intersect Pia and WM. These PAs respectively form the new Y,X and Z axes of the coordinate system in the local reference frame, with the centroid of rabies cluster being the new origin. In order to extract the volume of the region spanned by the rabies neurons (in other words the boundaries of the local reference frame), four planes that bound the region between Pia and WM need to be obtained. These clipping planes are found such that they pass through the end points of the first and second PAs and their orientation represents the local orientation of the

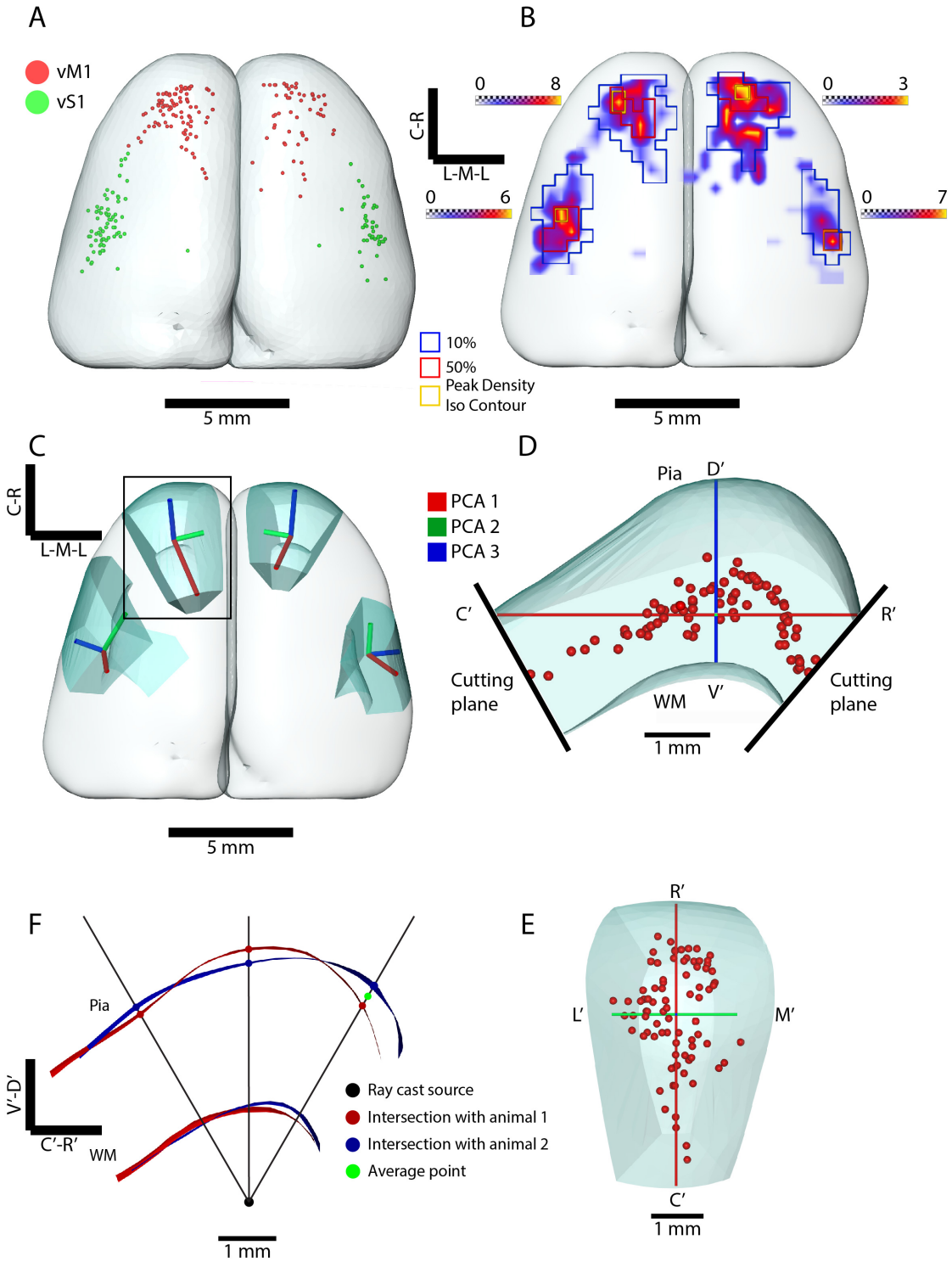

Figure 2.5. Generation of the rabies defined local reference frames. A. Top view of a cortical surface which has third-order rabies-positive neurons. The surface mesh is generated using a voxel size of 300 µm for smoother visualization. The rabies-

Figure 2.5. positive neuronal somata are clustered into tentative vM1 and vS1 groups in each hemisphere using 'k-means' clustering method (clusters are shown in red and green colors respectively). B. Tentative clusters (shown in panel A) are further cleaned up by removing outliers using density based clustering. Density image of each cluster is shown as a maximum projection onto the axial plane. These density image volumes are generated using a voxel size of 400 µm and binarized using a threshold expressed relative to the peak density of the cluster. The iso-contours corresponding to the iso-surfaces generated by lower thresholds of 10% of peak density, 50% of peak density and equal to the peak density are shown with blue, red and yellow colors respectively. C. The local reference frames generated by rabies clusters corresponding to 10% iso-contours along with the PAs. The PAs are color coded with red, green and blue respectively. D. vM1 of the left hemisphere from panel C shown in sagittal view of its local reference frame. L'-M', C'-R' and V'-D' axes are X,Y and Z axes of the local reference frame respectively. The origin is the centroid of the rabies cluster. The clipping planes at the end points of C'-R' axis are visualized with thick black lines. It can be seen that the reference vM1 volume spans to include exactly till the extreme rabies neuron somata of the cluster. E. Top view of the vM1 volume (shown in panel D) in its local reference frame along with the rabies cluster (in red) that was used to generate it. F. Illustration of the "Ray Cast" method used to generate the average Pia and WM surfaces. Clipped parts of the Pia and WM surfaces of two animals (that have been aligned) are shown in sagittal view and color coded as red and blue respectively. Rays are cast from the centroid of aligned Pia and WM surfaces (ray cast source shown as black dot). Each ray intersects the Pia and WM surfaces of individual animals and their points of intersections are color coded as red and blue respectively. For each ray, the average of the individual intersection points w.r.t. Pia and WM are calculated (shown in green for an example ray intersecting the Pia). These average points represent the average Pia and WM surfaces of the aligned surfaces.

cortex at the point of intersection between the clipping plane and the end point of the PA. The local orientation of the cortex at the end point of PA is approximated by drawing normals from WM to Pia within a radius of 1 mm around the end point of PA. Once the four clipping planes are determined, they are used to clip the desired part of Pia and WM (which spans the rabies-positive neurons). The four clipping planes together with the clipped Pia and WM surface triangulations (mesh) form the local reference frame volume (see 2.5D,E). The same procedure is repeated for each of the four rabies clusters individually and the resulting four

reference frames along with their PAs are shown in 2.5C for an example animal.

Alignment of anatomical landmarks In order to generate the average Pia and WM surface meshes from individual Pia and WM surfaces of different animals, the surfaces are first aligned to each other hemisphere-wise as follows. First, the center of mass of Pia and WM surface meshes of each animal is translated to match the center of mass of Pia and WM of reference animal (one of the animals is treated as reference animal). Second, The PAs of each animal's Pia and WM (obtained through the PCA) are aligned to the respective PAs of Pia and WM of the reference animal. Third, the distance between the Pia surface of each animal and the reference animal are minimized using the Iterative Closest Point (ICP) algorithm (Besl & McKay, 1992; Zhang, 1994). This algorithm aligns the two surfaces by minimizing the distance between the vertices of the two surfaces in the least square sense. The distances are calculated between each vertex of the surface to be aligned and the closest vertex on the reference surface. The resulting transformation is applied to the surface being aligned and the process is iterated till convergence is reached. This global hemispheric alignment is further fine tuned by aligning the vM1 and vS1 rabies cluster iso-surfaces using the ICP algorithm. All relevant anatomical landmarks (such as rabies clusters, PAs and local reference frames) are aligned along with the Pia and WM surfaces. In addition to the global alignment, local alignment of rabies defined local reference volumes as well as rabies cluster iso-surfaces were also performed using the aforementioned ICP algorithm.

Quantification of the precision After aligning the anatomical landmarks to one another, the quality of those alignments were quantified. In other words, how precisely can these landmarks be aligned to one another is quantified. The precision of aligning the cortical hemispheres is quantified at three levels: Pia surface, WM surface and center of mass of the hemisphere. In order to quantify the Pia and WM surface precision, an axis field is generated for each aligned hemisphere. The axis fields consist of uniformly distributed vector normals drawn from WM surface to Pia surface. For each vector in the reference axis field the nearest vectors in the aligned surfaces are determined. Along with the vectors, their respective points of intersection with the Pia and WM surfaces are determined as well. Now, for each

set of points of intersection at Pia and WM (corresponding to each vector normal of the reference surface), their centroid is determined and the euclidean distances between each point of intersection in the set and their centroid are computed along with their mean distance. The precision at Pia and WM surfaces respectively are now given by the mean euclidean distance (of each set of points of intersection) averaged across all vectors of the reference axis field. In addition to the euclidean precision angular precision is also computed, as the mean angle between the set of matched vectors averaged across all vectors of the reference axis field. The precision at the center of the hemisphere is computed from the set of centroids of each hemisphere in the same fashion as mentioned above. The aforementioned method of quantifying hemispheric precisions is followed to quantify the precision of rabies defined vM1 and vS1 reference frames as well.

Generation of the standard vM1 reference frame Having aligned the Pia and WM surfaces of each animal, the average Pia and WM surfaces are generated as follows. First, the Pia and WM surfaces are uniformly sampled using the "Ray Cast" approach (see 2.5F). In this method, a sphere having 1 µm radius and 14400 faces is placed at the center of mass of aligned Pia and WM surfaces; and vector normals (rays) are drawn from each face of sphere and extended till it intersects the Pia and WM surfaces. The point of intersection of each ray as it intersects each aligned Pia and WM surface is detected and their average point is computed. The average intersection points thus generated from ray casting represent the average Pia and WM surfaces of each hemisphere. Convex hulls for Pia and WM surfaces are generated from the respective average points using 3D Delaunay triangulations (Bowyer, 1981; Watson, 1981). After generating the average hemispheric surfaces (Pia and WM), standard rabies defined vM1 reference frame is created as follows. First, the center (origin) of the standard reference frame is determined as the mean of aligned rabies cluster centers of individual animals. The orientation of the standard reference frame is determined as the average of respective PAs of individual reference frames; with the extent of average PAs being the mean of respective PAs of individual reference frames. Given the center and PAs of the average reference frame, the standard reference frame volume is derived from the average Pia and WM surfaces by employing the same method used for

deriving individual reference frame volumes. The average Pia surfaces along with the standard reference frames are visualized in the result section (see Figure 3.19 D).

2.3.2 Derivation of the layer borders

In the previous subsection, I have explained the methods for generating the vM1 reference frames from third-order rabies-positive cortical neurons. In this subsection, I will describe the methods for delineating the cellular organization of the vM1 reference frame.

Generating the neuronal density profiles In order to obtain the layer borders of the vM1, neuronal density profiles are obtained as follows. First, the center locations of all neuronal somata of vM1 that are stained by NeuN are extracted from the 2D confocal images of cortical brain sections of third-order animals as explained previously (see 2.3.1). Second, the local orientation of the vM1 reference frame is approximated by generating an axis field that consists of vectors drawn from WM to Pia distributed uniformly throughout the reference frame. In order to distribute these vectors uniformly throughout the reference frame, a rectangular grid having a resolution of 500 µm^3 is generated, whose center is the center of the reference frame and whose length and breadth are equal to the extents of first two PAs of the reference frame respectively. The grid is rotated so that its sides are parallel to the first two PAs of the reference frame. At each vertex of this grid a vector is drawn from WM to Pia which represents the local orientation within a neighborhood of 800 µm radius. Top view of such vM1 axis fields are shown for a coronally sliced third-order animal in Figure 2.6A, where each vector is visualized as a cylinder of 250 µm radius. Third, having generated uniform axis field for the vM1 reference frame, all NeuN labeled somata whose center locations fall within the axis field cylinders of 250 µm radius are extracted (see Figure 2.6 B). For each such cylinder, a neuronal density profile is generated, traversing along the axis of the cylinder in steps of 50 µm from Pia to WM. The process starts by creating a smaller cylinder, which is a segment of the axis cylinder but has a height of 50 µm and whose center is 25 µm below Pia; and counting the number of

neuronal somata within this segment of the cylinder. Given the number of neurons within this segment of cylinder and the volume of this segment of cylinder, the density is computed for this segment of the profile. This small cylinder is moved along the axis in steps of 50 µm, measuring the density at each step, until the WM is reached. Thus, neuronal density profiles are obtained for each vector of the vM1 axis field. Since vectors (and hence the corresponding profiles) have different lengths, all profiles are normalized to average length of the central axes of vM1 reference frames across three third-order animals, which was found to be 2600 µm. Normalization is achieved using the univariate cubic spline interpolation technique (Marsden, 1974). All normalized profiles are averaged and such an average (±SD) neuronal density profile is shown in Figure 2.6C for the vM1 reference frame of the LHS of the third-order animal shown in Figure 2.6A.

Deriving the layer borders from the neuronal density profiles After obtaining the neuronal density profiles of the vM1 reference frame, the layer borders were derived from these profiles as follows. The profiles show the variation of neuronal density along the cortical depth of the vM1. The lower border of layer 1 (L1) was defined as the cortical depth (from Pia) at which the neuronal density was maximum within the cortical depth of 300 µm from the Pia. The lower border of layer 2/3 (L2/3) was defined as the cortical depth at which the density profile peaked, traveling further along the cortical depth. The lower border of layer 5A (L5A) was defined as the cortical depth at which the density profile reached its minimum value traveling further along the cortical depth. The lower border of layer 5B (L5B) was defined as the cortical depth at which the density profile peaked again going along the cortical depth. The lower border of layer 6 (L6) was the WM surface. This process was followed for each density profile of the vM1 and the average of their layer border depths for each layer is depicted in the Figure 2.6C for the left vM1 shown in panel A. For each vector of the vM1 axis field, the layer borders are demarcated and using those points, the layer border surfaces were generated for all layers using Delaunay triangulations as mentioned in 2.3.1 (Bowyer, 1981; Watson, 1981).

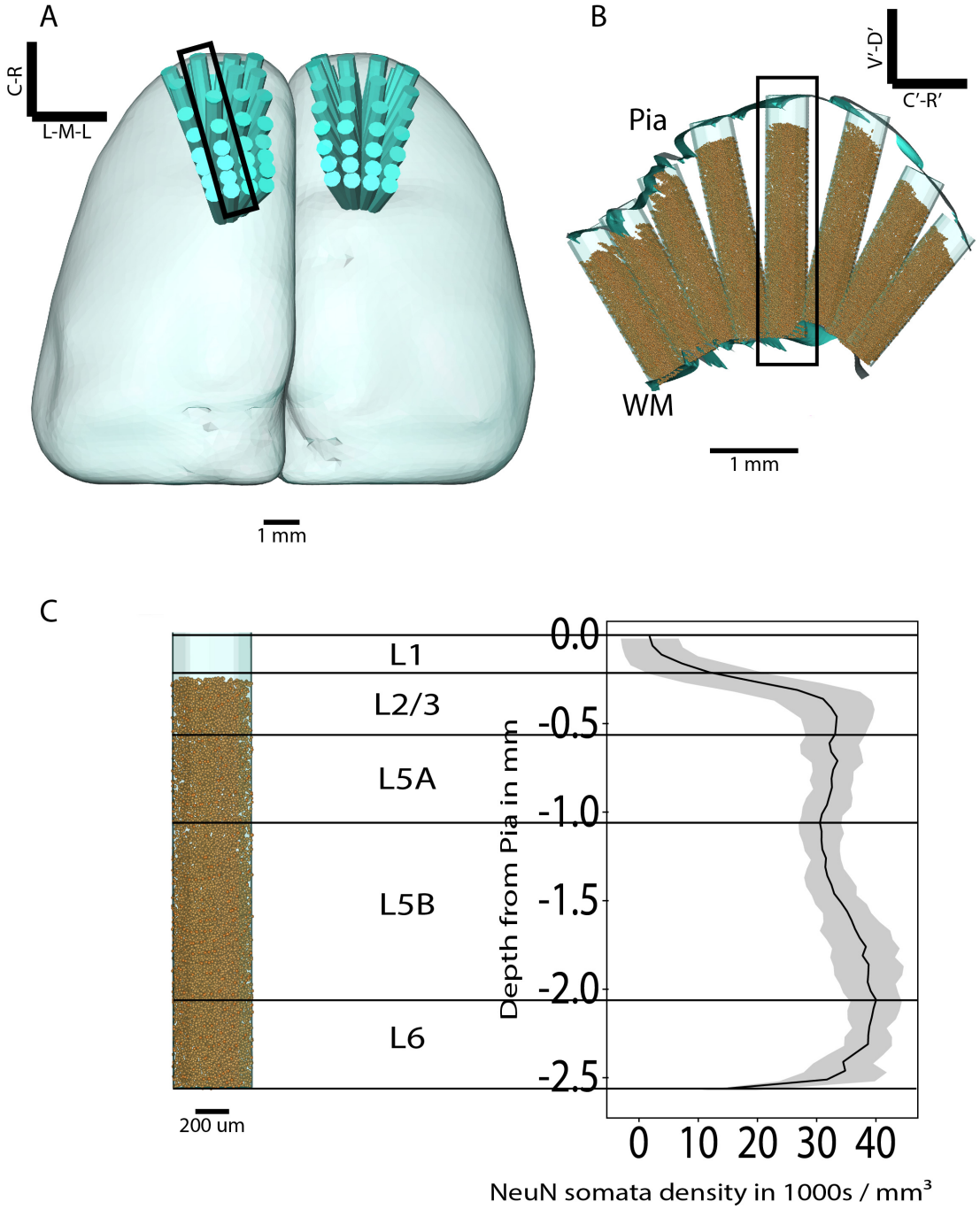

Figure 2.6. Deriving the vM1 layer borders from the neuronal density profiles. A. Top view of the Pia surface of a third-order rat brain in which the vM1 reference frames of both hemispheres are spanned by uniformly distributed axis fields. Each vector of the axis field is shown as a cylinder of radius 250 µm. B. Side (sagittal) view of the left vM1 in its local reference frame view, where only the vectors corresponding to the first PA are shown (highlighted in panel A). Each vector

Figure 2.6. shows the center locations of all NeuN somata (extracted from the 2D section images) that lie within its bounds. C. Left: the central axis of the vM1 reference frame highlighted in panel B. Right: Average density profile of the left vM1 reference frame (shown in panel A), where the density profile has been averaged across all normalized density profiles (corresponding to each vector of the axis field) and the error band (grey shaded area) represents their standard deviation. The density profile varies as we traverse along the depth of the cortex from Pia to WM. The layer borders are derived from these density variations along the cortical depth. The average layer borders for each layer are shown as black horizontal lines. These borders have been averaged across the respective borders obtained for each density profile throughout the vM1 axis field of the LHS (shown in panel A).

Delineating the cellular organization of the vM1 reference frame The detection of the center locations of NeuN labeled somata was performed by imaging a single optical section at the middle of each cortical brain section. However, in order to obtain the total number of neurons within the vM1 reference frame, the cell counts obtained from the 2D optical sections need to be scaled to the 3D brain sections. This was performed by imaging multiple optical sections at a resolution of 0.5 µm for each 50 µm thick brain section within the vM1 central axis of the LHS of one of the three third-order animals. This central axis was also imaged in 2D as mentioned before. Then, the cell counting was performed for the central axis in both 2D and 3D image stacks. Density profiles were generated for the central axis using both 2D and 3D cell counts. Using the average layer borders of the vM1 (derived as mentioned before using the entire axis field of the vM1), the layer-wise 2D to 3D scaling factors were obtained by dividing the peak neuronal density of each layer in the 3D profile by the respective peak densities in the 2D profile. These layer-wise scaling factors were then applied to each vM1 reference frame in order to scale the neuronal counts in a layer-wise manner. Having obtained the layer-wise neuronal counts, the volume and neuronal density of each layer was measured for all vM1 reference frames. The methods described above for delineating the layer borders of the vM1 reference frames were also applied to obtain the layer borders of the barrel cortex reference frames. Instead of using the vectors of the axis field, in case of the barrel cortex, the neuronal density profiles of C2, D2, C3 and D3

barrel columns were used to derive the layer borders. Additionally, similar to the generation of neuronal density profiles of the NeuN labeled somata, the density profiles were also generated for the rabies labeled somata in order to quantify the proportion of rabies labeled somata that lie within layer 5.

2.3.3 Registration of neuronal morphologies to the vM1 reference frame

I have described the methods for delineating the geometric and cellular organization of the vM1 reference frame in previous subsections. In this subsection, I describe the method for registering neuronal morphologies to the vM1 reference frame, whereby its morphological organization can be delineated. Dr. Rajeev Narayanan reconstructed 3D morphologies of neurons belonging to the vM1 region. The target neurons were sampled from the M1 region, whose location was defined by the stereotaxic coordinates provided by the Paxinos rat brain atlas (Paxinos & Watson, 2006). The methods employed for *in vivo* labeling, histology, high resolution imaging and semi-automated reconstruction of neuronal morphologies were similar to those detailed in (Narayanan et al., 2014). I developed the registration routine which registers these 3D morphologies into the vM1 reference frame.

The registration was performed in two major steps. First, Pia and WM isosurfaces of the rat cortex (from which the neuron has been reconstructed) were reconstructed using the method explained in (R. Egger et al., 2012) (see 2.3.1). The Pia and WM surfaces were then registered to the vM1 reference frame's Pia and WM surfaces (LHS), first by aligning the respective PAs and then by minimizing the surface errors using the ICP algorithm (Besl & McKay, 1992; Zhang, 1994) (see 2.3.1). The resulting transformation thus obtained was then applied to the neuron being registered. Second, this surface based neuron registration was further refined by rotating neuron's original axis to match the local orientation of the reference frame at the registered soma location. Neuron's axis was determined by finding the principal direction of its apical dendrite using the PCA. For neurons that lack the apical dendrite (and for neurons whose soma lie within 500 µm below the Pia surface before registration), their axis was determined by the local orientation of the cortex at the location of the soma. The local orientation of the cortex at the

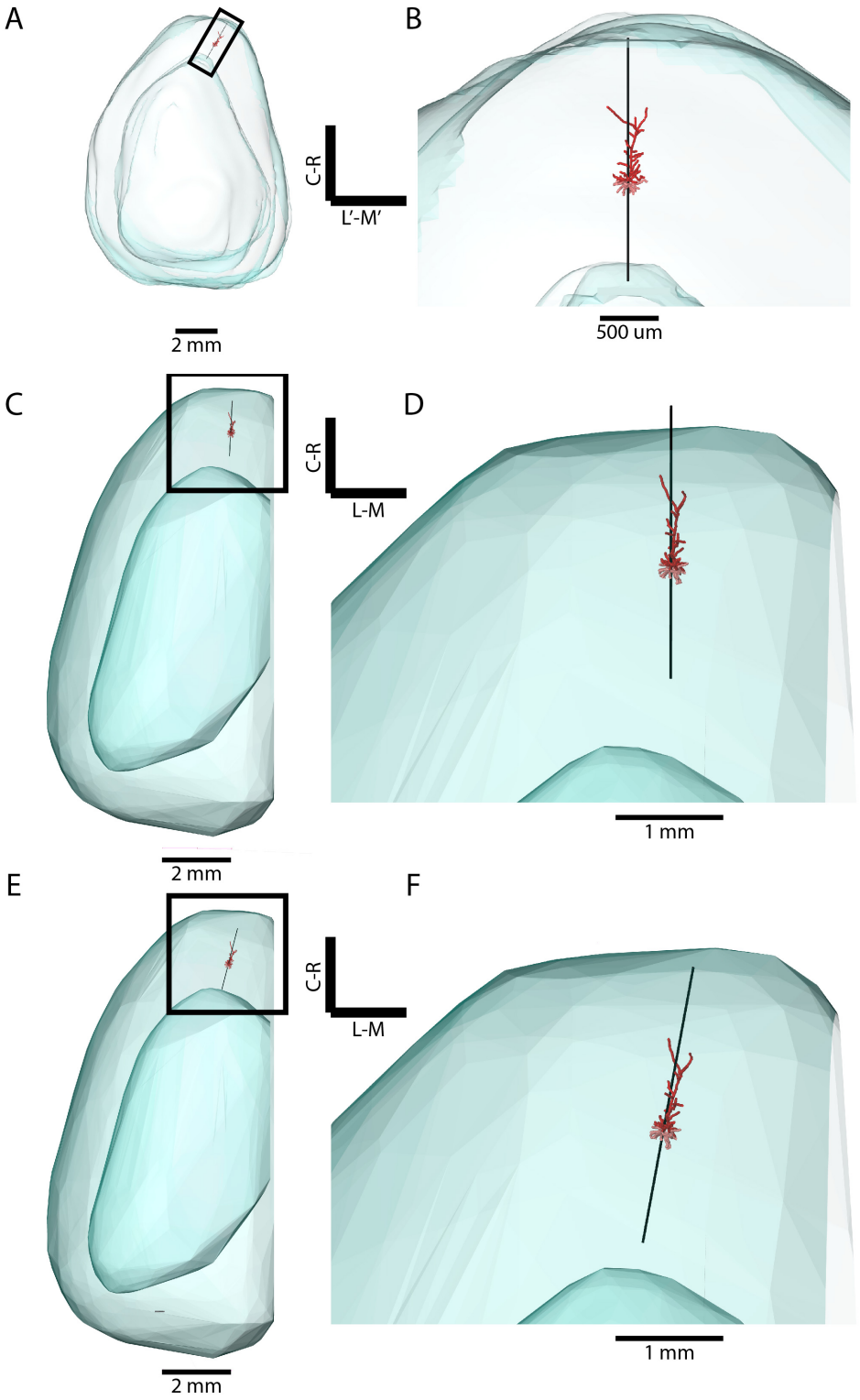

Figure 2.7. Registration of neuronal morphologies to the vM1 reference frame. A. Top view of a neuron morphology (to be registered) along with its axis. Pia and

Figure 2.7. WM surfaces of the tangentially sliced brain are visible as well. B. Zoom-in view of the morphology (from panel A). C. Registration step 1. Top view of the vM1 reference frame (LHS) with registered neuron (from panel A) after surface based alignment. D. Zoom-in view of the registered morphology. E. Registration step 2. Top view of the vM1 reference frame with the registered morphology after rotating the morphology to match the local orientation of the reference frame at the soma location and translating it along the registered neuron axis to preserve original soma depth. F. Zoom-in view of the registered neuron after orientation refinement. Note the change in orientation and soma depth compared to panel D.

soma location was estimated by finding the average orientation of all vectors of the axis field that are within a neighborhood of 800 µm radius. The method used for generating axis fields has been described in previous subsections. After rotating the neuron morphology, the registration process is completed by translating it along its registered axis (local average axis) in order to preserve its original soma depth from Pia.

The registration quality was evaluated by measuring the change in soma depth from Pia (or height from WM) along the neuron's axis as well as the change in neuron's orientation after registration. Orientation of the neuron was measured as the angle between the neuron's axis and the local orientation of the cortex at the soma location.

3 | Results

3.1 Putative synapses between *in vivo* labeled pairs of neurons

The method described in section 2.1.1 was applied to 5 animals, resulting in the reconstruction of 17 neuronal morphologies and one VPM axon. These morphologies yielded a total of 45 cell pairs across these 5 animals. All 45 cell pairs were then analyzed for putative synapses using the method described in section 2.1.2, which yielded a total of 216 touch points (overlap between spine and axon) out of which 49 were putative synapses (overlap between spine and bouton); which gave a conversion ratio of 22.7%. The average number of putative synapses per cell pair was 1.1 ± 1.5 and their distribution was as follows: 24 cell pairs (49%) made no putative synapses, 8 cell pairs (16%) made 1 putative synapse each, 6 cell pairs (12%) made 2 putative synapses each, 2 cell pairs (4%) made 3 putative synapses each, 3 cell pairs (6%) made 4 putative synapses each, 1 cell pair (2%) made 5 putative synapses and 1 cell pair (2%) made 6 putative synapses.

3.1.1 Number and distribution of cell type-specific putative synapses

Each neuronal morphology was classified into a cell type. There was 1 L3py neuron, 6 L4sp neurons, 3 L4ss neurons, 5 L5st neurons, 2 L5tt neurons and 1 VPM axon. The 45 cell pairs formed 20 cell type-specific pairs and their number as well as distribution is shown in Figure 3.1. Layer 4 neurons made the highest number of putative synapses with all other cell types (including itself), averaging 1.8 ± 1.7

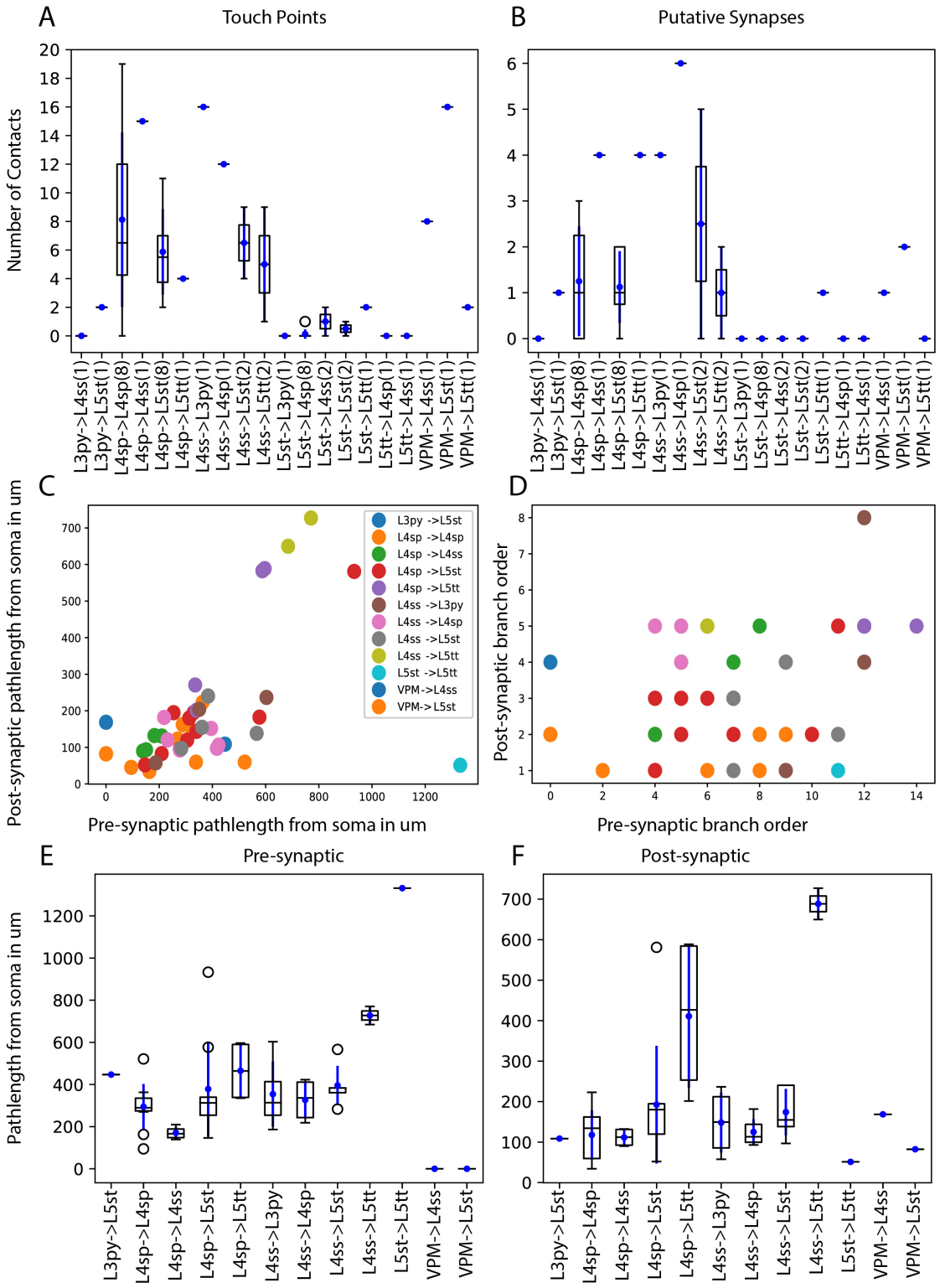

Figure 3.1. Number and distribution of cell type-specific putative synapses: A. Number of touch points organized by their pre and post synaptic cell types.

Figure 3.1. Distributions are shown as box plots (black) and error bars (blue). 18 neuronal morphologies reconstructed across 5 different animals make 45 cell pairs which form 20 cell types-specific pairs, yielding a total of 216 touch points. The number of times each cell type-specific pair is encountered in our data set (N) is shown in x-axis. B. Number of putative synapses organized by their pre and post synaptic cell types. Distribution of 49 putative synapses are shown as box plots (black) and error bars (blue). C. Scatter plot of pre and post synaptic path lengths from somata, colour coded by cell types. 12 out of 20 cell type-specific pairs have putative synapses. The path lengths are distributed in a concentrated manner. 90% of putative synapses have a presynaptic path length less than 600 µm and postsynaptic path length less than 300 µm . D. Scatter plot of pre and post synaptic branch order (edge level from somata), colour coded by cell types. E. Distribution of presynaptic path lengths from soma shown as box plots (black) and error bars (blue). Note that VPM path length is shown as zero, indicting that path length calculation was not possible as soma location is unknown. F. Distribution of postsynaptic path lengths from soma shown as box plots (black) and error bars (blue). Except for L5tt neuron, the postsynaptic path lengths are low, averaging about 141 µm.

(N=24), whereas layer 5 neurons made the least number of putative synapses, 0.1 ± 0.2 (N=16). Layer 3 and VPM made 0.5 ± 0.5 (N=2) and 1 ± 0.8 (N=3) respectively (see Figure 3.1B).

For each putative synapse its presynaptic path length from soma (on axon) and postsynaptic path length from soma (on dendrite) were calculated. Majority of the putative synapses (90%) had a presynaptic path length less than 600 µm and postsynaptic path length less than 300 µm (see Figure 3.1C). Furthermore, the pre and post synaptic branch orders (depth of branch from soma) were calculated for each putative synapse; 74% of them had presynaptic branch order between 4 and 9, whereas 98% of them had postsynaptic branch order between 1 and 5 (see Figure 3.1D). The presynaptic path lengths fell within a narrow range of 359 µm ± 176 µm (N=45) except for L5st neuron which had a presynaptic path length of 1332 µm (N=1) (see Figure 3.1E). Note that the presynaptic path length is shown as 0 for VPM axon, as its soma location is unknown and hence path length can not be calculated. Postsynaptic path lengths also had a narrow distribution of 141 µm ± 89 µm (N=43), except for Layer 4 neuron's connection to L5tt neurons which had a much higher postsynaptic path length of 503 µm ± 215 µm (N=6)

(see Figure 3.1F).

Out of the 49 putative synapses 16 had postsynaptic site on an apical dendrite (33%). 10 of these apical dendrite putative synapses were between Layer 4 and Layer 5. Rest were: 4 putative synapses between L4sp and L4sp, 1 between VPM axon and L5st and 1 between L3py and L5st. Out of the 10 putative synapses between Layer 4 and Layer 5, 4 were between L4sp and L5tt, 3 were between L4sp and L5st, 2 were between L4ss and L5tt and 1 was between L4ss and L5st.

3.1.2 Robustness of putative synapse detection method

The proximity radius, i.e., the maximum allowed distance between an axon and a dendrite for putative synapse detection, was determined through systematic testing. As shown in Figure 3.2A, increasing the proximity radius from 3 µm to 6 µm in steps of 1 µm, increased the number of proximity zones detected linearly from around 2000 to around 8000 in steps of approximately 2000. But such a linear relationship was not found between proximity radius and touch points (or putative synapses). There was a moderate increase in the number of touch points from 533 to 589 (90 to 108 for putative synapses) as the proximity radius increased from 3 µm to 4 µm. But after 4 µm, any increase in proximity radius did not produce new touch points or putative synapses, indicating that the additional proximity zones detected were false positives (see Figure 3.2B). Note that for this analysis touch points and putative synapses that a neuron makes with itself were also included.

In addition to the systematic testing, spine lengths were also calculated to ascertain the robustness of proximity radius. Spine lengths were determined by computing the euclidean distance between the center of spine head and the point on skeleton of dendritic shaft that is closest to it. Spine lengths were determined for all spines present in all proximity zones, yielding a total of 4838 spine lengths. Additionally, all 1674 spine lengths of a L5tt neuron were also determined, bringing the total number of spine lengths to 6512. A histogram of these spine lengths is plotted in Figure 3.2C. The average spine length was 1.9 µm ± 0.9 µm. 97% of spine lengths were less than 4 µm. Therefore, from the results of systematic testing and spine length analysis, the optimal proximity radius was set to be 4 µm.

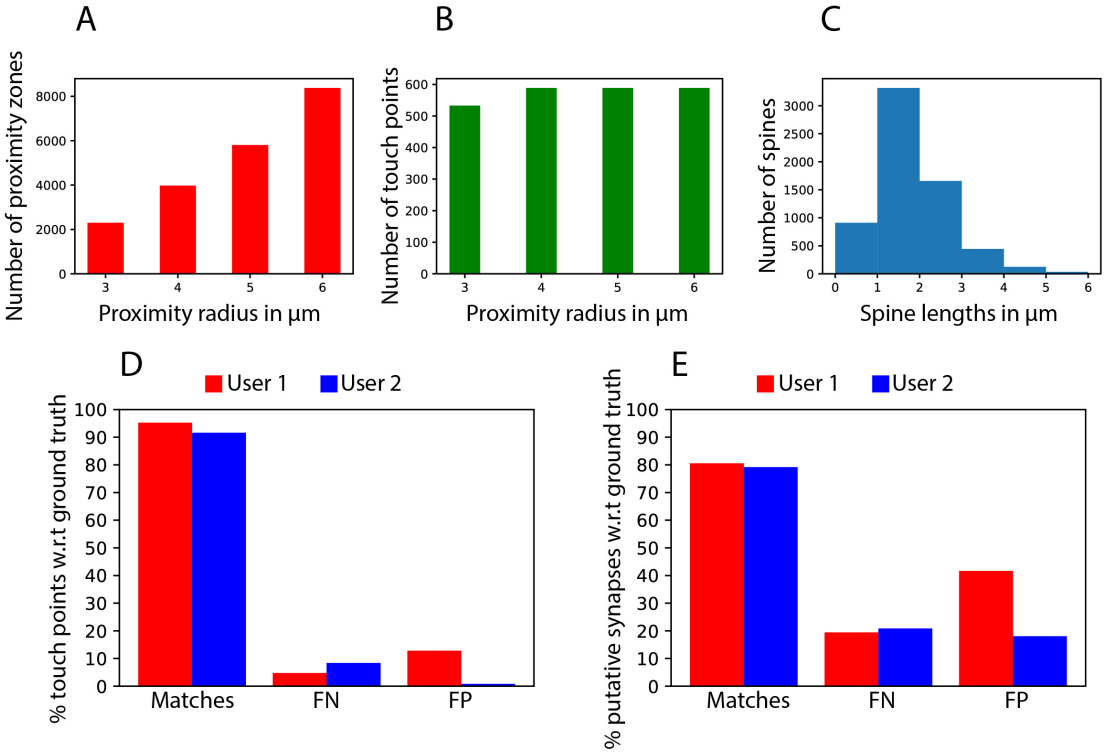

Figure 3.2. Robustness of the detection method: A. Number of proximity zones detected increases linearly with the increase in proximity radius. B. Number of touch points detected remain constant after 4 µm of proximity radius. C. Histogram of spine lengths. 97% of spines have a lengths less than 4 µm. Total number of spines analysed were 6512. D. Comparison of independent detection of touch points by 2 users with the consensus ground truth. Matches (accuracy), FN and FP for both users are shown (red and blue). E. Comparison of independent detection of putative synapses by 2 users with the consensus ground truth.

In order to determine the inter-user variability of the detection method, me and Dr. David Slabik went through all 3973 proximity zone image stacks detected with the proximity radius of 4 µm and independently marked the landmarks for touch points and putative synapses. After a few months, we created a consensus set with mutual agreement. This is treated as the ground truth (analysis shown in Figure 3.1 are based on this ground truth data set) and individual results are compared to this set. The comparison results for the 2 users are shown for touch points and putative synapses in Figure 3.2D and 3.2E respectively. For the comparisons an error resolution of 4 µm is used, i.e., if the distance between ground truth landmark

(touch point or putative synapse) and a user landmark is less than 4 µm, then it is considered a match at this error resolution. The landmarks that are in the user's set without any matching landmark in the ground truth set are called as false positives (FP); whereas the landmarks that are present in the ground truth set without any matching landmarks in the user's set are called as false negatives (FN). For touch points, User 1 has an accuracy (matches) of 95%, whereas FN and FP are 5% and 13% respectively. User 2 has an accuracy of 92%, whereas FN and FP are 8% and 1% respectively. In case of putative synapses, User 1 has an accuracy of 81%, whereas FN and FP are 19% and 41% respectively. User 2 has an accuracy of 79%, whereas FN and FP are 21% and 18% respectively (see Figure 3.2D,E). It can be seen that the accuracy and FN remain consistent between the 2 users, whereas FP varies more widely.

3.1.3 Comparison with the predictions of the statistical connectome model

Dr. Daniel Udvary, working with Dr. David Slabik compared the pair-wise putative synapses described above to the connection probabilities predicted by the statistical connectome of the SBF described in 1.2. A detailed description of the methods employed for the comparison as well as the results of the comparison are described in (Udvary, 2021). Briefly, all 45 *in vivo* labeled cell pairs and the putative synapses were registered to the dense structural model of the rat barrel cortex (SBF). Using equation 1.1, for each cell pair a and b, the predicted number of synapses between a and b, DSC(a,b), was computed as DSC(a,b,$\hat{x}$) summed over all 50 µm cubes $\hat{x}$. These model predicted number of synapses correlated with the observed putative synapses (n(a,b)) with a Pearson's correlation coefficient R of 0.75 (see Figure 3.3A).

In addition to the number of synapses, the likelihood of observing the putative synaptic pattern in those specific locations along the dendrite with a resolution of 50 µm ($S_{empirical}$) were also computed for 21 cell pairs (see Figure 3.3B). This was achieved by computing all possible combinations of 50 µm cubes in which the observed number of synapses could be located for each cell pair and finding the likelihood of each such combination (using equations 1.2 and 1.3). Only 17%±21%

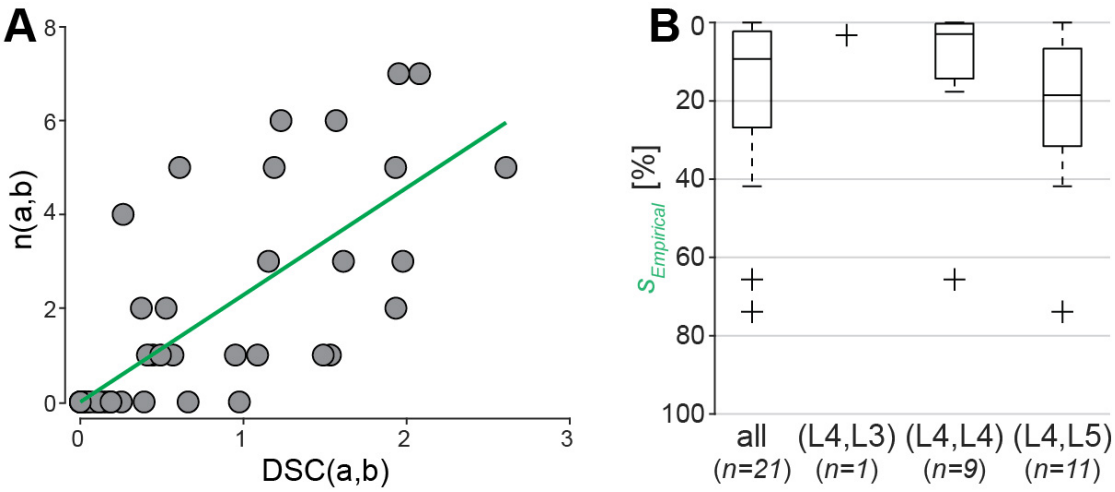

Figure 3.3. Comparison with the predictions of the statistical connectome model. A. The number of synapses predicted by the statistical connectome of the SBF for 45 cell pairs, correlate well (R=0.75) with the observed number of putative synapses between *in vivo* labeled pairs of neurons. B. Likelihood of finding a more likely synaptic pattern than the observed putative synaptic pattern. Out of all possible combinations (patterns) of 50 µm cubes in which the observed number of synapses could occur, only 17%±21% patterns were found be more likely than the observed synaptic pattern. Likelihoods displayed for connectivity between L4–>L3, L4–>L4, L4–>L5 and all 3 cell type pairs. This figure and data have been adopted from (Udvary, 2021)

of such combinations were more likely to occur than the observed putative synaptic pattern. In other words, the observed (empirical) synaptic pattern was on average the 18^{th} most likely pattern out of 100 as per the model (0 being the most likely pattern). In summary, the number and pattern of putative synapses were in line with the predictions of the dense statistical connectome model of the SBF.

3.2 The facial nucleus reference frame and its applications

In this section, I reproduce the results presented in (Guest et al., 2017). Specifically, I present the variability and precision of the rat FN geometry with the help of its local reference frame. I also delineate the cellular organization of the rat

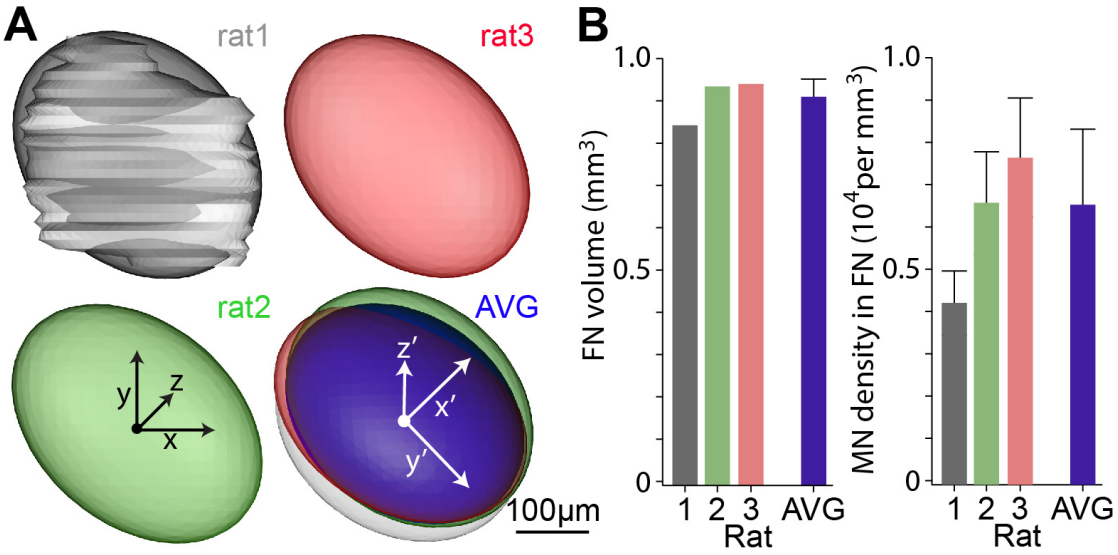

Figure 3.4. Geometry and cellular organization of the rat FN. A. Ellipsoid approximation of the FN volumes. Three FN volumes were approximated by ellipsoids and their average was derived (blue), which represents the 3D FN reference frame. The x, y and z directions are along L-M, C-R and V-D axes respectively. x', y' and z' represent the axes of FN reference frame coordinate system. B. Left panel: Variability of the FN ellipsoid volumes were small (CV of 5.5%) and the average FN volume was 0.91 mm^3 ± 0.05 mm^3. Right panel: MN density in FN was 6743 ± 1584 per mm^3 and the number of MNs in FN was 6136 ± 1020. This figure is adopted from (Guest et al., 2017).

FN, particularly organization of the vMNs (along with its dendrites) within the FN. Finally, I quantify and visualize the trans-synaptic tracing of whisker muscle related neuronal networks using the replication competent rabies virus within the brain stem.

3.2.1 Geometry and cellular organization of the rat FN

Variability and precision of the rat FN geometry The experimental procedure explained in 2.2.1 was applied to three rats. Following the histology and imaging, the FN contours as well as NeuN soma locations were obtained for all three rats as explained in 2.2.2. These FN contours were then approximated by ellipsoids and the average of these ellipsoids (i.e., FN reference frame) was generated using the method described in 2.2.3. The three FN ellipsoids and their

average are shown in Figure 3.4A. The variability of volume as well as the extent and orientation of PAs of the FN ellipsoid were as follows. The volumes of the FN ellipsoids were very similar across three rats, 0.91 mm^3 ± 0.05 mm^3 (mean ± SD), having a coefficient of variation (CV) of 5.5% (see Figure 3.4B). The difference in volume between the ellipsoid approximation and the FN volume was 16% ± 3%. The extents of the three PAs were also similar across the three animals, having CVs of 1.2%, 2.3% and 6.7% respectively. The longest PA had an extent of 1.6 mm ± 0.02 mm and was most parallel to the C-R axis (y-axis). The second largest PA had an extent of 1.3 mm ± 0.03 mm and was most parallel to the L-M axis (x-axis). The third PA had an extent of 0.9 mm ± 0.06 mm and was most parallel to the V-D axis (z-axis). Since the variability of FN volume and extent were very small (as evidenced by small CVs) an average ellipsoid was generated, such that the extent of PAs of this ellipsoid are the mean of the extent of individual FN ellipsoids. This average ellipsoid represents the standard FN reference frame, with its center being the origin and its PAs being the three axes of the coordinate system x', y' and z' (see Figure 3.4A). In order to find out how precisely we can register new FN onto the standard reference frame, the three individual FN ellipsoids were aligned to the standard by minimizing the squared error between surfaces. The SD of the means (centroids) of these aligned ellipsoids, in other words, the mean of euclidean distances between aligned individual ellipsoid centroids and the center of the reference ellipsoid was 120 µm. This is the precision with which we can register facial nuclei to the FN reference frame. Similarly, the angular precision, which is the mean of angles between the PAs of aligned ellipsoids with the respective PA of the standard ellipsoid, was 4.6° ± 2.0° (averaged across the three PAs).

Cellular organization of the rat FN As mentioned in the methods section 2.2.2, the FN was identified using the size differential between the somata of neurons that are inside the FN against those that are outside. The diameter of MNs inside the FN were almost twice as large, 30 µm ± 4 µm, compared to the diameter of somata that are at the border of (and surrounding) the FN, which were 16 µm ± 5 µm (see Figure 2.3C)). All NeuN positive somata were identified in 2D images of each section. In order to obtain an estimate of number of neurons inside the FN, cell counting was performed on 3D image sub-volumes and the scaling factor

(from 2D to 3D) was determined to be 2.1 ± 0.4. Scaling up the cell counts using this scaling factor, the number of neurons inside FN were determined to be 6136 ± 1020 across the three animals. Therefore, the neuronal density of FN was 6743 ± 1584 per mm^3 (see Figure 3.4B). The 3D distribution of somata showed a region of lower density between the lateral and medial parts (see Figure 2.3E).

3.2.2 Organization of vMNs within the rat FN

In this subsection, I describe the organization of vMNs within the rat FN, delineated by retrograde mono-synaptic tracer injections into the intrinsic whisker muscles. First, the successful targeting of individual intrinsic whisker muscle and the subsequent labeling of targeted whisker specific MNs in the FN is verified. Second, the whisker row-specific organization of vMNs within rat FN is depicted. Third, retrogradely labeled vMNs of multiple animals were registered into the FN reference frame, resulting in the generation of standardized whisker row-specific vMN slabs.

Targeting an individual intrinsic whisker muscle Using the method described in 2.2.1, a mono-synaptic retrograde tracer - Cholera Toxin Beta subunit (CTB) - was injected into the chosen whisker pad, targeting the intrinsic muscle. The CTB was conjugated with different florescent dyes: Alexa Flour 488, 594 and 647; so that multiple whiskers can be targeted within the same animal in order to verify whisker specific labeling of motoneurons inside the FN. A schematic of this procedure can be seen in Figure 3.5A. Using this method, whiskers in the same arc (B2/C2/D2) were targeted in 3 rats, whereas in 3 other rats whiskers belonging to the same row (C1/C2/C3) were targeted. After injecting, the whisker pads were removed (see Figure 3.5B), sliced into 150 µm thick sections and imaged so as to inspect the exact location and spread of the injection sights. It was found that the center of injections were 910 ± 285 µm below the surface of the whisker pads and 609 ± 415 µm posterior to the base of the follicle. The diameter of injection sites were 910 ± 285 µm and overlapped with the target intrinsic muscle. The separation between follicles of the same row were 789 ± 108 µm and were more than twice the average injection diameter, whereas the separation across follicles

of different rows were still larger at 1114 ± 173 µm. It was seen that the CTB infected only the intrinsic muscle (with the injection sites resembling the sling of the infected intrinsic muscle) and did not infect the sensory pathway (follicle) or the tissue between the muscles (see Figure 3.5C,D).

Whisker-specific labeling of vMNs in the FN Having verified that the CTB injections infected the targeted intrinsic whisker muscle, neurons that were retrogradely labeled by these CTB injections in the FN were analyzed. From the 18 CTB injections carried out across 6 animals, 42 ± 32 neurons were labeled and they all were located in the ventrolateral part of the FN (see Figure 3.5E,F), which further confirms that only intrinsic muscles were infected by CTB and not the extrinsic muscles (Klein & Rhoades, 1985). Most of these CTB labeled neurons were positive for a single marker. Dual labeling was only observed for adjacent whiskers. About 4% vMNs that belonged to adjacent whiskers of the same row were doubly labeled, whereas only 1% of vMNs belonging to the adjacent whiskers of the same arc were doubly labeled (owing to the increased separation between the follicles of different rows as opposed to the follicles of the same row).

Whisker row-specific organization of the vMNs Having confirmed the whisker specific labeling of vMNs in rat FN, the CTB experiments were carried out for an additional 36 whiskers across 13 rats. The target whiskers chosen in each animal were separated by at least one whisker, in order to avoid double labeling. The whiskers targeted were: C1/C3/C5 (N=3), A3/C3/E3 (N=3), A1/C3 (N=3), C2/C4/E1 (N=2), B3/D3/β or δ (N=2). These chosen whiskers cover different combinations: belonging to the same row, belonging to the same arc, along a diagonal axis and belonging to different rows and arcs respectively. Each CTB injected into a whisker labeled a distinct set of vMNs in the rat FN, without any overlap (double labeling). For each animal the labeled vMNs were identified for each CTB injection and visualized within their FN ellipsoids (see Figure 3.6A). The number of vMNs labeled per whisker was 46 ± 5 (mean ± SEM) across all 36 whiskers and did not show any significant correlation along whisker row (Pearson R = 0.17) or arc (R = 0.07). A convex hull was generated around the vMNs labeled by each whisker. These hulls were elongated and were therefore approx-

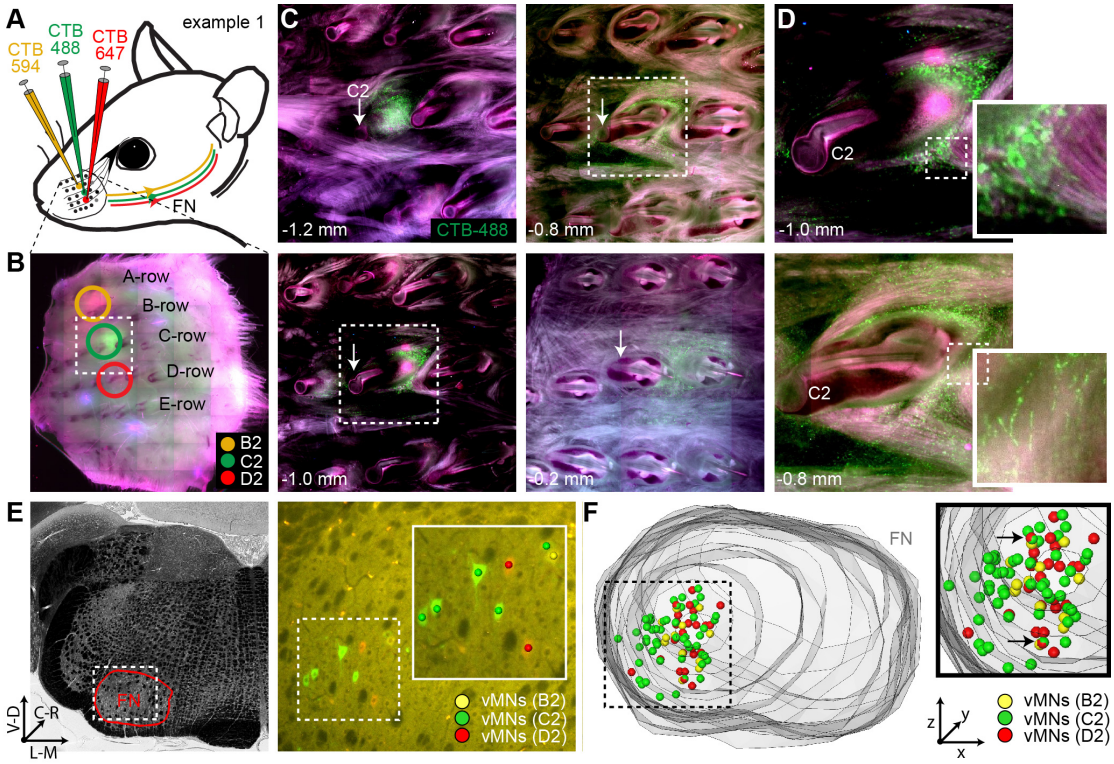

Figure 3.5. Targeting and labeling the whisker-specific vMNs in the rat FN. A. Schematic of an example experiment where three adjacent whiskers belonging to the same arc (B2/C2/D2) were targeted by three versions of retrograde CTB tracers (conjugated with AlexaFlour 488, 594 and 647) respectively. B. Image of injection sites for the example experiment shown in panel A. C. Cross sections of the injected C2 whisker pad (shown in panel B) at four different depths. The whisker pad was sliced into 150 µm thick sections and inspected for spread of the injection. At the depth of 1.2 mm below the surface of the whisker pad (top left), we see the injection site which is posterior to the target whisker follicle (indicated by the white arrow). Sections at 1.0 mm and 0.8 mm depths show that the injection did not spread into the intrinsic muscles of adjacent whiskers. There was no infection of extrinsic muscle as evidenced by the lack of infection seen at the depth of 0.2 mm. D. Zoomed-in images of the C2 whisker pad at depths of 1.0 mm and 0.8 mm, confirming the spread of the injected tracer within the intrinsic muscle (evidenced by the formation of sling shape). E. 50 µm thick coronal section of right hemisphere of brain stem (shown reflected around the mid line plane). FN contours are drawn in each of these FN containing sections. Right panel shows the zoomed-in FN, where distinct vMNs are labeled by each retrograde injection. F. 3D FN generated from the section-wise FN contours, showing the vMNs labeled in the ventrolateral part of the FN. The labeling was largely whisker-specific (with each whisker injection labeling primarily non-overlapping set of vMNs) with occasional

Figure 3.5. overlap seen between C2 and D2 whisker injections, as showcased by the black arrows in the zoomed-in panel to the right. This figure is adopted from (Guest et al., 2017).

imated by an ellipsoid, similar to the FN approximation. The volumes of these whisker specific vMN slabs were 0.065 ± 0.007 mm^3 (mean ± SEM) and showed no correlation along rows (R=0.12) or arcs (R=0.20). The number and volumes of whisker specific vMNs are shown in Figure 3.6B. These slabs had their longest axis being almost parallel to the C-R axis (y'). The slabs belonging to different rows (e.g., A3/C3/E3), although overlapping, were separable along the axis most parallel to L-M axis (x'); whereas the slabs belonging to the whiskers of the same row (e.g., C1/C3/C5) occupied more or less the same volume (see Figure 3.6C). This row-specific organization of vMNs was further quantified by plotting the center locations of vMN slabs in the FN reference frame coordinate system (see Figure 3.6D). In each experiment where injections were separated by one row (n = 13), the slab representing the lower whisker row (on the snout) is located more medial within the FN. Contrastingly, the experiments where whiskers belonging to the same row were targeted (n = 10), slabs showed no systematic shift with respect to each other. As we move from row A to E, the center of the slab shifts systematically along the L-M axis (see Figure 3.6E). No such organization is visible along the arcs.

Standardized row-specific slabs of the vMNs in the FN reference frame
All vMNs labeled by the 36 injections along with their slab ellipsoids were registered into the standard FN reference frame using affine transformation as described in the method section 2.2.3. A step by step visualization of these registrations can be seen in Figure 3.7A-C. In order to uncover the organizational patter of these vMN slabs, the position of the center - and the 3D orientation of the PAs - of each vMN slab ellipsoid was analyzed (see Figure 3.7D). The three PAs have slab extents of 1121 ± 29 µm, 444 ± 26 µm and 328 ± 20 µm (mean ± SEM) respectively; having no significant correlation with the position of injected whisker's row or arc. Similarly, the orientation of PAs were 24 ± 2 °, 39 ± 4 ° and 27 ± 3 ° (mean ± SEM) with respect to the L-M, C-R and V-D axes respectively and

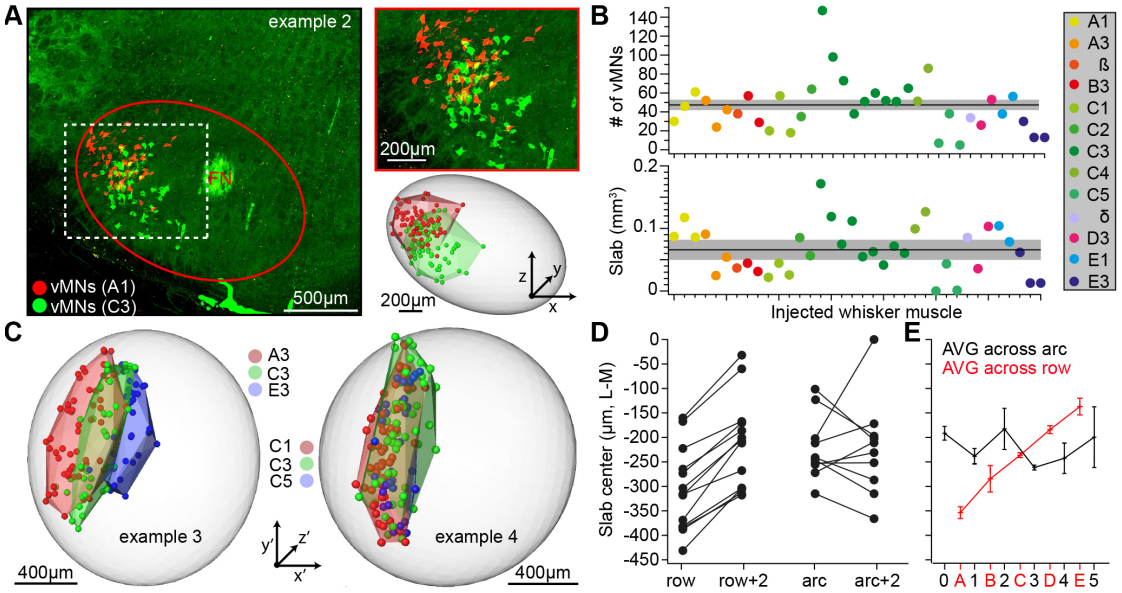

Figure 3.6. Whisker row-specific organization of the vMNs within the rat FN. A. Visualization of vMNs labeled by CTB whisker injections. Left panel: Maximum projection image of confocal image stack spanning the FN of an experiment where the intrinsic muscles of A1 and C3 whiskers were injected with two different versions of CTB. The respective whisker specific vMN populations labeled by these two injections (shown in red and green colors respectively) occupy the ventrolateral part of the FN and span the entire FN along the C-R axis. Right panel: Top panel shows the zoom-in of vMNs from the left panel. We can see that the two whisker injections label two distinct sets of vMN populations. Bottom panel shows the center locations of the two vMN populations (red and green) as well as the volumes occupied by them in the form of convex hulls. The location of these shell-shaped slabs are visualized within the FN ellipsoid. B. The experiment mentioned in panel A, was repeated for 12 more rats yielding a total of 36 injections targeting whiskers belonging to different rows and arcs. The distribution of number of vMNs labeled per whisker injection is shown in the top panel. The mean ± SEM of the number of vMNs per whisker was 46 ± 5, which is shown as a black line and grey shaded area. The distribution (as well as mean ± SEM) of the volume of whisker specific slabs is shown in the bottom panel. C. Visualization of vMN distributions of two more examples experiments. In the left panel whiskers belonging to the same arc but different rows were targeted (A3,C3 and E3); whereas in the right panel whiskers belonging to the same row but different arcs were targeted (C1,C3,C5). The vMN slabs representing the whiskers belonging to the same row occupy the same volume (right panel); whereas slabs belonging to different rows are disjoint (left panel). This indicates the whisker row-specific organization of the vMNs within the rat FN. D. Quantification of whisker row-specific organization of

Figure 3.6. the vMNs. When the center location of each vMN slab (across all 36 whisker injections) are plotted along the L-M axis, it became apparent that there is a systematic shift between slabs representing different rows. No such pattern is seen for slabs representing the different arcs (but belonging to the same row). E. Mean ± SEM of vMN slab centers along the L-M axis, belonging to each row and arc. The row-specific organization of vMNs is evident due to the systematic shift across rows but not across arcs. This figure is adopted from (Guest et al., 2017).

showed no significant correlation with the position of whisker's row or arc. The centers of the slabs showed significant correlation along the L-M (R=0.6) and V-D (R=-0.4) directions. Which means that, as we go through the whiskers sorted by row A to E (and then by arc 1 to 5 (A1 to E3)), whisker row-specific slab centers move from lateral to medial in steps of 54 µm and from ventral to dorsal in steps of 19 µm. Therefore, to represent the row-specific map of vMNs within the standard FN reference frame, five slabs (one for each row) of equal extents and orientation were generated and placed at their respective average position within the FN reference frame. The C3 slab centers varied by 144 µm across animals (N=9), which is similar to the precision of the FN reference frame. These standardized row slabs and their map within the FN reference frame are shown in Figure 3.7E. In order to generate the standardized row slab, the registered vMN somata of C-row across experiments were converted into a density map using a resolution of 100 μm^3 and then an iso-surface was generated using a density cutoff threshold of 90% around this volume.

3.2.3 Trans-synaptic rabies virus tracing of the whisker muscle-related neuronal networks

Having verified the successful targeting of the individual intrinsic whisker muscle and the subsequent whisker-specific labeling of the vMNs in the FN in the previous subsection, I now present a novel method of defining brain regions based on their synaptic distance from a terminal muscle. In order to do this, we inject replication-competent trans-synaptic retrograde rabies virus (N2c strain) into the intrinsic muscle of C3 whisker (similar to the CTB injections described in the previous subsection) and follow its propagation across synapses. In this subsection, I first

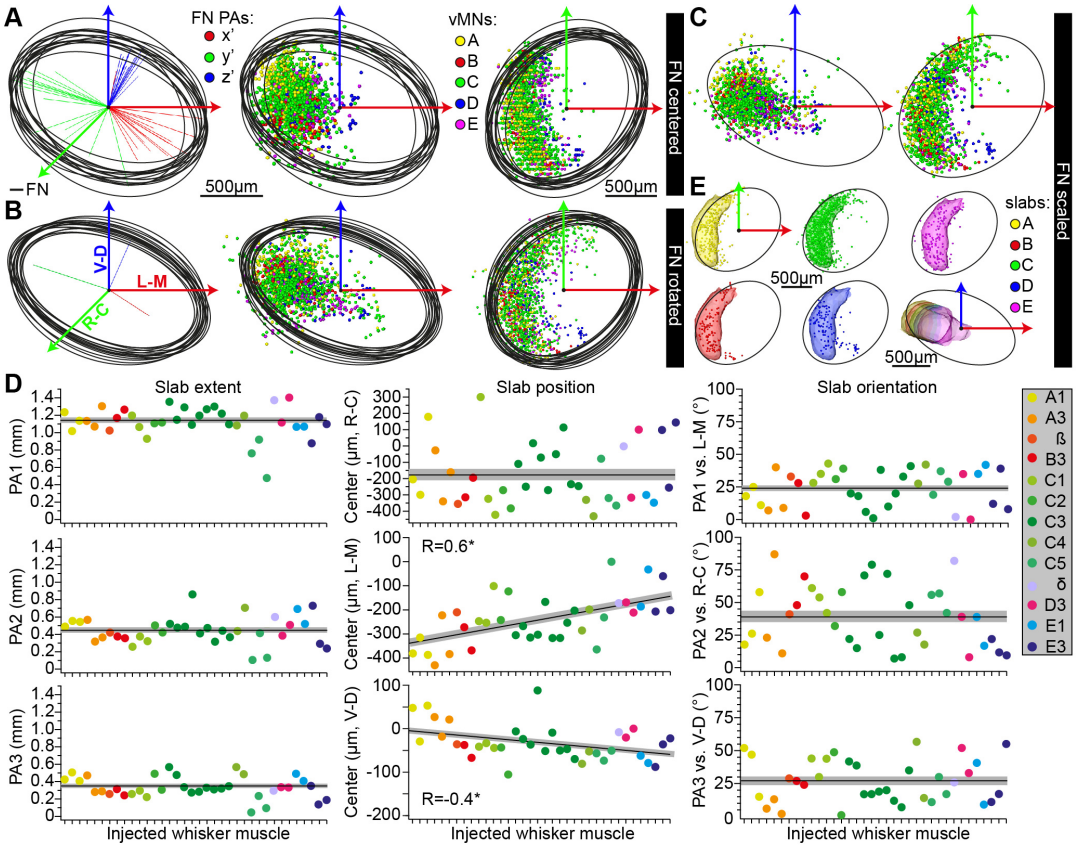

Figure 3.7. Standardized row-specific slabs of the vMNs within the rat FN reference frame. A–C. Registration of vMN somata from 13 CTB whisker injection experiments into the standard reference frame of the rat FN. A. In each CTB whisker injection experiment the FN is approximated by an ellipsoid and translated to match the center of the FN reference frame. Left panel: Coronal view of all centered FN ellipsoids with the color coded principal axes (x', y', z'). Mid panel: Labeled vMN soma centers from each experiment centered to the FN reference frame using the respective FN ellipsoid's translation. The vMN somata are color coded according to their whisker row. Right panel: Same as mid panel but in axial orientation. B. Each centered FN ellipsoid is rotated to align its principal axes with the respective principal axes of the FN reference frame (left panel). The resulting transformation is applied to the vMN somata of respective individual experiments. Mid and right panels shown coronal and axial views respectively. C. Principal axes of each aligned FN ellipsoid are linearly scaled to match the scale of the principal axes of the FN reference frame and the resulting transformation is applied to the vMN somata accordingly. Right and left panels show the registered vMNs from all experiments in coronal and axial orientations respectively. D. Row specific organization of the vMN slabs. Whisker-specific vMNs labeled using 36 CBT whisker injections (resulting from 13 animals) were registered to the standard

Figure 3.7. FN reference frame. Each set of whisker-specific vMNs was approximated by an ellipsoid slab to obtain its extent, position and orientation. These parameters are plotted after sorting the slabs first by the whisker row and then by the arc. Slab's extent along the three principal axes show no correlation w.r.t. whisker row or arc (see left panel). Slab's orientation w.r.t. the principal axes also show no correlation (see right panel). Slab centers (see mid panel) show correlation along the L-M and V-D axes but not along C-R axis. The correlation is seen along the whisker rows but not along the arcs. E. Visualization of the standardized vMN slabs. Standard whisker-row specific slabs have the extent and orientation of the C-row slab. They are positioned within the FN reference frame as per the average position of respective row-specific slabs. This figure is adopted from (Guest et al., 2017).

describe the trans-synaptic rabies virus and the criteria for defining orders of trans-synaptic labeling. Then, I explore the neurons and brain regions labeled by the rabies virus across different synaptic orders.

Rabies virus as the trans-synaptic retrograde tracer Replication-competent strains of the rabies virus have been previously applied for tracing motor networks involved in the control of specific single muscles (Kelly & Strick, 2000; Ugolini, 2010). These strains have the following desirable properties. First, their entry into the central nervous system is exclusively through the motor route and thus can be accomplished via intramuscular injection (Tang, Rampin, Giuliano, & Ugolini, 1999; Ugolini, 2008). Second, the intracellular transport of the rabies virus is restricted to the soma and the dendrites after replication and hence the trans-synaptic transfer of the virus occurs exclusively in the retrograde direction (Ugolini, 1995; Klingen, Conzelmann, & Finke, 2008). Third, the trans-synaptic transfer happens in a time-dependent manner, taking about 8-12 hours per synaptic transfer (Ugolini, 1995; Tang et al., 1999; Kelly & Strick, 2003), thus allowing the precise identification of trans-synaptic order of rabies labeled neuronal populations by varying the survival time of the infected animal (and thereby controlling the time taken for trans-synaptic transfer of rabies virus). Furthermore, the trans-synaptic spread is not dependent on the location of synapses along the dendrites or axons between pre and post synaptic neurons (Ugolini, 2010); thus all neuronal

populations of the same synaptic order are labeled synchronously.

Definition of trans-synaptic orders of spread Due to the properties of the rabies virus described above, we can inject this virus into the intrinsic whisker muscles in order to distinguish animals having different trans-synaptic order of spread, i.e., animals that have successive neuronal populations labeled based on their respective synaptic distance from the terminal muscle. This can be accomplished by controlling the trans-synaptic spread of the virus, via controlling the time between injection and perfusion (survival time). Although, the spread occurs in a time dependent manner, the time taken for the initial uptake of the virus varies across animals. Therefore, we determine the synaptic order of spread by quantifying the brain-wide distribution of rabies positive neurons in addition to the survival time of each experiment (see 3.8A). As demonstrated in the previous subsection, the vMNs innervate the intrinsic muscle (and hence are pre-synaptic to it) and are the first-order neurons. The second-order neurons that innervate these vMNs are located in the brain stem (Hattox, Priest, & Keller, 2002; Takatoh et al., 2013). Layer 5 pyramidal tract neurons of the cortex directly innervate these second-order brain stem neurons (Sreenivasan, Karmakar, Rijli, & Petersen, 2015) and therefore are defined here as third-order neurons. Any experiment where the cortical labeling is beyond L5 are deemed to represent fourth-order (or higher) trans-synaptic spread.

First-order neurons The N2c strain of the rabies virus was injected into the intrinsic muscle of C3 whisker and the rats were sacrificed after 3 days (72 hours) at an interval of 12 hours. Brains went through sectioning, histology and imaging as described in the methods section (see 2.2.1). Rabies as well as NeuN distributions were obtained and brain regions (including the FN) were contoured (see section 2.2.2 and Figure 3.8B). In two littermates, which were sacrificed after 72 and 96 hours respectively, the rabies labeling was restricted to the brain stem (no labeling in the cortex) and thus these animals were exhibiting second-order trans-synaptic spread as per our definition (see Figure 3.8C first column). Only a handful of vMNs in the FN were labeled by the rabies virus in these two animals (6 and 3 respectively). This sparseness indicates that there is little to no replication of the

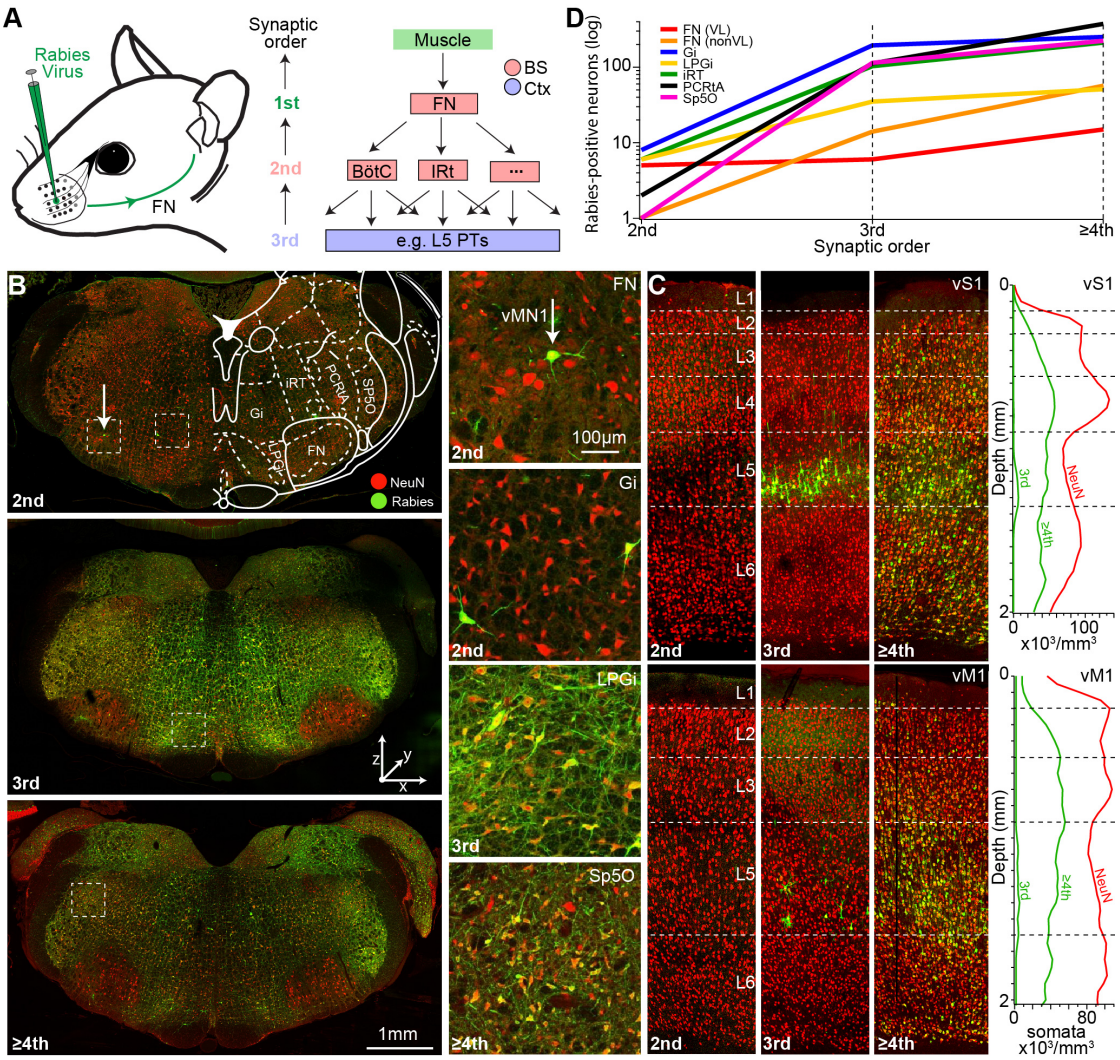

Figure 3.8. Trans-synaptic tracing of the whisker muscle-related neuronal networks. A. Schematic illustration of the rabies virus injection and its trans-synaptic tracing. Left panel: Schematic of the rabies virus being injected into the intrinsic muscle of the C3 whisker. Right panel: Illustration of definition of trans-synaptic order of labeling. First order experiments are ones where rabies labeling is restricted to the vMNs of the FN. In the second order animals, labeling is restricted to the BS nuclei which are presynaptic to the vMNs of the FN. In the third order animals, rabies labeling has spread to the cortex but restricted to Layer 5. Greater than third order experiments are ones where rabies labeling has spread to other layers of the cortex. B. Trans-synaptic labeling of the BS across different orders of spread. Left panel: Maximum projection images of certain BS sections containing the FN, arranged in the increasing order of rabies spread (from top to bottom). Right panel: Higher magnification image crops of example rabies labeled BS nuclei showing: second order (FN and Gi), third order (LPGi) and fourth order (Sp5O)

Figure 3.8. labeling. C. Trans-synaptic labeling of cortex for different orders of rabies spread. Left panel: Example cortical image snippets showing no labeling, Layer 5 only labeling and labeling across cortical layers for second, third and fourth order (or higher) synaptic spread respectively in vS1 (top) and vM1 (bottom) regions. Right panel: cortical depth profile of rabies and NeuN densities for third and fourth (or higher) order rabies spread in vS1 and vM1 regions. Rabies profiles represent the average of three coronal sections through vS1 and vM1 respectively, wherein the quantification of rabies-positive neurons was performed manually. D. Quantification of all rabies-positive neurons in the BS. Ventro-lateral FN shows no significant increase in the number of rabies-positive neurons across synaptic orders of spread. All other BS nuclei show one order of magnitude (or higher) increase in the number of rabies-positive neurons while going from second to third order, whereas the increase is 2-4 fold while going from third to fourth order of synaptic spread. This figure is adopted from (Guest et al., 2017).

virus in the muscle (Ugolini, 2010) or the fibers of the passage (Tang et al., 1999; Levinthal & Strick, 2012) (see Figure 3.8D).

Dendritic organization of the vMNs in the rat FN The sparse labeling of the vMNs in the FN as well as the quality of rabies labeling and subsequent high resolution imaging allowed for the reconstruction of 3D morphologies of the vMNs (see Figure 3.9A). Soma, dendrite and local axon morphologies of 3 out of 6 vMNs labeled in an animal were reconstructed using the methods described in 2.2.2. The 3 reconstructed vMN morphologies are shown in 3.9B. The dendritic path lengths were 11.4 $\pm$ 3.7 mm (mean $\pm$ SD) across the 3 dendrites. Number of dendrites extending radially (within the coronal plane) from the soma were 6 $\pm$ 2. Most of these dendrites terminated outside the FN contours with sparsely branched arbors. The somata and morphologies of these vMNs were then registered to the standard FN reference frame. After registration, all landmarks were located within the standardized C-row slab, further verifying the precision of FN reference frame and the registration process (see Figure 3.9C). The somata of these registered dendrites were located more rostrally and projected their dendrites towards and beyond the rostral most part of the FN; they innervated a region more medial than the slabs. The dendritic fields were quite disjoint in the sagittal plane and innervate different depths along the C-R axis. The degree to which these dendrites

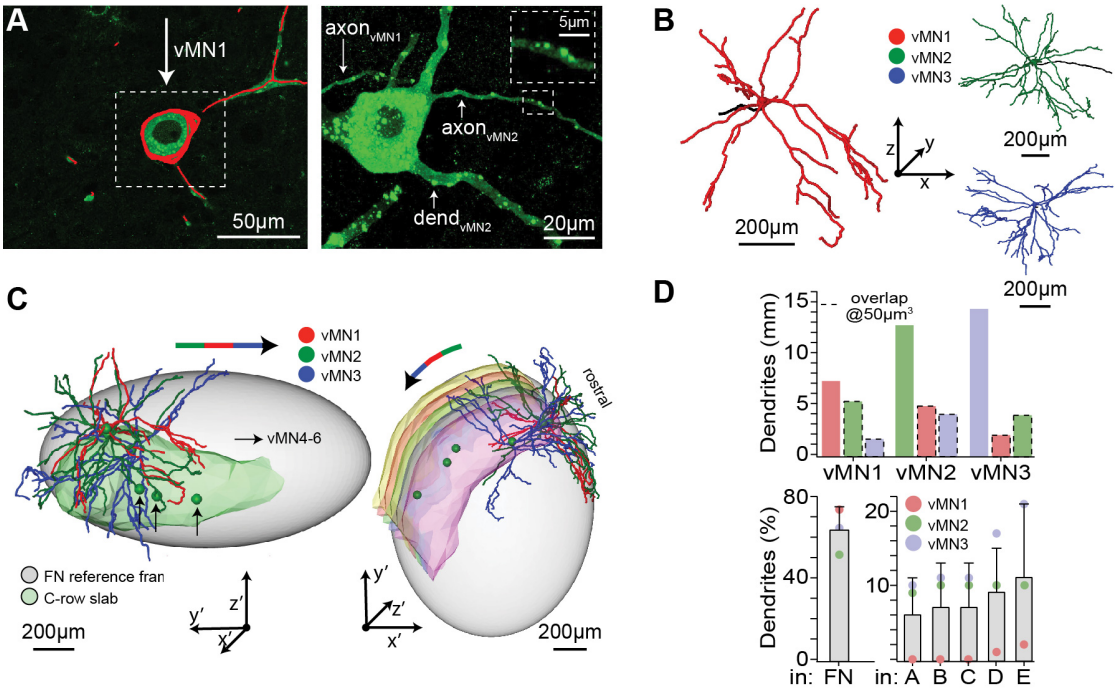

Figure 3.9. Dendritic organization of the vMNs. A. Visualization of rabies labeled dendrites. Left panel: High resolution image of rabies labeled vMN1 shown in Figure 3.8B (top right panel). Right panel: High resolution image of a histological section that was adjacent to the one shown in the left panel. In this image we can see axon and dendrites of the second neuron (vMN2) as well as axon of vMN1. B. 3D morphologies of three reconstructed dendrites from the same animal including those of vMN1 and vMN2. C. Registration of those three morphologies onto the FN reference frame. The vMNs are registered to their home whisker row (C-row). D. Variability of vMN dendrites within the FN. Upper panel: Dendrites partially overlap with each other. Lower panel: dendrites partially extend beyond the FN. Overlap of dendrites with row-specific slabs varies significantly across vMNs. This figure is adopted from (Guest et al., 2017).

overlapped amongst each other varied widely (see Figure 3.9D top). The overlaps, computed at the resolution of 50 µm^3, ranged between 13% to 72% with an average overlap of 34%. Across the 3 vMNs 64% ± 10% of the dendrites were inside the FN and these dendrites overlapped with row-specific slabs very sparsely, with one vMN having about 10% overlap with each slab, the other having almost no overlap with any slab, and the third one having 17% and 21% overlap with D and E slabs respectively (see Figure 3.9D bottom).

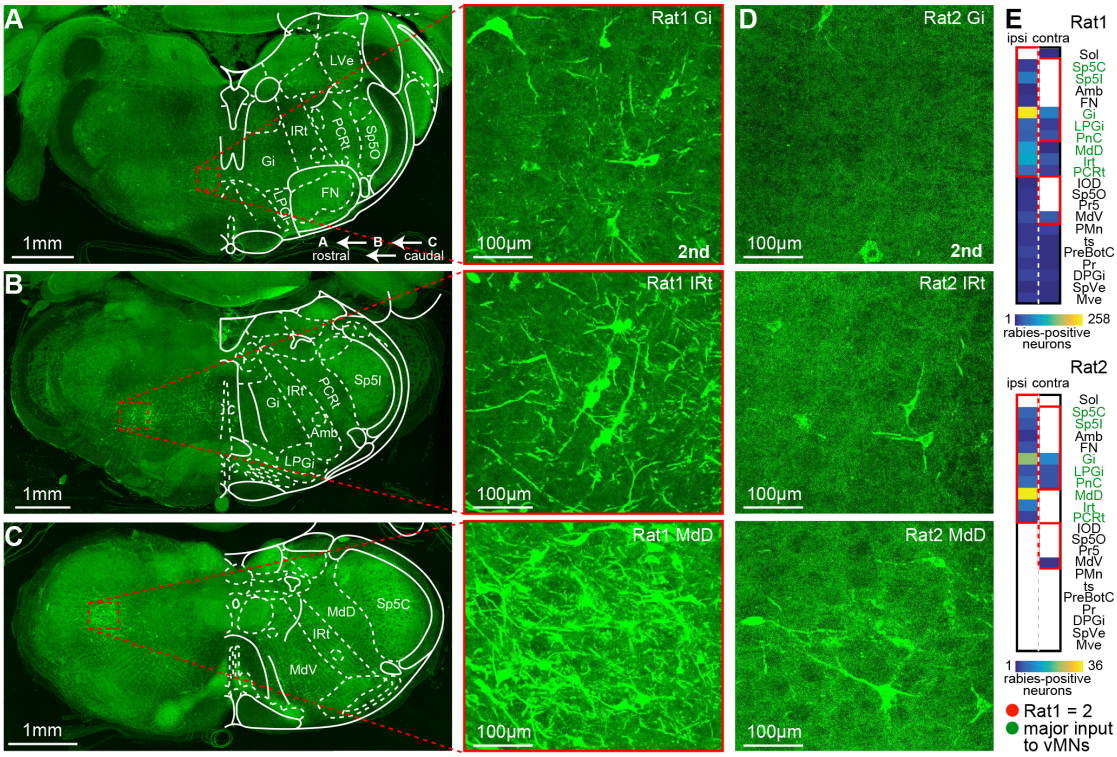

Figure 3.10. Pre-synaptic populations of the vMNs. A. Left panel: Maximum projection image of all brain sections comprising the Sp5O of the BS of a second order animal (Rat 1). The corresponding map of the rat brain from the Paxinos atlas is superimposed on the right. Right panel: Zoom-in showing sparse rabies labeling of second order neurons that are pre-synaptic to the FN in the Gi. B. Same as panel A, but the maximum projection image in the left panel spans all BS sections containing the Sp5I. The right panel shows labeling in the IRt. C. Same as panels A and B, but the left panel is a maximum projection image of all BS sections spanning the Sp5C, whereas the right panel shows rabies labeled second-order neurons in the MdD. D. Same as panels A through C, but for a second second-order animal (Rat 2). This animal shows significantly sparser labeling in the BS nuclei. E. Comparison of the rabies labeled BS nuclei in two second-order experiments (Rat 1 vs Rat 2). Although the number of nuclei and the number of neurons labeled in each nuclei differ significantly for the two animals; the nuclei which provide majority of inputs to the FN remain the same across the two animals (highlighted in green). This figure is adopted from (Guest et al., 2017).

Second-order neurons The variability in the innervation of vMN dendrites hinted at diverse pre-synaptic populations that might be providing input to these

vMNs. To investigate this further, all rabies positive neurons within the brain stem of both second-order animals were quantified. The brain stem nuclei identified in this process agreed with regions that have been previously reported as being pre-synaptic to the vMNs or other MNs of the FN (Takatoh et al., 2013; Hattox et al., 2002). The most prominent brain stem nuclei that were pre-synaptic to FN in these second-order animals were ipsilateral gigantocellular reticular nucleus (Gi containing ~10-40 times the number of vMNs), ipsilateral dorsal medullary reticular formation (MdD containing ~10 times the number of vMNs), ipsilateral intermediate reticular nucleus (IRt), ipsilateral spinal nucleus interpolaris (Sp5I) and the contralateral Gi (containing ~5 times the number of vMNs). In one of the two second-order animals (the animal in which vMN morphologies were reconstructed), 921 second-order neurons were labeled across 22 brain stem nuclei (see Figure 3.10A-C). Except for prepositus nucleus (Pr) and tectal spinal tract (ts), other 20 nuclei were previously reported as being pre-synaptic to FN. The largest second-order nuclei in this animal were Gi, IRt and MdD; containing 258, 97 and 87 rabies positive second-order neurons respectively in the ipsilateral hemisphere. The same nuclei contained 68, 28 and 28 second-order neurons in the contralateral hemisphere. Overall, the number of second-order neurons in the ipsilateral hemisphere (716) were 3.5 times the number of neurons in the contralateral hemisphere (205). In the second animal the number of second-order neurons were significantly lower, 104, across the 11 pre-synaptic nuclei in the brain stem. However, the largest nuclei remained MdD, Gi and IRt (see Figure 3.10D). The ratio between the number of second-order neurons across the two animals were consistent between the hemispheres; ~4 for ipsilateral and ~5 for contralateral.

Third-order neurons Another animal, which was sacrificed 84 hours after the muscle injection, exhibited rabies labeling beyond the brain stem but restricted to the layer 5 of the cortex. In this third-order animal, the cortical labeling was seen in vibrissal-related motor (vM1) and somatosensory (vS1 and S2) cortices (see Figure 3.8C). In the brain stem, the rabies had progressed to almost all nuclei and in the nuclei that were labeled in the second-order animals, the number of neurons labeled had increased by an order of magnitude (see Figure 3.8D). However, only 6 vMNs were labeled in the FN, reflecting the lack of interconnectivity in the ventro-

lateral FN. Additionally, about 15 neurons were labeled in the non-ventrolateral FN (medial).

Fourth-order (or higher) neurons In another animal that was sacrificed 108 hours after injection, the virus had spread to all layers of vM1 and vS1 (see Figure 3.8C) and to additional cortical areas; hence this animal was defined as having fourth-order (or higher) trans-synaptic spread. This animal showed increased labeling in all brain stem nuclei (compared to the third-order, see Figure 3.8D). The labeling in the ventrolateral FN remained sparse (see Figure 3.8B), whereas medial FN showed labeling of 57 neurons.

3.3 The vibrissal motor cortex reference frame and its applications

In the previous section, I presented the trans-synaptic tracing of rabies virus and defined the neuronal populations based on their synaptic distance from the terminal whisker muscle. In this section, I will focus on the third-order animals (that is rats in which the rabies-positive cortical neurons are confined to the layer 5 of the cortex) and use the third-order rabies-positive cortical neurons to derive the local reference frame for another brain region - vibrissal motor cortex (vM1). Specifically, I present the following: visualization and quantification of third-order rabies-positive cortical neurons (and the brain regions labeled by them), variability and precision of rabies defined vM1 reference frame, cellular organization of vM1 and its comparison with the cellular organization of the barrel cortex, and vM1 registered neuronal morphologies.

3.3.1 Third-order rabies-positive cortical neurons

Visualization of the third-order rabies-positive cortical neurons The method for injecting the replication competent rabies virus into the intrinsic whisker muscle of rats; as well as the subsequent methods for histology, imaging and quantification of anatomical landmarks - such as Pia surface and rabies labeled neuronal somata - have been described in the methods section (see 2.2.1, 2.3.1). These

methods were applied to three rats that were sacrificed after 3-5 days of survival period. The rabies labeling in the cortex was limited to layer 5 in these three rats (therefore these were defined as third-order animals). The Pia surfaces and the center locations of third-order rabies-positive neuronal somata of these three animals are visualized in the axial (top) view in the figure 3.11 A-C. One of the rat's brain (Animal 1) was sliced coronally, whereas the other two rat brains were sliced tangential to the barrel cortex. Tangentially sliced rat brains were aligned to the coronally sliced brain (treated as reference) along with all anatomical landmarks, as described in the method section. 3.11 D depicts the sensory sub-cortices, motor sub-cortices and Insular cortices as defined by the Paxinos rat brain atlas (see "List of abbreviations" for expansion of brain region names as per the atlas). After generating the surface triangulation for these atlas brain regions along with the Pia, they were aligned to the reference rat brain by aligning the respective Pia surfaces using the ICP algorithm. The aligned rabies landmarks (combined from three animals) are superimposed onto the atlas brain areas in order to visualize the main regions that were labeled by the rabies virus. Figures 3.12 and 3.13 visualize the same data as in Figure 3.11, but in coronal and sagittal views respectively. For better visualization of rabies labelling in the coronal view, cortex was clipped perpendicular to the C-R axis and parts spanned by the rabies virus labeling are shown one below the other respectively (tentatively termed as vM1 and vS1). Similarly, in the sagittal view, left and right hemispheres are shown one below the other respectively.

Quantification of the rabies clusters The number of rabies-positive cortical neurons increased from Animal 1-3, with the average number of neurons being 1452. The variability of number of neurons was high with a standard deviation (SD) of 1296 neurons and a coefficient of variation (CoV) of 89%. In each animal, these cortical rabies-positive neurons were clustered into tentative motor (vM1) and sensory (vS1) clusters in each hemisphere using "k-means" clustering as mentioned in the methods section. The number of neurons in each of these clusters are plotted in Figure 3.17A. The absolute number of rabies-positive neurons within each cluster varied widely across the three animals with CoVs of 106%, 95%, 128% and 98% for vM1 LHS, vM1 RHS, vS1 LHS, vS1 RHS clusters respectively. How-

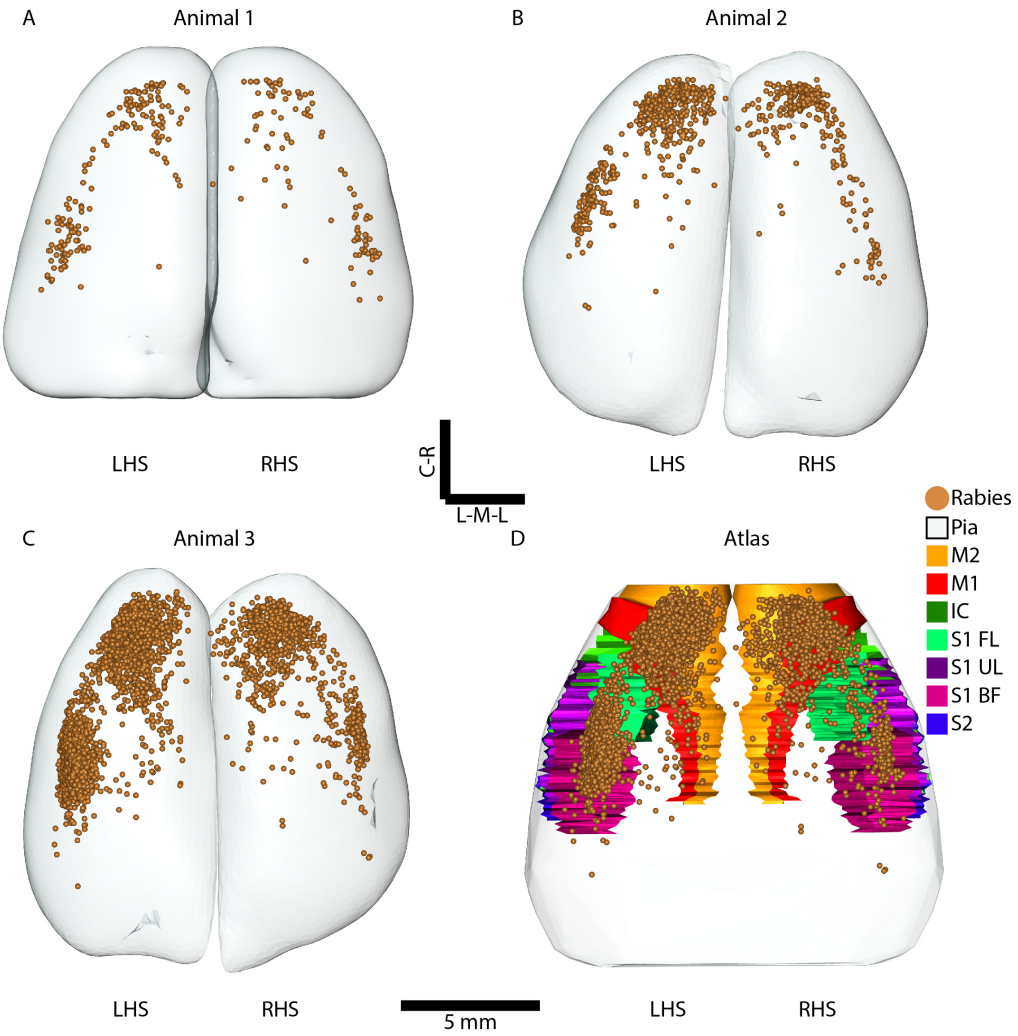

Figure 3.11. Visualization of the third-order rabies-positive cortical neurons (axial view). A-C. Pia surfaces as well as the center locations of rabies-positive cortical neuronal somata of three third-order animals respectively. Although all three animals are third-order, the quantity of rabies-positive cortical neurons increases exponentially from Animal 1 to Animal 3. D. Certain cortical brain regions as per the Paxinos rat brain atlas that were labeled by the rabies virus. Surface triangulation have been generated for Pia and other brain regions of the atlas by following the same procedure as for the Pia surface generation of rats A-C. The Pia of the atlas was aligned to Animal 1 along with the atlas brain regions. The rabies-positive cortical neurons from the three animals (A-C) were aligned to each other (with Animal 1 being the reference) by aligning their Pia surfaces. The combined rabies-positive cortical neurons are superimposed onto Paxinos atlas to visualize the atlas cortical regions labeled by the rabies virus.

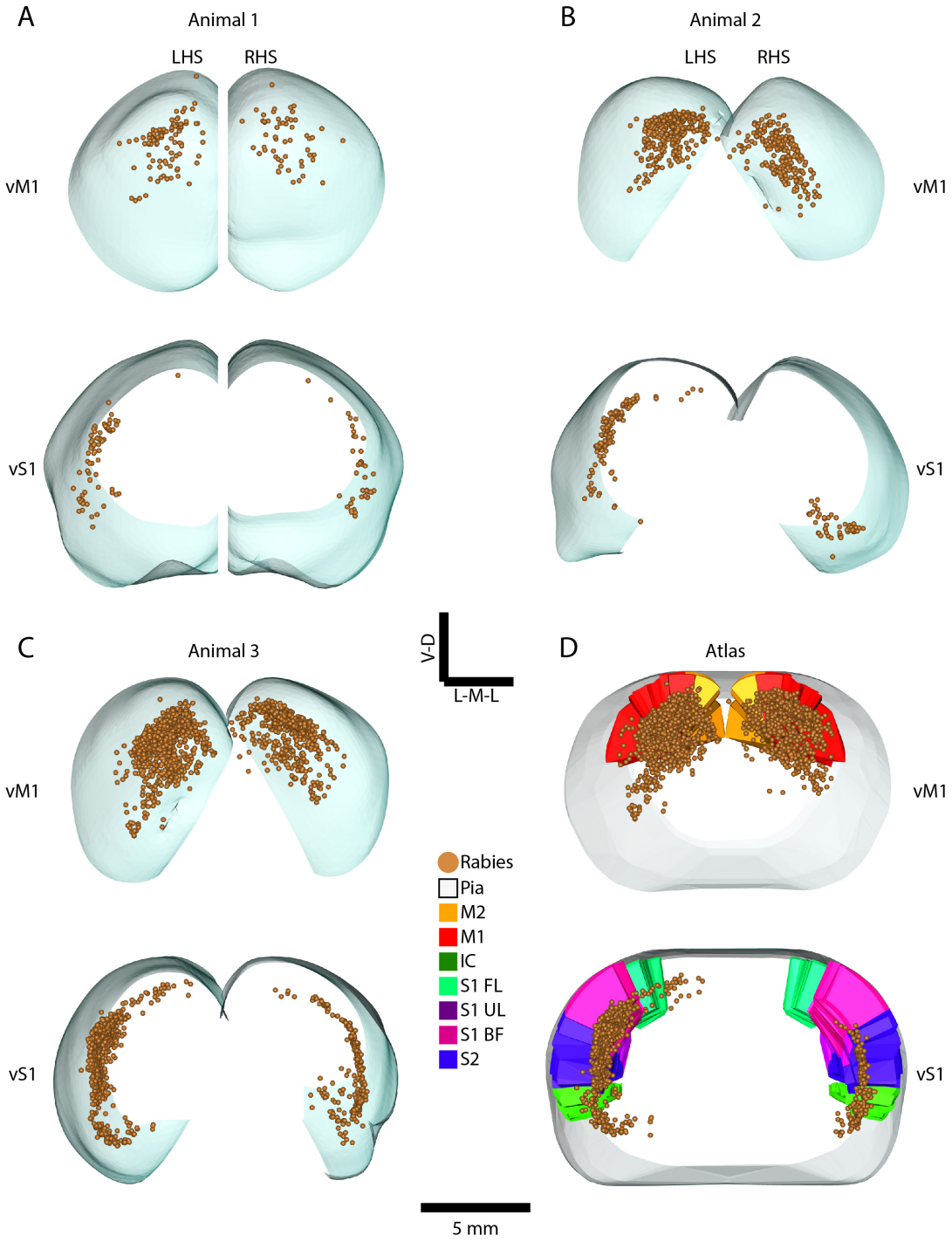

Figure 3.12. Visualization of the third-order rabies-positive cortical neurons (coronal view). Same data as shown in 3.11, visualized in the coronal view. For better visualization, cortex was clipped perpendicular to the C-R axis so as to extract parts spanned by the rabies virus labeling (tentatively termed as vM1 and vS1).

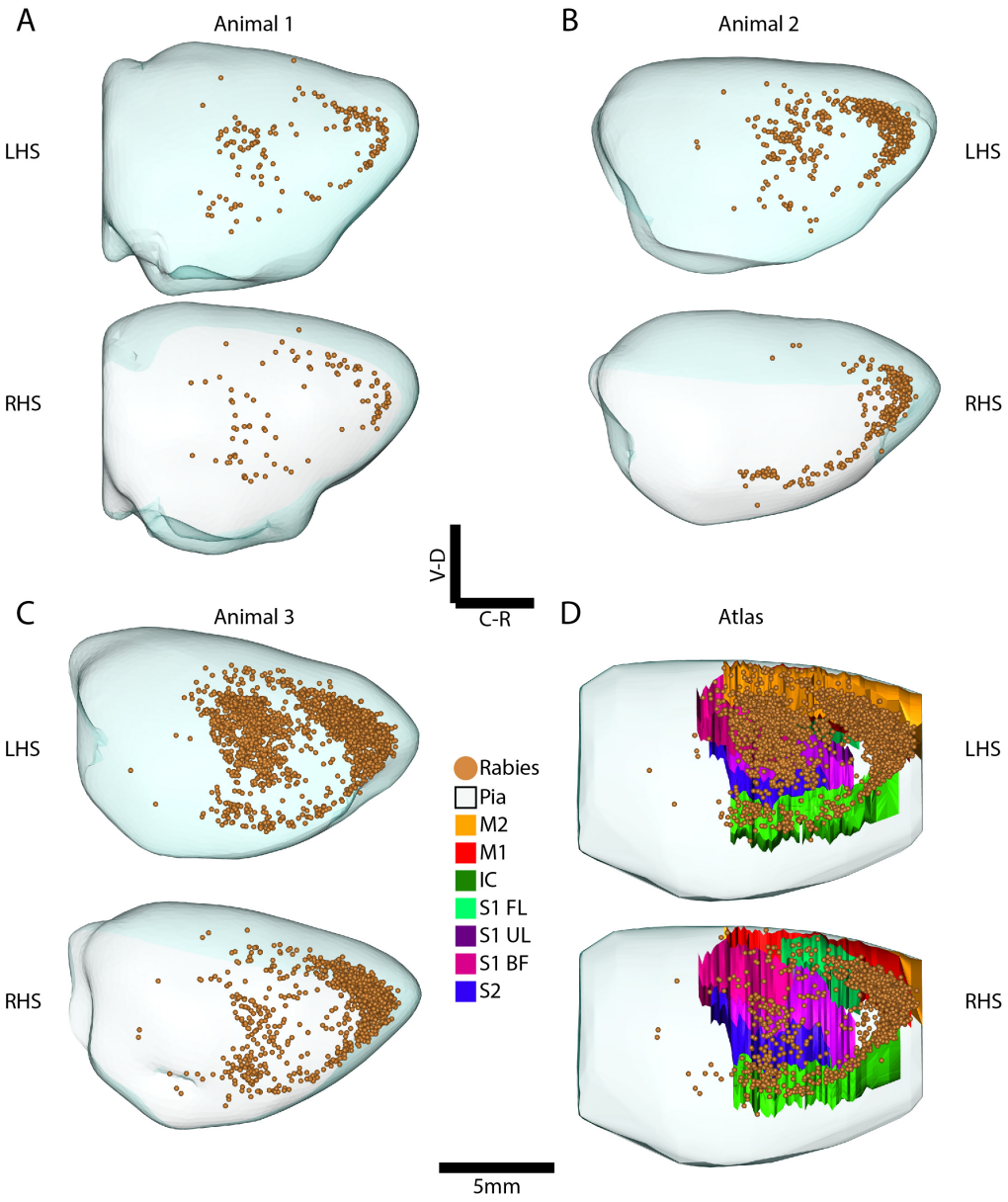

Figure 3.13. Visualization of the third-order rabies-positive cortical neurons (sagittal view). Same data as shown in 3.11, visualized in the sagittal view. For better visualization, the two hemispheres are shown one below the other.

ever, the ratio of the number of neurons in the LHS as compared with the number of neurons in the RHS within each animals varied less significantly across animals. Across motor clusters the LHS had an increase of 172% ± 19% (mean ± SD) as compared to the RHS, with a CoV of 11%, whereas across the sensory clusters this ratio was 291% ± 108% with a CoV of 37%.

Outlier removal using density thresholding After the initial separation of tentative motor and sensory rabies clusters, these clusters were further processed by removing the outlier in each cluster using the density thresholding method described in the methods section. This process is visualized in the axial view in Figure 3.14 A-C, wherein each of the four clusters of each animal are visualized as the density images with densities color coded as heat-maps. The density image volume of each rabies cluster was generated using a grid resolution of 400 μm^3 and maximally projected onto the axial plane for visualization. Similar to the number of neurons in each cluster, the peak density of each cluster also varied widely across the three animals having CoVs of 81%, 77%, 101% and 53% for vM1 LHS, vM1 RHS, vS1 LHS, vS1 RHS clusters respectively. The ratio of peak densities of LHS to RHS in each animal varied less widely across animals for the motor clusters, having ratio of 2 ± 0.5 with a CoV of 24%; whereas the ratios varied widely for the sensory clusters with ratio of 1.9 ± 1.1 (CoV=59%). Each density image volume was binarized using relative lower thresholds at multiples of 10% of peak density. For example, if the lower threshold used is 10% of peak density, this means that every voxel of the density image volume which has a density equal to or above 10% of peak density will be set as high and rest of the voxels will be set to zero. At each threshold, the binary image volume was converted into an iso-surface. The iso-contours (maximally projected onto the axial plane) corresponding to the iso-surfaces generated using thresholds of 100% of peak density, 50% of peak density and 10% of peak density are shown for each cluster in the Figure 3.14 A-C. Figure 3.17B shows the exponential reduction in the number of neurons (as well as the surface area of the iso-surfaces enclosing those neurons) for different density thresholds (in steps of 10% of peak cluster density) across all four clusters of three animals (N=12). An increase in the lower threshold of 10% corresponds to 21% (± 14%) reduction in the total number of rabies-positive neurons within the

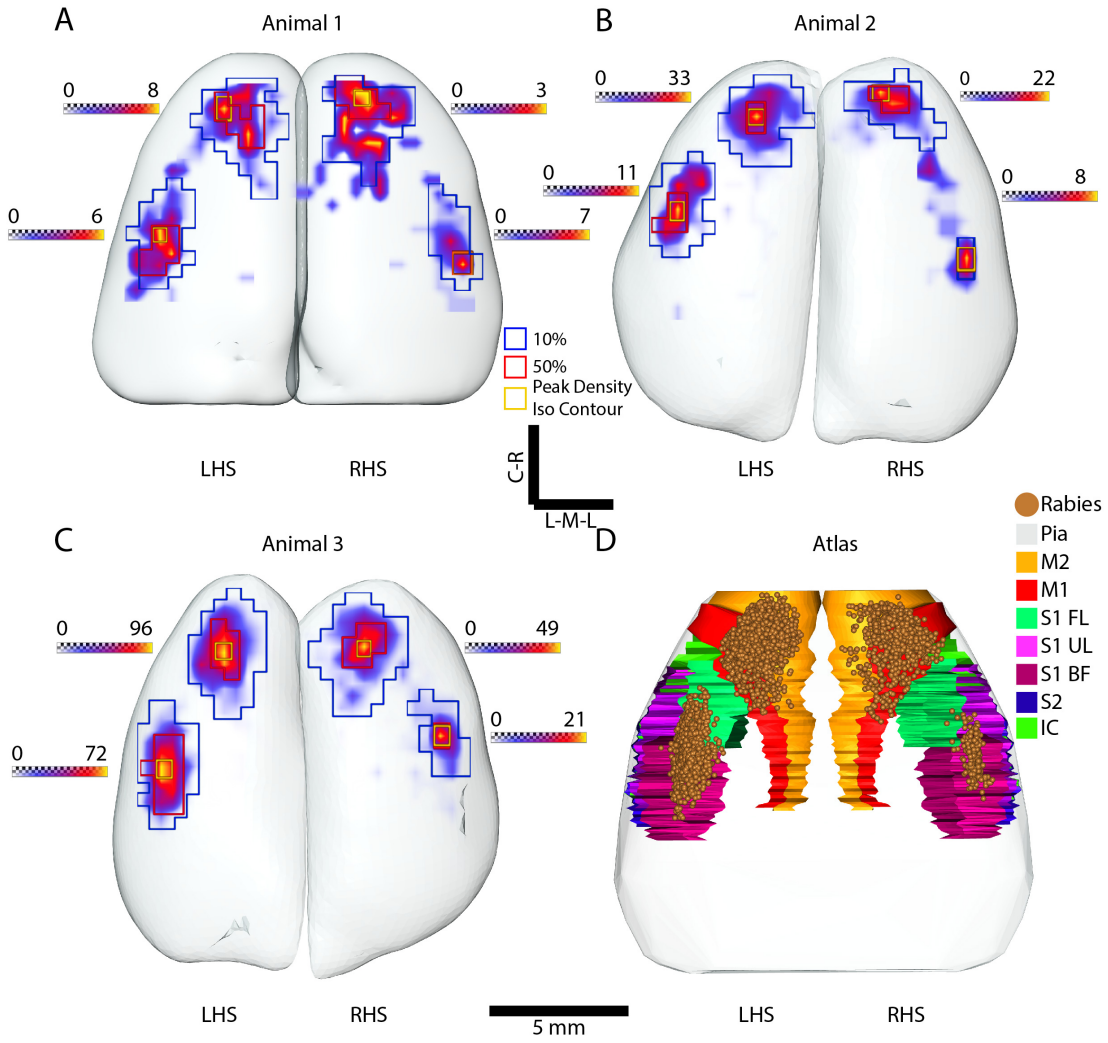

Figure 3.14. Visualization of the rabies clusters as density images (axial view). A-C. Same data that is shown in Figure 3.11 A-C, however, each rabies cluster is visualized as density image volume, instead of visualizing the center locations of rabies labeled somata as spheres. Each rabies cluster is converted into a density image by using a grid whose resolution is 400 μm^3 and densities are color coded using a color map. The minimum and maximum (peak) density for each cluster is also shown. Each density image is then binarized using lower thresholds that are expressed as a percentage of respective cluster's peak density. The iso-contours corresponding to the binary images obtained using the thresholds of 10%, 50% and 100% of peak density are visualized with color-coding. The peak densities of each cluster varies across animals - increasing from Animal 1 to Animal 3. The density image as well the iso-contours are projected maximally onto the axial plane for visualization. D. Same data as shown in 3.11 D, however, instead of all rabies-

Figure 3.14. positive cortical neurons, the validated neurons after removing the outliers in each cluster (using a threshold of 10%) are registered to the Paxinos atlas from three animals. The various brain regions that are labeled by the validated rabies clusters are visualized with color coding.

clusters; whereas it corresponds to a 66% (±16%) reduction in the corresponding surface areas. The reductions get less drastic with the increasing threshold. This shows that the 10% threshold gets rid of more than half of the area covered by the spurious rabies-positive neurons while removing only a fraction of neurons from the cluster. Thus, 10% of peak density is used as the threshold for selecting valid rabies-positive neurons in each cluster. The volumes occupied by the rabies clusters after validation are 9.1 ± 1.5 mm^3, 7.4 ± 4.1 mm^3, 8.6 ± 6.4 mm^3 and 4.8 ± 3.3 mm^3 for vM1 LHS, vM1 RHS, vS1 LHS and vS1 RHS respectively (see Figure 3.17 C). Although, the number of rabies-positive cortical neurons were highly variable across third-order animals (CoV=89%), they consistently labeled brain regions of similar volumes (after outlier removal) in the LHS of these animals with CoVs of 16% and 7% respectively for motor and sensory clusters. The labeling in the RHS, however, were less consistent with CoVs of 56% and 69% respectively for motor and sensory clusters. Therefore, the motor cluster of LHS (vM1 LHS) and its local reference frame is used for subsequent analysis, although the results are presented for all four clusters.

Distribution of the rabies labeled cortical neurons amongst the atlas defined regions The valid rabies clusters from all three animals were combined (after alignment) and registered to the atlas as described before. This is shown in the panel D of Figures 3.14, 3.15 and 3.16. The extent to which certain cortical brain regions (as defined by the Paxinos atlas) have been labeled by these rabies-positive cortical neurons across the three third-order animals is quantified in Figure 3.18 by counting the number of rabies-positive cortical neurons within each of those brain regions of interest. The motor cortex was the most labeled region in both hemispheres. The second most labeled region was the sensory cortex in the LHS and the insular cortex in the RHS. Within the motor cortex, M1 (primary motor cortex) received 31% ± 6% labeling in the LHS and 33% ± 13% labeling in the

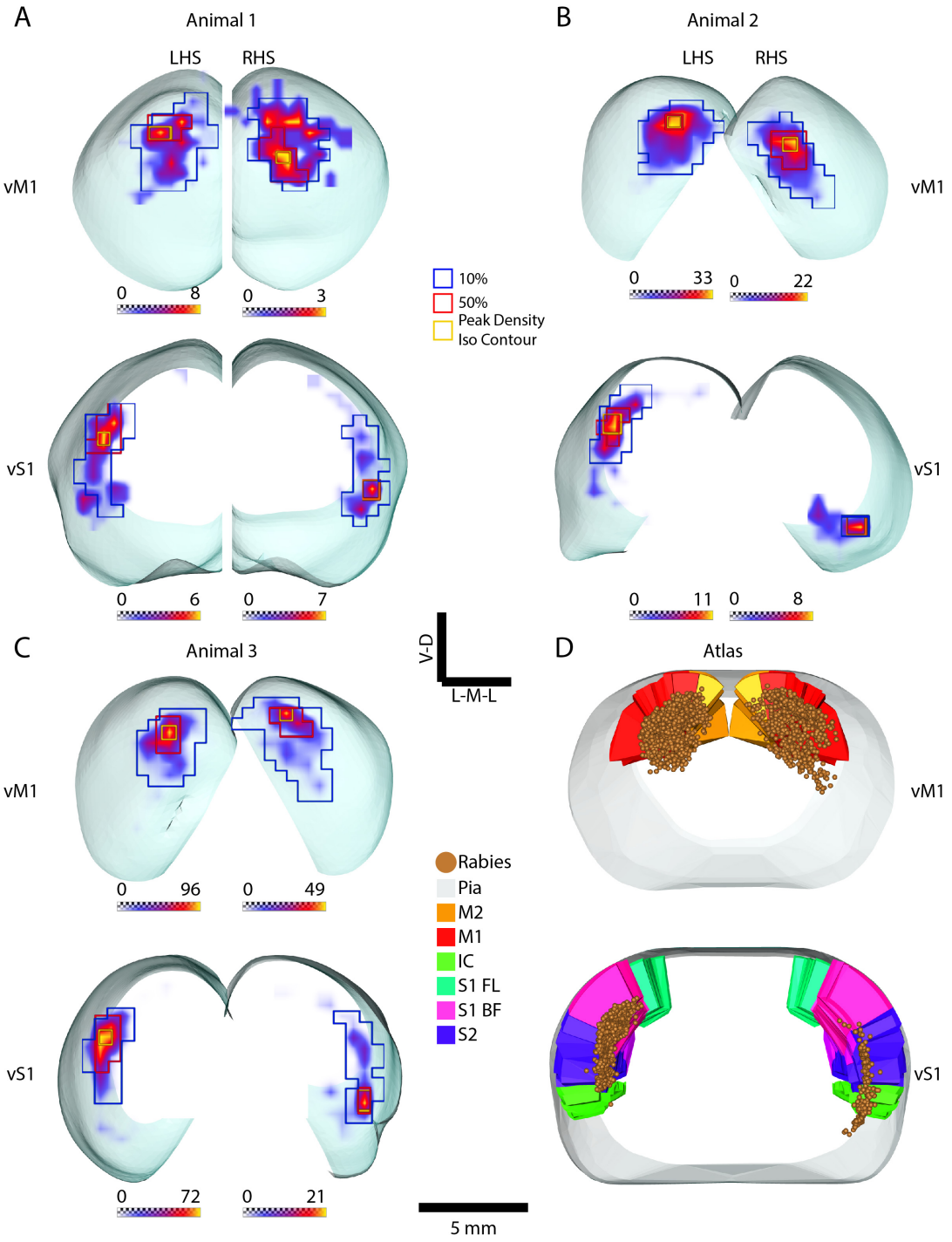

Figure 3.15. Visualization of the rabies clusters as density images (coronal view). Same data as shown in 3.14, visualized in the coronal view. For better visualization, cortex was clipped perpendicular to the C-R axis so as to extract parts spanned by the vM1 and vS1 clusters and visualized one below the other.

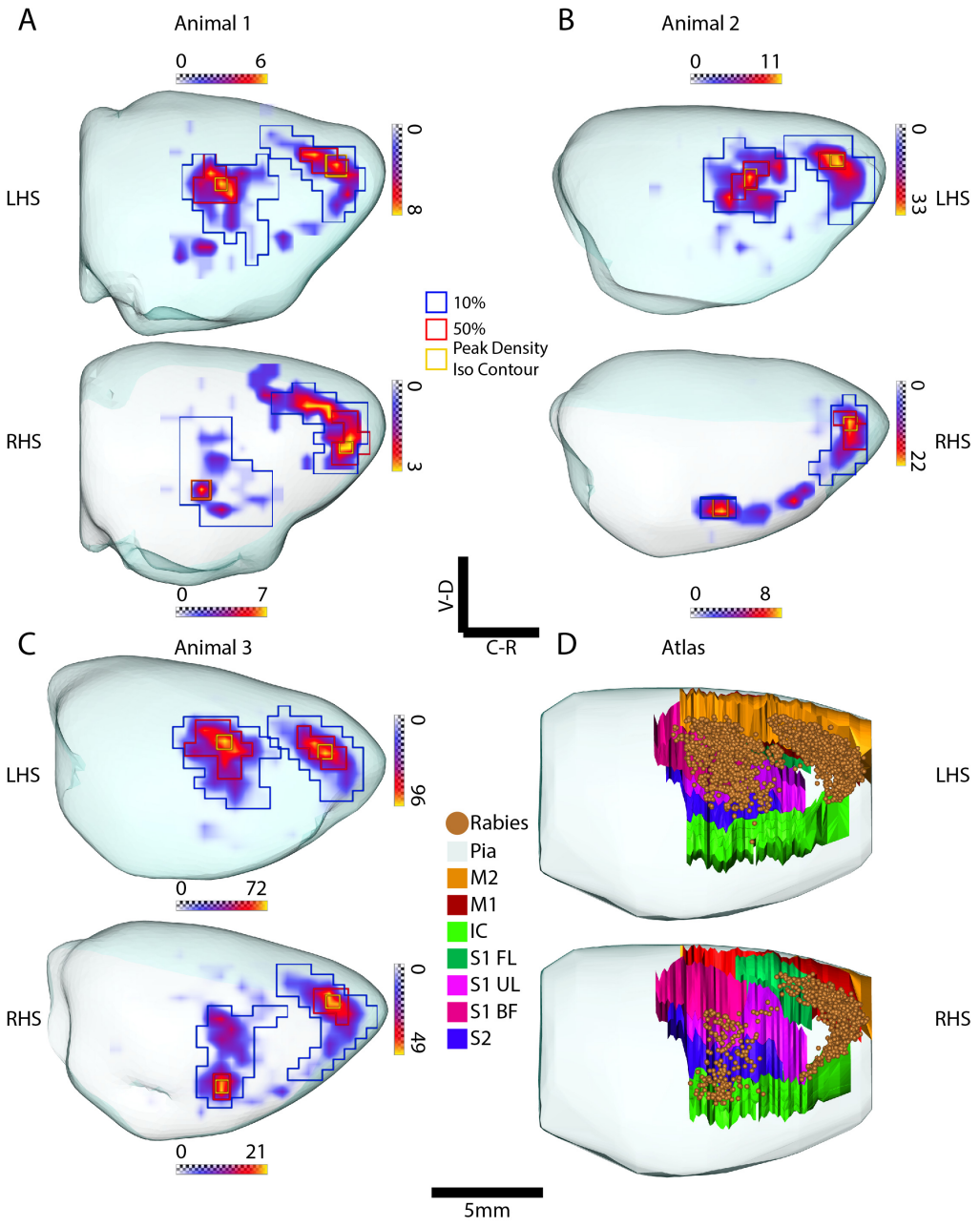

Figure 3.16. Visualization of the rabies clusters as density images (sagittal view). Same data as shown in 3.14, visualized in the sagittal view. For better visualization, the two hemispheres are shown one below the other.

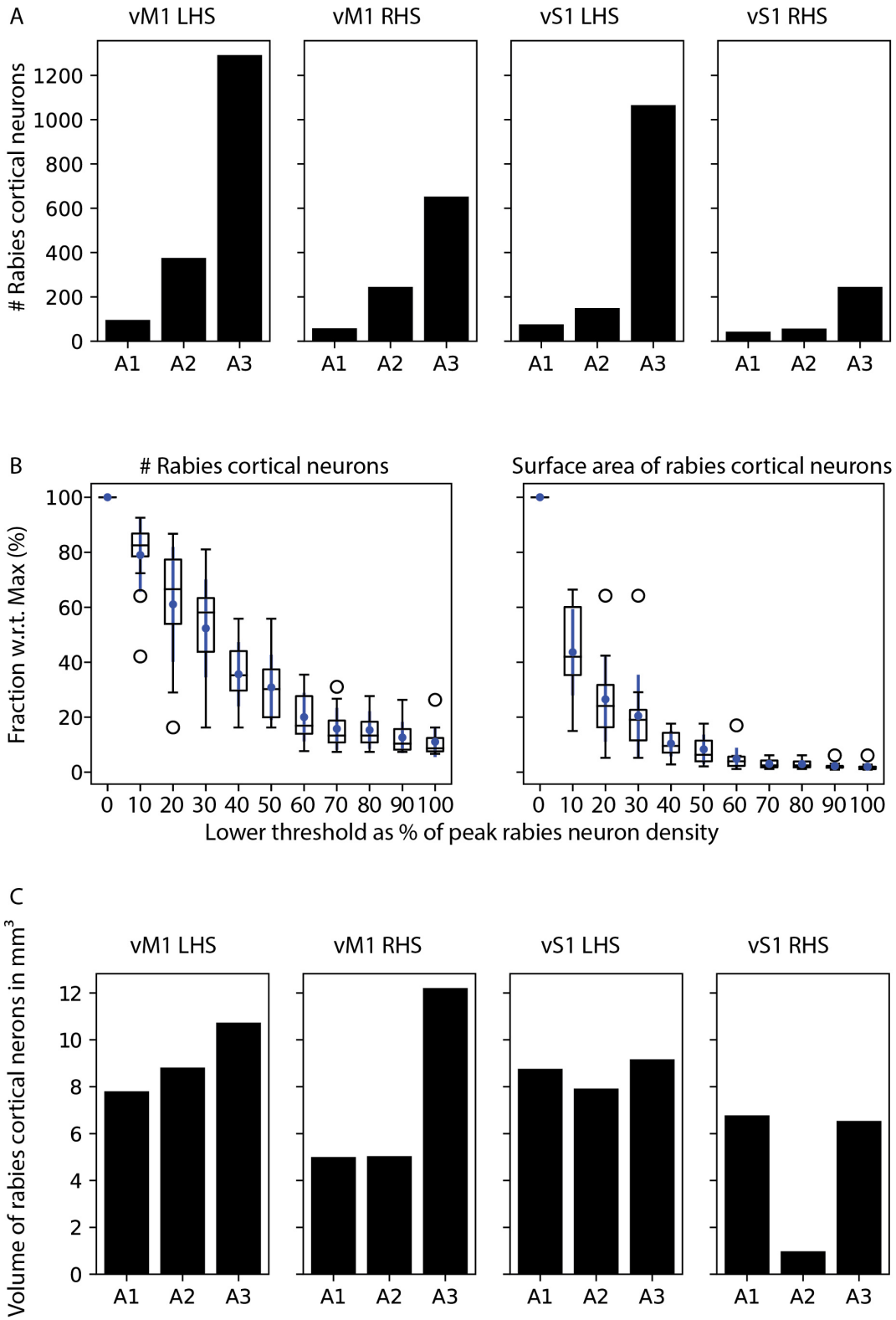

Figure 3.17. Quantification of the rabies clusters. A. Quantification of the rabies-

Figure 3.17. positive neuronal somata in each "k-means" cluster. The number of rabies-positive neuronal somata increases exponentially from Animal 1 to Animal 3 in each cluster; with high CoVs of 106%, 95%, 128% and 98% for vM1 LHS, vM1 RHS, vS1 LHS, vS1 RHS clusters respectively. The mean ± SD of number of rabies positive neuronal somata in those clusters were 588 ± 626, 319 ± 304, 430 ± 552 and 115 ± 113 respectively in vM1 LHS, vM1 RHS, vS1 LHS, vS1 RHS clusters. B. Effect of lower threshold on percentage number of neurons selected in each cluster (left panel) as well as their respective surface areas (right panel) during density based clustering for outlier removal. The number of neurons selected and their surface areas reduce exponentially as the lower threshold used for binarizing the cluster's density image is increased in steps of 10% of peak density. A lower threshold of 10% of peak density corresponds to a reduction of 21% ± 14% of neurons (averaged across four clusters of three animals, N=12), whereas the same threshold corresponds to getting rid of 66% ± 16% of surface area occupied by spurious neurons. The percentage removal of neurons and their surface areas get less drastic as the lower threshold is increased in steps of 10% of peak density. Therefore, 10% of peak density is used as the lower threshold for outlier removal from each cluster. C. Quantification of volume occupied by the valid rabies clusters (after outlier removal using 10% of peak density as threshold). The volumes are 9.1 ± 1.5 mm^3, 7.4 ± 4.1 mm^3, 8.6 ± 6.4 mm^3 and 4.8 ± 3.3 mm^3 for vM1 LHS, vM1 RHS, vS1 LHS and vS1 RHS respectively. Unlike the number of neurons in the initial clusters, which have high variability in each cluster across animals, the validated clusters have lower variability with volumes occupied by those clusters having CoVs of 16%, 7%, 56% and 69% respectively for vM1 LHS, vS1 LHS, vM1 RHS, vS1 RHS clusters.

RHS. Although, the average labeling of M1 was similar across the two hemispheres, the labeling in the LHS was more consistent across animals (CoV = 18%) as compared with that of the RHS (CoV = 40%). Labeling in the M2 (secondary motor cortex) varied more widely across animals, having received rabies labeling of 9% ± 5% (CoV = 53%) and 13% ± 10% (CoV = 78%) respectively in the LHS and the RHS. The sensory cortex in the LHS received labeling prominently in S1B (primary somatosensory cortex - barrel field or barrel cortex) and S1U (primary somatosensory cortex - upper lip region) sub-cortices containing 17% ± 9% and 11% ± 0% of rabies-positive neurons respectively. Whereas the somatosensory cortex labeling in the RHS was negligible with S1B and S1U respectively receiving 2% ± 3% and 3% ± 4%. The S2 (secondary somatosensory cortex) received

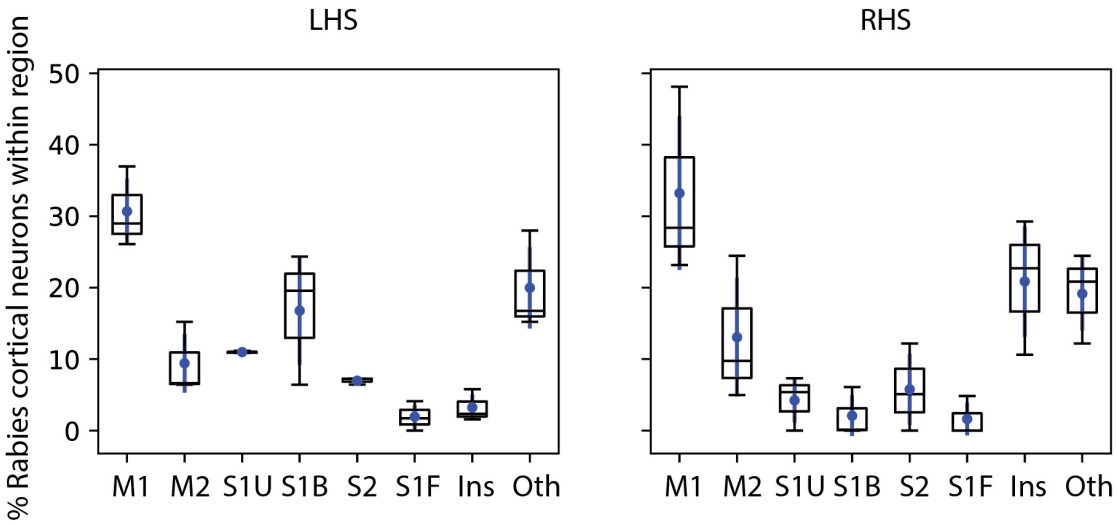

Figure 3.18. Distribution of the rabies labeled cortical neurons amongst the atlas defined regions. The extent to which certain cortical brain regions (as defined by the Paxinos rat brain atlas) are labeled by the rabies virus in the third-order animals is quantified in the left (for the LHS) and right (for the RHS) panels. The motor cortex was the most labeled amongst cortical regions in both hemispheres with the M1 receiving 31% ± 6% and 33% ± 13% labeling respectively in the LHS and the RHS. The M2 received 9% ± 5% and 13% ± 10% labeling respectively in the LHS and the RHS. The sensory sub-cortices S1B and S1U respectively received labeling of 17% ± 9%, 11% ± 0% in the LHS and a negligible 2% ± 3%, 3% ± 4% in the RHS. The S2 received 7% ± 0% and 6% ± 6% labeling in the LHS and the RHS respectively. The S1F received a negligible share of 2% ± 2% and 2% ± 3% labeling in the LHS and the RHS respectively. The insular cortex labeling was prominent in the RHS (21% ± 9%); whereas in the LHS it was negligible (3% ± 2%).

labeling of 7% ± 0% and 6% ± 6% in the LHS and the RHS respectively. The S1F (primary somatosensory cortex - forelimb region) received 2% ± 2% and 2% ± 3% labeling in the LHS and the RHS respectively, indicating that the sensory cortex labeling in third-order animals was primarily restricted to the facial (vibrissal and upper lip) areas. The insular cortex received a prominent labeling of 21% ± 9% in the RHS; whereas in the LHS the labeling was 3% ± 2%.

3.3.2 The rabies defined reference frames

Variability of the rabies defined reference frames As seen in the previous subsection, out of the four cortical rabies clusters, the vM1 cluster in the LHS consistently labels the same cortical region across animals (after removing outliers). Therefore, this cluster is utilized to generate the reference frame using the procedure described in the method section. For comparison, the same method is also applied for the remaining three clusters and the respective reference frames are generated (vM1 RHS, vS1 LHS and vS1 RHS). These four reference frames in each animal are visualized in the three canonical views (axial, coronal and sagittal) in Figures 3.19, 3.20 and 3.21 respectively. The surface areas and the volumes of these reference frames are quantified in Figure 3.22. The vM1 reference frame in the LHS was most consistent out of the four clusters, having a total surface area of 60 mm^2 ± 5 mm^2(CoV=8%), Pia surface area of 34 mm^2 ± 2 mm^2 (CoV=7%) and volume of 30 mm^3 ± 3 mm^3 (CoV=10%). Whereas, the vM1 reference frame in the RHS was more varied having a total surface area of 54 mm^2 ± 13 mm^2 (CoV=24%), Pia surface area of 31 mm^2 ± 10 mm^2 (CoV=33%) and volume of 26 mm^3 ± 9 mm^3 (CoV=35%). The vS1 reference frame in the LHS had a total surface area of 65 mm^2 ± 12 mm^2 (CoV=18%), Pia surface area of 26 mm^2 ± 6 mm^2 (CoV=24%) and volume of 25 mm^3 ± 4 mm^3 (CoV=15%). The vS1 reference frame in the RHS was the most inconsistent of the four clusters, with a total surface area of 43 mm^2 ± 24 mm^2 (CoV=57%), Pia surface area of 20 mm^2 ± 13 mm^2 (CoV=65%) and volume of 16 mm^3 ± 11 mm^3 (CoV=67%).

The extent and orientation of the PAs of these reference frames are quantified in Figure 3.23A,B respectively. The first PA had the largest extent, whereas the extents of the second and third PAs were comparable with each other. The three PAs of the vM1 reference frame in the LHS had extents of 5 mm ± 0.5 mm (CoV=10%), 2.8 mm ± 0.3 mm (CoV=9%) and 2.7 mm ± 0.2 mm (CoV=6%) respectively. The extents of the PAs of the vM1 in the RHS were respectively 4.5 mm ± 0.5 mm (CoV=11%), 2.3 mm ± 0.5 mm (CoV=23%) and 2.8 mm ± 0.2 mm (CoV=6%). The vS1 reference frame in the LHS had PA extents of 4.5 mm ± 0.5 mm (CoV=12%), 3.3 mm ± 0.2 mm (CoV=7%) and 1.8 mm ± 0.03 mm (CoV=2%) respectively. The vS1 of the RHS was most variable across animals

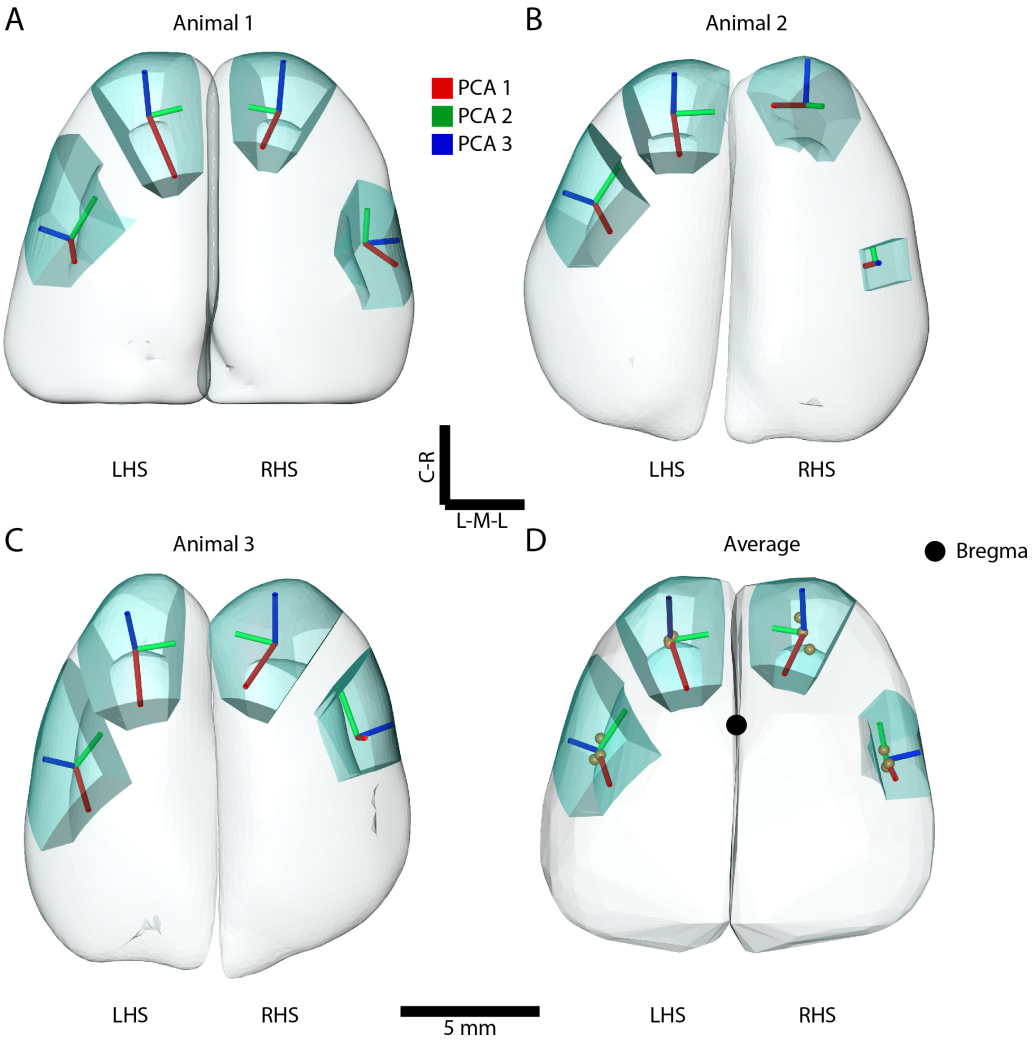

Figure 3.19. Visualization of the rabies defined reference frames (top view). A-C. The rabies defined local reference frames of the three third-order animals. The Pia surfaces of the three animals as well as the four local reference frames derived from the valid rabies clusters for each animal are shown in the top view. Each reference frame is derived from each of the rabies clusters by first obtaining the PA of the rabies cluster through PCA; then extracting the portion of Pia and WM of cortical hemisphere spanned by the rabies cluster using the extent and orientation of the PAs. The PAs of each reference frame is shown color coded with red, green and blue colors respectively. D. Standardized reference frames along with the average Pia surfaces. The centers of aligned rabies clusters are shown for each reference frame, wherein the respective rabies clusters have been aligned with each other by aligning their respective rabies cluster surfaces from the three animals. The precision of aligning the vM1 LHS, vM1 RHS, vS1 LHS and vS1 RHS were respectively 137 µm ± 49 µm, 170 µm ± 53 µm, 166 µm ± 59 µm and

Figure 3.19. 336 µm ± 114 µm. The centroids of these aligned cluster centers form the origin of each average reference frame. The PAs of the average reference frames have extents and orientations that are the average of respective individual reference frame's PA extents and orientations. The orientational precisions of the aligned PAs of vM1 LHS, vM1 RHS, vS1 LHS and vS1 RHS reference frames were respectively 6° ± 2°, 10° ± 3°, 10° ± 4° and 25° ± 6° (averaged across the three PAs for each average reference frame). Using the origin and PAs, the average reference frame volumes were extracted from the average Pia and WM surfaces. The average Pia and WM surfaces were generated from the aligned individual Pia and WM surfaces using the "ray casting" approach. The position of the bregma is identified on the average Pia surface by aligning the Paxinos atlas's Pia surface to the average Pia surface.

with the PAs having extents of 3.6 mm ± 1.5 mm (CoV=42%), 2.4 mm ± 0.7 mm (CoV=29%) and 1.3 mm ± 0.6 mm (CoV=44%).

The orientation of each PA is measured by projecting it onto the horizontal (axial) plane and measuring its orientation with respect to the coronal plane (visible in the axial view) as well as its elevation with respect to the horizontal plane (visible in the coronal or sagittal views). All angles are measured in the anti-clockwise direction. The first PA of the vM1 reference frame in the LHS was most parallel to the mid-line (C-R axis) with orientations of 102° ± 8° and 127° ± 3° with respect to the coronal and horizontal planes respectively. The second PA was most parallel to the coronal and the horizontal planes, having orientations of 8° ± 4° and 175° ± 8° respectively. The third PA had orientations of 96° ± 6° and 37° ± 3° with coronal and horizontal planes respectively. The first PA of the vM1 reference frame in the RHS was most perpendicular to the horizontal plane with orientations of 40° ± 29° and 108° ± 10° with respect to the coronal and horizontal planes respectively. The second PA was most parallel to the coronal plane having orientations of 171° ± 4° and 20° ± 9° respectively with coronal and horizontal planes. The third PA was most perpendicular to the coronal plane having orientations of 88° ± 2° and 17° ± 11° respectively with coronal and horizontal planes. The three PAs of the vS1 reference frame in the LHS had orientations of 108° ± 8°, 56° ± 3° and 163° ± 3° respectively with the coronal plane; whereas the orientation with respect to the horizontal plane were 124° ± 5°, 28° ± 8° and

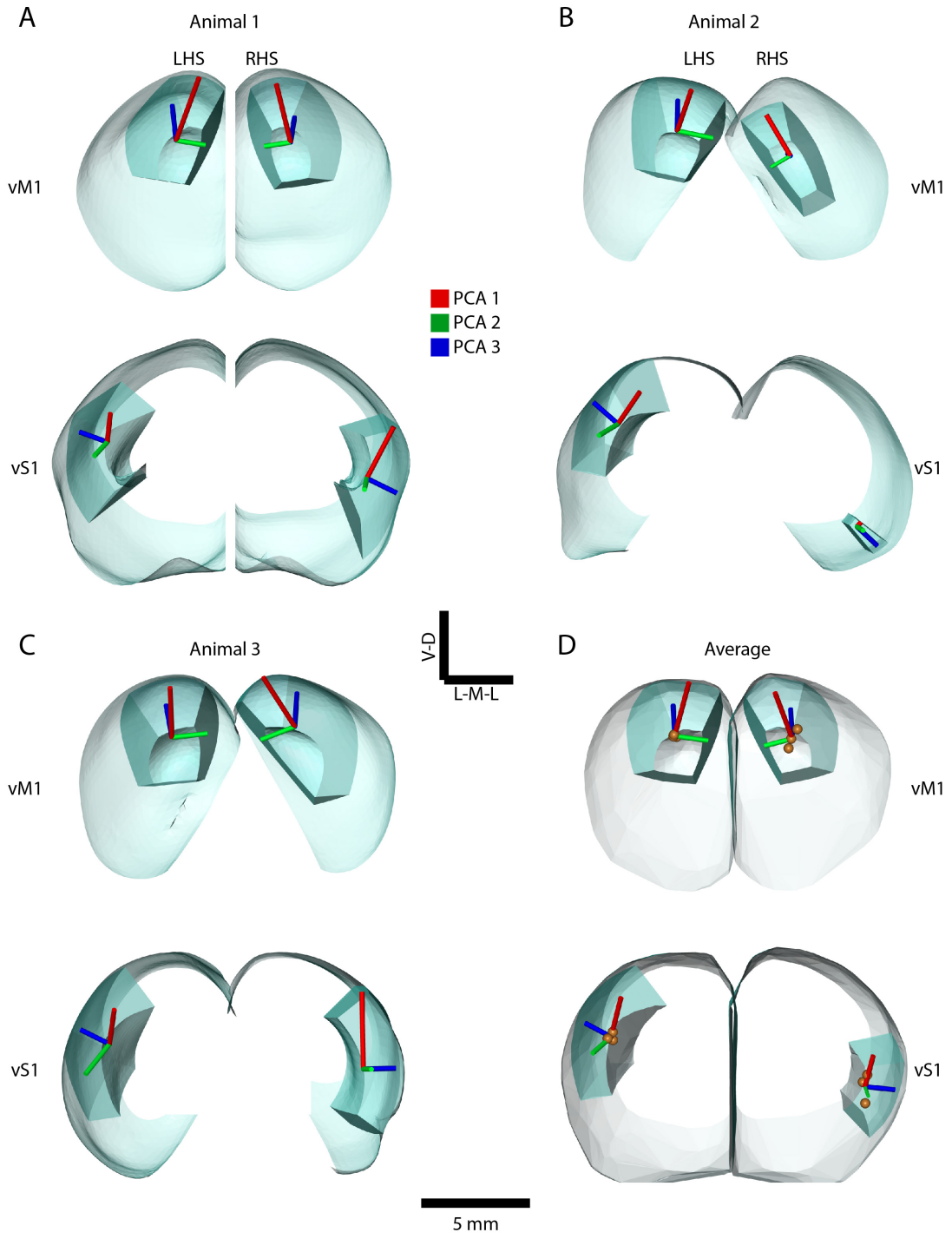

Figure 3.20. Visualization of the rabies defined reference frames (coronal view). Same data as shown in 3.19, visualized in the coronal view. For better visualization, cortex was clipped perpendicular to the C-R axis and the vM1 and vS1 reference frames are shown one below the other.

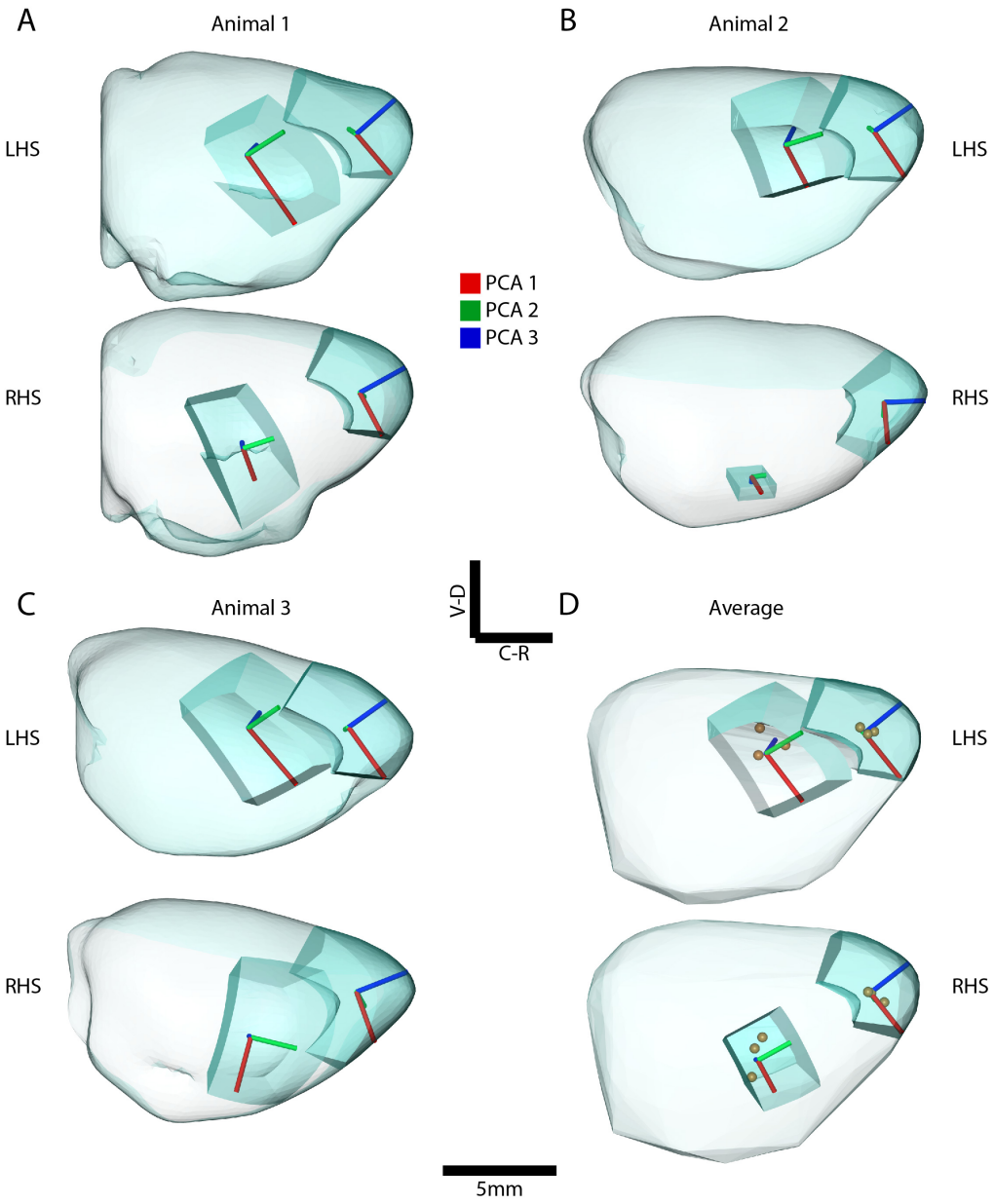

Figure 3.21. Visualization of the rabies defined reference frames (sagittal view). Same data as shown in 3.19, visualized in the sagittal view. For better visualization, the two hemispheres are shown one below the other.

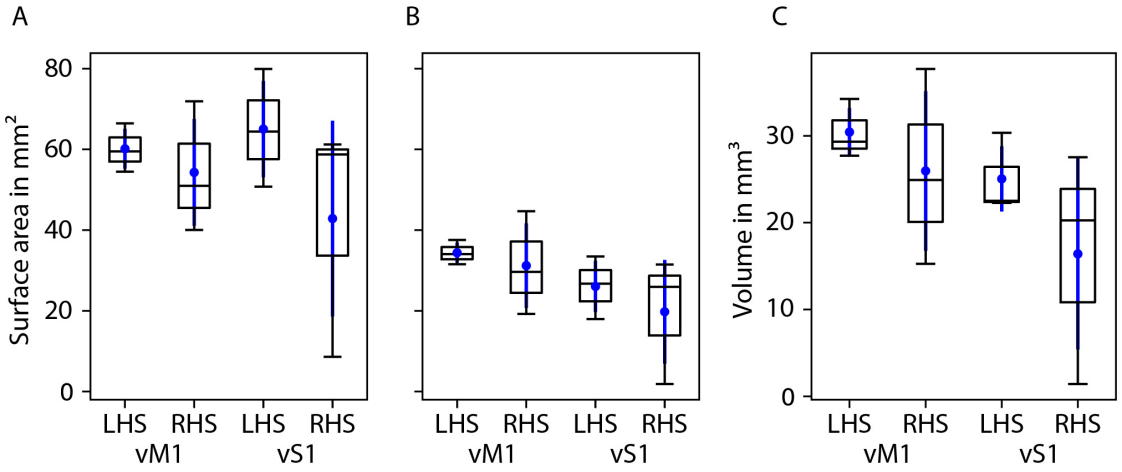

Figure 3.22. Variability of the rabies defined reference frames: surface area and volume. A. Total surface areas of the rabies defined reference frames. The total surface areas of the vM1 LHS, vM1 RHS, vS1 LHS and vS1 RHS reference frames were respectively $60\,mm^2 \pm 5\,mm^2$, $54\,mm^2 \pm 13\,mm^2$, $65\,mm^2 \pm 12\,mm^2$ and $43\,mm^2 \pm 24\,mm^2$. B. The Pia surface areas of the rabies defined reference frames. The Pia surface areas of the vM1 LHS, vM1 RHS, vS1 LHS and vS1 RHS reference frames were respectively $34\,mm^2 \pm 2\,mm^2$, $31\,mm^2 \pm 10\,mm^2$, $26\,mm^2 \pm 6\,mm^2$ and $20\,mm^2 \pm 13\,mm^2$. C. Volumes of the rabies defined reference frames. The volumes of the vM1 LHS, vM1 RHS, vS1 LHS and vS1 RHS reference frames were respectively $30\,mm^3 \pm 3\,mm^3$, $26\,mm^3 \pm 9\,mm^3$, $25\,mm^3 \pm 4\,mm^3$ and $16\,mm^3 \pm 11\,mm^3$. The vM1 reference frame in the LHS was the most consistent amongst the four reference frames, having a CoV of 9% (averaged across surface area and volume). The vS1 reference frame in the RHS was the least consistent amongst the four reference frames, having a CoV of 62%.

$151° \pm 9°$ respectively. The three PAs of the vS1 reference frame in the RHS had orientations of $172° \pm 21°$, $99° \pm 10°$ and $9° \pm 9°$ respectively with the coronal plane; whereas the orientations with respect to the horizontal plane were $102° \pm 20°$, $4° \pm 13°$ and $157° \pm 18°$ respectively.

Distance of the reference frames from the Bregma Along with the Paxinos atlas brain surface, the bregma position (as defined by the atlas) was also aligned to the reference animal brain surface. The position of the reference frames were measured with respect to the Bregma by measuring the distance between the center of the rabies cluster (origin of the reference frame) and the Bregma. The results

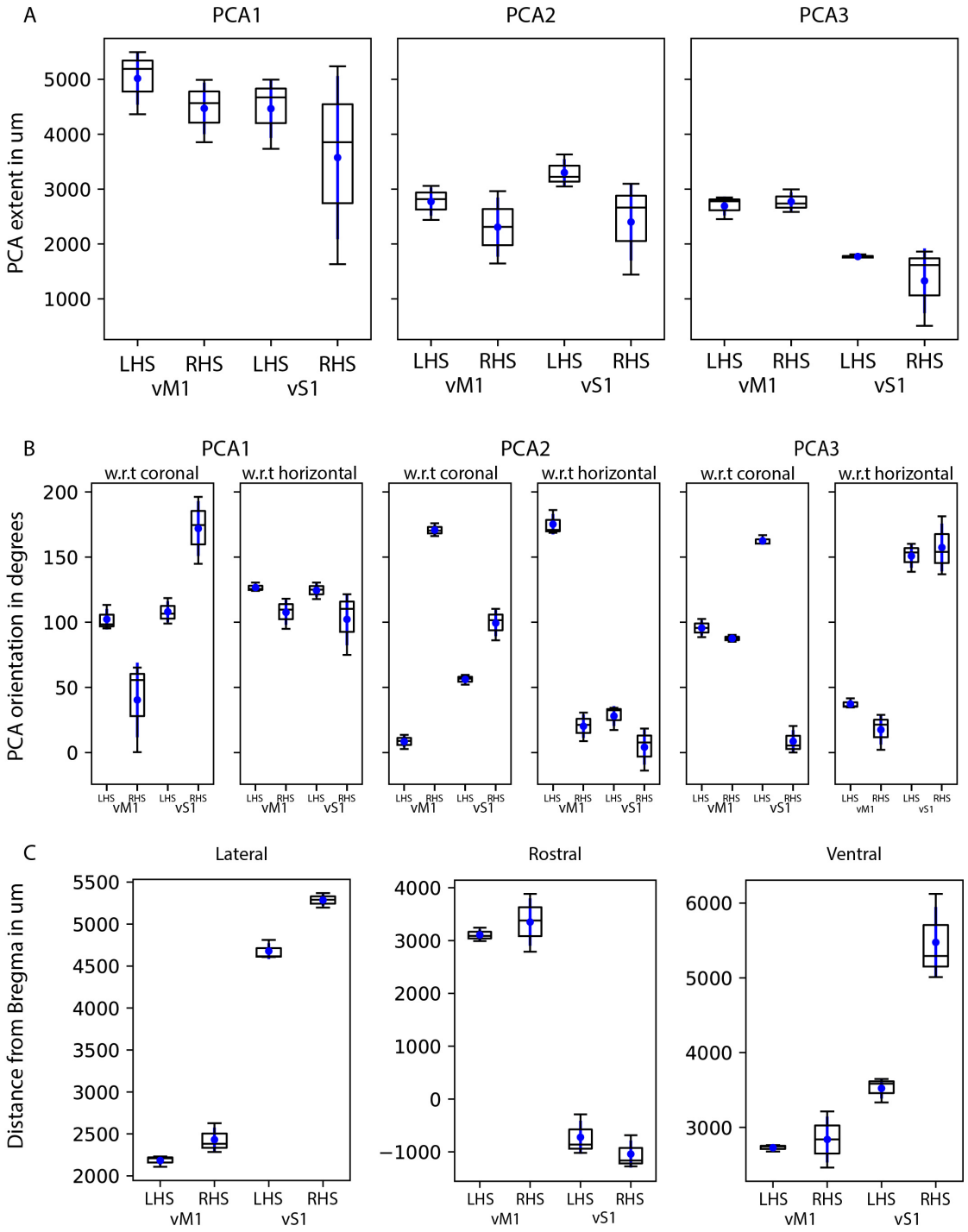

Figure 3.23. Variability of the rabies defined reference frames: PAs and distance from the Bregma. A. Extents of the PAs of the rabies defined reference frames. The three PAs of the vM1 reference frame had extents of 5 mm ± 0.5 mm, 2.8 mm ± 0.3 mm and 2.7 mm ± 0.2 mm respectively in the LHS; and extents of 4.5 mm ± 0.5 mm, 2.3 mm ± 0.5 mm and 2.8 mm ± 0.2 mm in the RHS. The vS1 reference

Figure 3.23. frame had PA extents of 4.5 mm ± 0.5 mm, 3.3 mm ± 0.2 mm and 1.8 mm ± 0.03 mm respectively in the LHS; and 3.6 mm ± 1.5 mm, 2.4 mm ± 0.7 mm and 1.3 mm ± 0.6 mm in the RHS. B. Orientations of the PAs of the rabies defined reference frames. The orientation of the three PAs of the vM1 reference frame with respect to the coronal plane were respectively 102° ± 8°, 8° ± 4° and 96° ± 6°. The elevation of these three PAs with respect to the horizontal plane were respectively 127° ± 3°, 175° ± 8° and 37° ± 3°. Similarly, the orientation of the three PAs of vM1 reference frame in the RHS were respectively 40° ± 29°, 171° ± 4° and 88° ± 2° with respect to the coronal plane; 108° ± 10°, 20° ± 9° and 17° ± 11° with respect to the horizontal plane. The orientation of the three PAs of vS1 reference frame in the LHS were respectively 108° ± 8°, 56° ± 3° and 163° ± 3° with respect to the coronal plane; 124° ± 5°, 28° ± 8° and 151° ± 9° with respect to the horizontal plane. The orientation of the three PAs of vS1 reference frame in the RHS were respectively 172° ± 21°, 99° ± 10° and 9° ± 9° with respect to the coronal plane; 102° ± 20°, 4° ± 13° and 157° ± 18° with respect to the horizontal plane. C. Positions of centers of rabies defined reference frames with respect to the bregma. The center (origin) of vM1 reference frame in the LHS was positioned 2.2 mm ± 0.05 mm lateral, 3.1 mm ± 0.1 mm rostral and 2.7 mm ± 0.04 mm ventral to the bregma. The center of vM1 reference frame in the RHS was positioned 2.4 mm ± 0.1 mm lateral, 3.4 mm ± 0.5 mm rostral and 2.8 mm ± 0.3 mm ventral to the bregma. The center of vS1 reference frame in the LHS was positioned 4.7 mm ± 0.1 mm lateral, 0.7 mm ± 0.3 mm caudal and 3.5 mm ± 0.1 mm ventral to the bregma. The center of vS1 reference frame in the RHS was positioned 5.3 mm ± 0.07 mm lateral, 1 mm ± 0.3 mm caudal and 5.5 mm ± 0.5 mm ventral to the bregma.

are plotted in the Figure 3.23 C. The center of the vM1 reference frame in the LHS was located 2.2 mm ± 0.05 mm (CoV=2%) lateral, 3.1 mm ± 0.1 mm (CoV=3%) rostral and 2.7 mm ± 0.04 mm (CoV=1%) ventral with respect to the Bregma across the three animals. Similarly, the vM1 reference frame in the RHS was positioned 2.4 mm ± 0.1 mm (CoV=6%) lateral, 3.4 mm ± 0.5 mm (CoV=13%) rostral and 2.8 mm ± 0.3 mm (CoV=11%) ventral with respect to the Bregma. The vS1 reference frame in the LHS was positioned 4.7 mm ± 0.1 mm (CoV=2%) lateral, 0.7 mm ± 0.3 mm (CoV=43%) caudal and 3.5 mm ± 0.1 mm (CoV=4%) ventral with respect to the Bregma. Whereas, the vS1 reference frame in the RHS was positioned 5.3 mm ± 0.07 mm (CoV=1%) lateral, 1 mm ± 0.3 mm (CoV=25%) caudal and 5.5 mm ± 0.5 mm (CoV=9%) ventral to the Bregma.

Precision and standardization of the vM1 reference frame The inter-animal variability of vM1 reference frame in the LHS was the least among the four clusters having a dimensional CoV of 8.6% (averaged across surface area, volume and extent of the PAs) and positional CoV (averaged across the distances of the reference frame center from the bregma along M-L, C-R and D-V axes) of 2%. The vS1 reference frame in the LHS was the next most consistently labeled cluster with dimensional and positional CoVs being 11% and 16% respectively. The dimensional and positional variability of vM1 and vS1 reference frames in the RHS were 20% and 10% as well as 48% and 12% respectively. Given the small variance of vM1 reference frame in the LHS, I proceeded to align the reference frames from three animals and quantified their precision. After aligning the rabies clusters (by aligning the rabies cluster's surface triangulations), the precision was measured at the center of the rabies cluster as well as the Pia and WM surfaces of the reference frame as explained in the methods section. For the vM1 reference frame in the LHS, these precisions were 137 µm ± 49 µm, 161 µm ± 52 µm and 125 µm ± 26 µm respectively. For comparison, I quantified the precisions for the remaining three clusters as well. The vM1 reference frame in the RHS was comparatively less precise, having precisions of 170 µm ± 53 µm, 277 µm ± 70 µm and 289 µm ± 80 µm respectively at the center, Pia and WM. The vS1 reference frame in the LHS had comparable precisions of 166 µm ± 59 µm, 166 µm ± 56 µm and 263 µm ± 96 µm; whereas the vS1 in the RHS was the least precise with precisions of 336 µm ± 114 µm, 374 µm ± 136 µm and 391 µm ± 82 µm at the center of the cluster, Pia surface and WM surface respectively. The orientational (angular) precision of vM1 LHS - as measured by the mean of individual PA's precision across three animals - was 6° ± 2°. For the remaining three clusters (vM1 RHS, vS1 LHS, vS1 RHS), these precisions were 10° ± 3°, 10° ± 4° and 25° ± 6° respectively.

From the above analysis, it is clear that the rabies virus consistently labeled the same region in the motor cortex of the LHS; as evidenced by the low variance and high precision. Therefore, I proceeded to generate an average reference frame from the three aligned reference frames of the vM1 LHS. First, I generated the average cortical hemispheres using the "ray casting" approach, as explained in the methods section. Second, I extracted the standard reference frame from the average hemisphere, whose center as well as the extent and orientation of the

PAs were set to be the mean of the aligned individual reference frame's center, extent of PAs and orientation of PAs respectively. For completeness, I repeated the process for the remaining three clusters. The average cortical hemispheres and the four standard reference frames are visualized in the three canonical views (axial, coronal, sagittal) in the panel D of Figures 3.19, 3.20 and 3.21 respectively.

3.3.3 Cellular organization of the vM1 reference frame

In the previous subsection, I described the geometry, position and precision of the vM1 reference frame. In this subsection, I will delineate the cellular organization of the vM1 reference frame along with its layer borders. Additionally, I will describe the layer borders of the barrel cortex reference frame for comparison.

Layer borders of the vM1 reference frame The method for obtaining the layer borders of the vM1 reference frame using its neuronal density has been detailed in the methods section (see 2.3.2). This method has been applied for the vM1 reference frames of the aforementioned third-order animals. The resulting neuronal density images, average density profiles and the derived layer borders have been visualized in the Figure 3.24 for each vM1 reference frame. Additionally, the average layer borders across the three animals have also been visualized. In order to visualize the neuronal density of each vM1 reference frame, a 200 µm wide region on either side of the first PA of the vM1 reference frame was clipped, where the clipping planes were parallel to first and third PAs. All NeuN positive neurons (counted in the 2D image sections) that lie within the clipped region were then converted into a density image volume using a grid resolution of 200 μm^3. The density image volume is visualized as a heat map in the sagittal view of its local reference frame, which means that the viewing angle is perpendicular to the first and third PAs of the vM1 reference frame. In addition to the NeuN density, the rabies positive neurons that lie within the clipped region are also visualized. All NeuN positive neurons that lie within the vM1 reference frames were utilized to obtain the density profiles by uniformly sampling each vM1 reference frame using axis fields. In each vector of the axis field, the neuronal density within a radius of 250 µm was determined in steps of 50 µm from Pia to WM. All density

profile lengths were then normalized to a cortical thickness of 2600 µm. An average density profile (mean ± SD), averaged across all normalized density profiles of the reference frame, is visualized for each reference frame (N=6) in the Figure 3.24. Additionally, the average density profile of the rabies-positive neurons are also shown for each reference frame. Using the variations of the neuronal density along the cortical depth, the layer borders were derived for each density profile and the average layer borders for each vM1 reference frame have been visualized as horizontal lines in the Figure 3.24. In each vM1 reference frame, the average layer borders were used to create iso-surfaces at the lower borders of L1, L2/3, L5A and L5B layers respectively. The methods for generating the density profiles and subsequently deriving the layer borders from them have been explained in the methods section (see 2.3.2).

After deriving the layer borders, the number of rabies-positive neurons contained within the layer 5 were determined for each animal. 99.6%±0.9% of rabies-positive cortical neurons of vM1 were located in the layer 5 (averaged across six reference frames), whereas, 99%±1% were located specifically in the layer 5B. This verifies that we are indeed analyzing third-order rat brains, where the cortical spread of rabies virus is limited to the layer 5.

The lower borders of L1, L2/3, L5A and L5B layers were respectively at the depths 8.5%±2%, 21%±8%, 39%±6% and 78%±9% below the Pia. The borders are expressed as a percentage of cortical thickness (normalized to 2600 µm) that are averaged across all density profiles of six vM1 reference frames (N=387). In Figure 3.25A, these layer borders are compared with the vM1 borders obtained in the study (Hooks et al., 2011); wherein the vM1 layer borders were obtained by visually inspecting the bright field images of vM1 for neuronal density variations along the Pia-WM axis (except for L5B border, which was taken to be at mid distance between L5A border and the WM). The lower borders of L1, L2/3, L5A and L5B layers according to this study were at the depths of 10%±1%, 16%±1%, 34%±2% and 67%±0% respectively from the Pia; which are comparable to the layer borders presented here. Figure 3.25B shows the distribution of mean layer borders of the six vM1 reference frames as box plots, along with the mean and SD. The precision of layer borders, as given by the SD of means of the layer borders of six reference frames, were 1.2% (31 µm), 1.1% (27 µm), 0.6% (16 µm), 1.8% (47 µm)

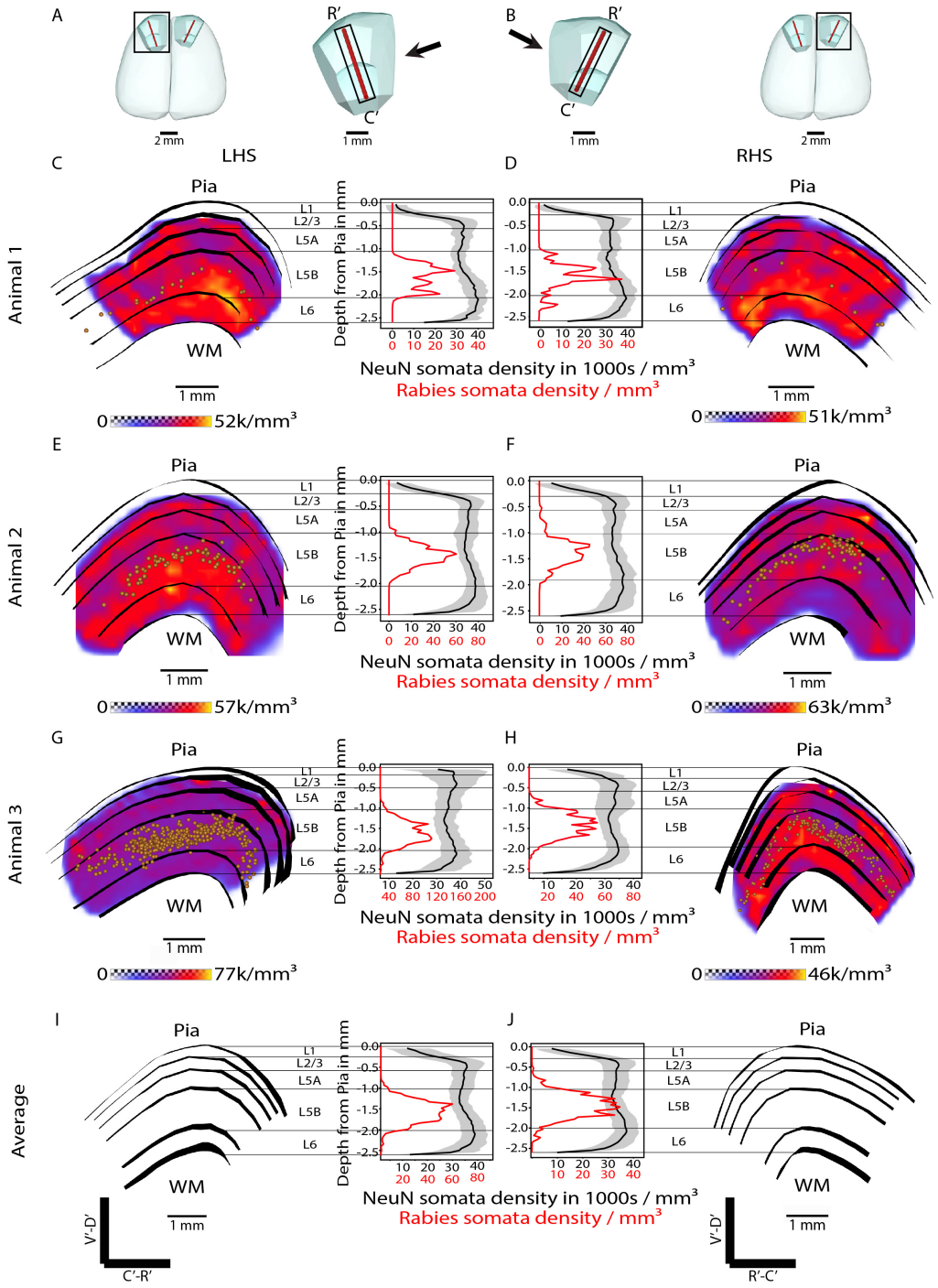

Figure 3.24. Layer borders of the vM1 reference frame. A-B. Schematic of the viewing angles used for the subsequent visualization of layer borders of the left and right vM1 reference frames respectively. A 200 µm wide region on either side of the first PA is used for the visualization of layer borders. C. Left: The sagittal view of the vM1 of Animal 1 (LHS), where a 400 µm wide region around the first

Figure 3.24. PA of the vM1 reference frame is clipped using clipping planes that are parallel to the central axis (third PA) of the reference frame. The NeuN positive neurons contained within the region have been converted into a density image volume using a 200 µm^3 grid resolution. The density image volume is visualized as a heat map with appropriate color coding. The average lower border of each layer is visualized both as a horizontal line and also as an iso-surface. Right: The average neuronal density profile of the vM1 reference frame of LHS of Animal 1, averaged across all vectors of the axis field (shown in black). The error band indicates the SD. Similar process is applied to obtain the average density profile of rabies-positive neurons of the vM1 reference frame (shown in red). Please note the different scales used for the NeuN and rabies density profiles (in black and red respectively). D. Same data as in panel C, but for the RHS of Animal 1. E-H. Same data as in the previous row but for Animal 2 and 3 respectively. I-J. Average NeuN density profile, average rabies density profile, layer borders and the layer border iso-surfaces for the average LHS and RHS respectively.

respectively for L1, L2/3, L5A and L5B layers. Therefore, the precision of layer borders of vM1 across all layers was 30 µm ± 11 µm.

Laminar organization of the vM1 reference frame The neuronal density computations described above were based on the cell counts performed in the 2D image sections (one image per 50 µm thick brain section). However, in order to delineate the cellular organization, the real (3D) cell count needs to be estimated by scaling up the 2D cell counts. This was achieved by first imaging a sample region - 250 µm radius around the central axis of the vM1 reference frame of Animal 3 LHS - in 3D and then by performing the automated cell counting of all NeuN labelled somata within the 3D image volume stack of this region. A 3D neuronal density profile was generated from these 3D cell counts. The scaling factors needed for estimating the real cell counts were then obtained by determining the factors needed for scaling the average 2D density profile of this (Animal 3 LHS) reference frame in order to match the 3D profile in a layer-wise manner. These scaling factors were 0.1, 2.3, 3.1, 2.4 and 2 for L1, L2/3, L5A, L5B and L6 layers respectively. These scaling factors were applied to the average 2D density profile of each vM1 reference frame in a layer-wise manner; by multiplying the average 2D density of each layer by its respective layer scaling factor. The 3D neuronal density of each

layer thus estimated was then multiplied by its respective layer volume to obtain the 3D cell count. The process of estimating the 3D cell counts and the respective scaling factors are depicted in the Figure 3.25 C; whereas, the layer-wise volumes, number of neurons and the neuronal densities are shown in Figure 3.25 D-F.

The layer-wise breakup of the vM1 reference frame volumes across the three animals in the LHS were $2.5\,mm^3 \pm 0.3\,mm^3$, $3.9\,mm^3 \pm 0.5\,mm^3$, $5.6\,mm^3 \pm 1.2\,mm^3$, $12.1\,mm^3 \pm 0.9\,mm^3$ and $6.4\,mm^3 \pm 1.2\,mm^3$ respectively for L1, L2/3, L5A, L5B and L6 layers. The volumes of these respective layers in the RHS had larger variability, owing to the larger variability of the vM1 reference frame volume in the RHS ($2.3\,mm^3 \pm 0.9\,mm^3$, $3.1\,mm^3 \pm 1.6\,mm^3$, $4.6\,mm^3 \pm 2.1\,mm^3$, $10\,mm^3 \pm 4.2\,mm^3$ and $5.8\,mm^3 \pm 2.6\,mm^3$). The estimated 3D cell counts per layer were proportional to the layer volumes. In the LHS the number of neurons (in thousands) in each layer were respectively 3.5 ± 3.3, 286 ± 77, 613 ± 150, 1007 ± 62 and 436 ± 74; whereas in the RHS the cell counts (in thousands) were 3.5 ± 3.3, 227 ± 125, 481 ± 222, 802 ± 307 and 362 ± 132 respectively for L1, L2/3, L5A, L5B and L6 layers. The resulting neuronal densities (expressed as 1000 neurons per mm^3) were 1.6 ± 1.6, 73 ± 12, 108 ± 5, 84 ± 2 and 68 ± 2 in the LHS; 1.4 ± 0.9, 72 ± 4, 104 ± 3, 81 ± 3 and 63 ± 5 in the RHS.

Comparing the cellular organization of the vM1 with the vS1 A comparison of the volume, number of neurons and the neuronal density of the vM1 and vS1 (barrel cortex) reference frames is presented in Figure 3.25 G. The data shown for the vS1 reference frame are obtained from the study (Meyer et al., 2013). The methods employed for the histology, image acquisition and the automated cell counting in that study were similar to the methods employed for the vM1 reference frame presented in this thesis. The cell counting in the study (Meyer et al., 2013) was performed in 3D image stacks, as opposed to the 2D cell counting performed for the vM1 reference frame in the current study . The volume of the vM1 reference frame was on average four times that of the vS1 reference frame ($28\,mm^3 \pm 7\,mm^3$ (N=6) vs $6.6\,mm^3 \pm 0.6\,mm^3$ (N=4)); the number of neurons in the vM1 reference frame were also on average four times the number of neurons present in the vS1 reference frame (2110 ± 601 vs 530 ± 39 thousands). The resulting densities of the two reference frames were comparable with the vS1 having slightly higher

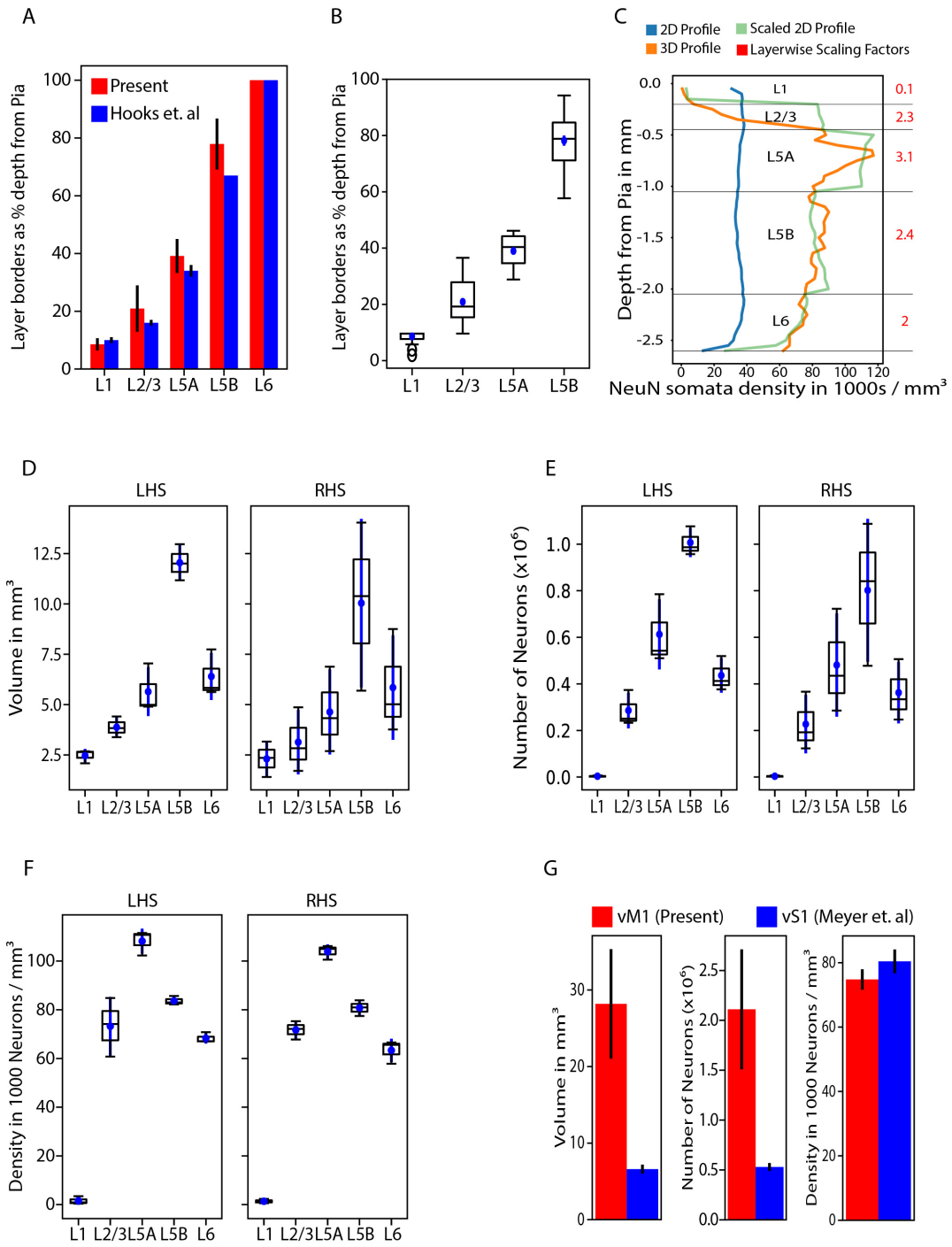

Figure 3.25. Laminar organization of the vM1 reference frame. A. vM1 layer border comparison between present and (Hooks et al., 2011). The average (averaged across all density profiles of six reference frames; N=387) lower borders of L1, L2/3, L5A and L5B layers determined in the current study were at the depths of

Figure 3.25. 8.5%±2%, 21%±8%, 39%±6% and 78%±9% respectively from the Pia; which are comparable to the borders presented in (Hooks et al., 2011) - 10%±1%, 16%±1%, 34%±2% and 67%±0%. B. Precision of the vM1 layers borders. The precisions - as given by the SD of means of the layer borders of six reference frames - for L1, L2/3, L5A and L5B layers respectively were 31 µm, 27 µm, 16 µm and 47 µm. C. Estimating 3D cell counts. The layer-wise scaling factors required for scaling up the 2D cell counts were determined by dividing the average 3D density of each layer of the central axis of the vM1 reference frame of Animal 3 LHS by corresponding layer's average 2D density of vM1 reference frame of Animal 3 LHS. The average 2D density profile, 3D density profile of the central axis and the scaled 2D density profile are shown with color coding. The scaling factors thus obtained were 0.1, 2.3, 3.1, 2.4 and 2 for L1, L2/3, L5A, L5B and L6 layers respectively. D-F. Layer-wise breakup of volumes, number of neurons (estimated 3D counts) and densities of the vM1 reference frame. The LHS and RHS layer volumes are shown separately since the variability of the vM1 reference frame volume in the RHS was large as compared to the LHS. This yielded the corresponding large variability in the number of neurons in the RHS. The neuronal densities of L1, L2/3, L5A, L5B and L6 layers were respectively 1.6 ± 1.6, 73 ± 12, 108 ± 5, 84 ± 2 and 68 ± 2 in the LHS and 1.4 ± 0.9, 72 ± 4, 104 ± 3, 81 ± 3 and 63 ± 5 in the RHS (expressed as 1000 neurons per mm^3). G. Comparison of vM1 and vS1 reference frames. The average volume and number of neurons of the vM1 reference frame were nearly 4 times the average volume and number of neurons of vS1 reference frame as reported in (Meyer et al., 2013). The resulting densities of vM1 and vS1 reference frames were comparable to each other (75 ± 3 vs 80 ± 4 thousand neurons per mm^3).

density (75 ± 3 vs 80 ± 4 thousand neurons per mm^3), owing to the presence of the granular layer (layer 4).

Layer borders of the barrel cortex reference frame The aforementioned methods of obtaining the layer borders were subsequently applied for deriving layer borders of the barrel cortex reference frame. This was achieved by obtaining the neuronal density profiles of C2, C3, D2 and D3 barrel columns (assuming a barrel radius of 250 µm) of tangentially sliced Animal 2 (LHS) and Animal 3 (LHS and RHS). The layer borders were then derived from these density profiles using the same method that was applied for the layer border derivation of the vM1 reference frame. Figure 3.26 shows the average neuronal density profiles of each

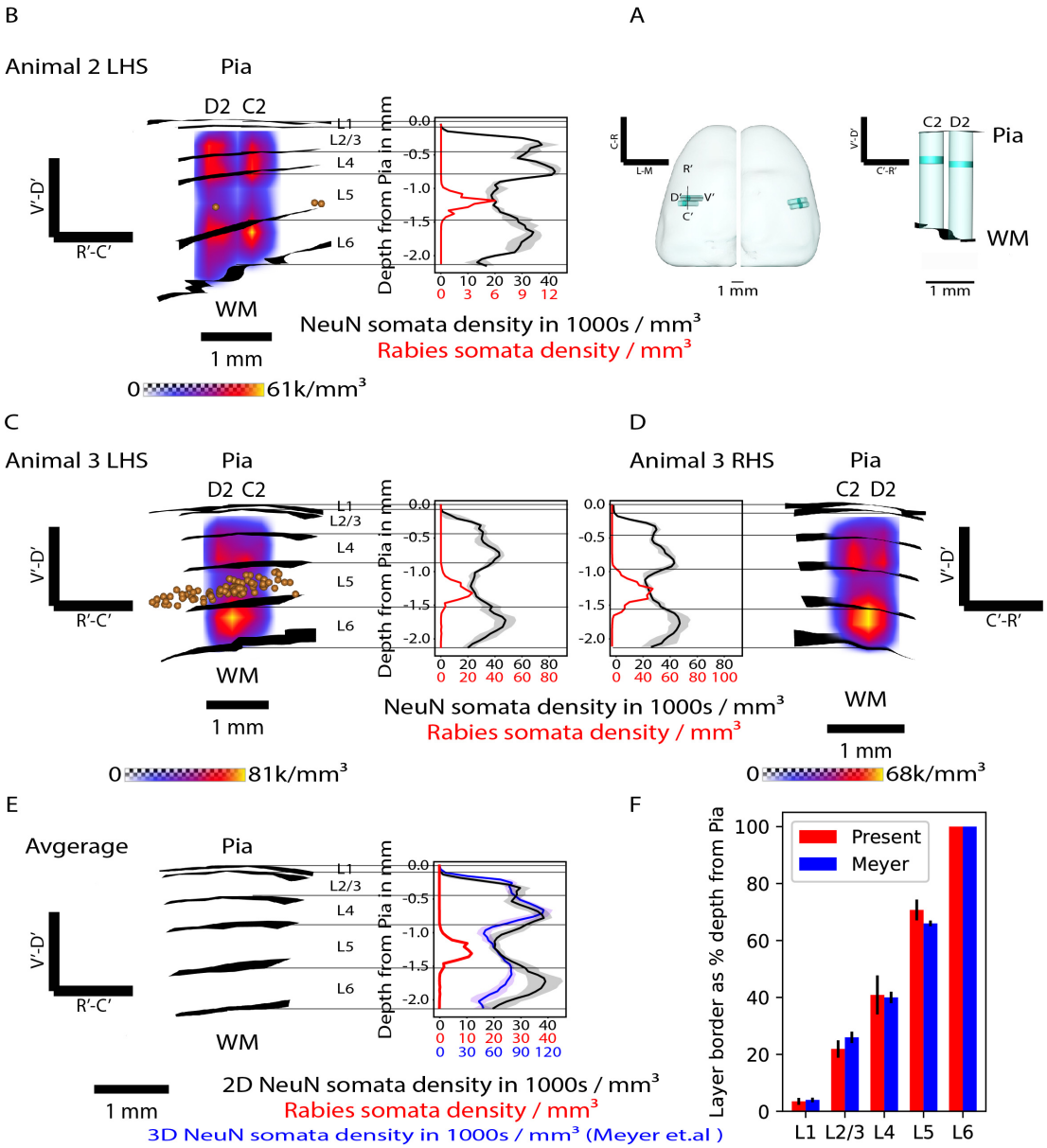

Figure 3.26. Layer borders of the barrel cortex reference frame. A. Left. Top view of the Pia surface of Animal 1 with C2 and D2 barrel columns of Animal 2 registered to it. Right. C2 and D2 barrel columns of the Animal 2 LHS, visualized in sagittal view of the D2 barrel column's local reference frame. B. Left. Heat map of neuronal density of C2 and D2 barrel columns of Animal 2 LHS. The density image volumes were generated using a grid resolution of 200 µm^3. The layer borders are visualized as iso-surfaces as well as horizontal lines. Right. Average (± SD) neuronal density profile of Animal 2 LHS averaged across C2, C3, D2 and D3 barrel columns; along with the average rabies density profile of the rabies defined vS1 reference frame of the Animal 2 LHS. Note different scales used for NeuN and

Figure 3.26. rabies density profiles. C-D. Same as panel B, but for Animal 3 LHS and RHS respectively. E. Left. Average layer border surfaces. Right. Average NeuN and rabies density profiles, averaged across the three reference frames. Additionally, average 3D neuronal density profile derived in (Meyer et al., 2010) is also shown for comparison. F. Comparison of layer borders derived in this thesis with (Meyer et al., 2010).

barrel cortex reference frame under consideration, along with the visualization of neuronal density of C2 and D2 barrel columns in the sagittal view of the D2 column's local reference frame. Additionally, the average layer border surfaces - averaged across the three barrel cortex reference frames - are also shown, along with the corresponding average (N = 12) neuronal density profile. The average lower borders thus defined for L1, L2/3, L4 and L5 layers were respectively 3% ± 1%, 22% ± 3%, 41% ± 7% and 71% ± 4% below the Pia surface, expressed as percentage of cortical thickness. These layer borders were comparable to those defined in the study (Meyer et al., 2010); which were 4% ± 1%, 26% ± 2%, 40% ± 2% and 66% ± 1% below the Pia surface respectively for L1, L2/3, L4 and L5 layers. The methods used for layer border derivation were similar between the two studies, with the difference being that in (Meyer et al., 2010) study, the cell counting was performed in 3D image stacks instead of 2D. The similar layer borders of barrel cortex reference frame obtained across these two studies validates the current method of layer border derivation presented in this thesis.

In addition to the NeuN density profiles of the barrel cortex, density profiles were generated for the rabies-positive neurons of rabies defined vS1 reference frames (see Figure 3.26). As in the case of vM1 reference frame, the rabies-positive neurons in the vS1 reference frame were restricted to the layer L5 (99% ± 1%), further confirming that the three rats under study were indeed third-order animals.

Comparison of the barrel cortex reference frame with the SBF During histology, the cortices of Animal 2 and Animal 3 were sliced tangentially and thus allowed for the reconstruction of their barrel cortices (N=4). In each barrel cortex, barrels were manually reconstructed from the 2D image stack using autofluorescence, resulting in the reconstruction of 4 arcs (1-4) each in A, B, C, D, E

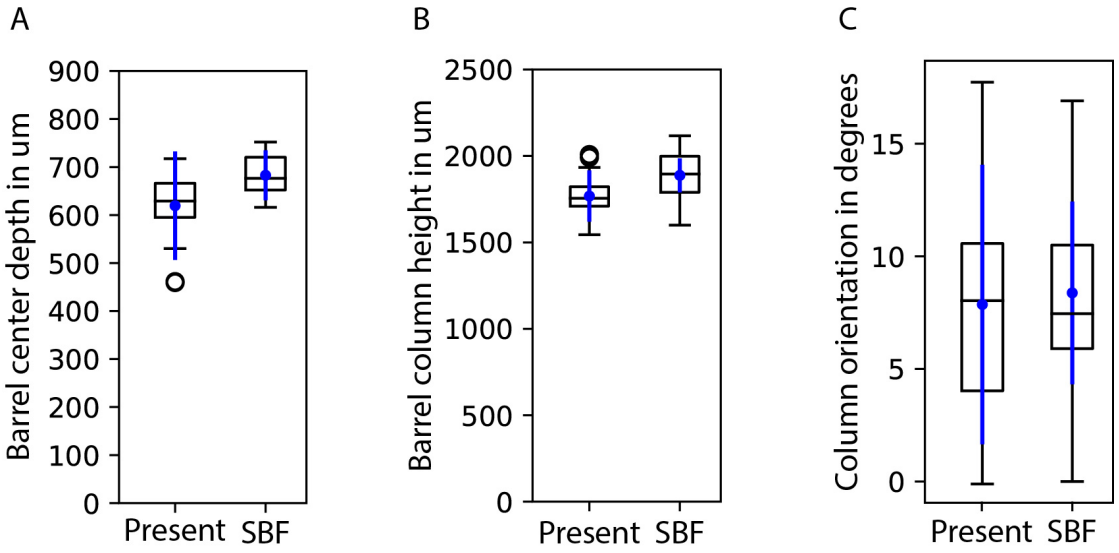

Figure 3.27. Comparison of the barrel cortex reference frame with the SBF. A. Comparison of depths of barrel centers from the Pia. The barrel centers of the barrels reconstructed in the current study were on average 617 µm ± 113 µm below the Pia; whereas, the barrel centers of the barrels reconstructed in the SBF study (R. Egger et al., 2012) were on average 683 µm ± 52 µm below the Pia. B. Comparison of heights of barrel columns. The barrel column heights on average were 1769 µm ± 148 µm and 1888 µm± 98 µm respectively for current and SBF studies. C. Comparison of orientations of the barrel columns. The average orientation of barrel columns with respect to the D2 barrel column in the current study were 8° ± 6.2°; whereas, in the SBF study, the barrel column orientations with respect to the C2 barrel column were on average 8.4°±4.1°.

and greek rows. Each of the 24 barrels thus reconstructed, was then approximated by a cylinder of 250 µm radius and the cylinder was projected to intersect the Pia and WM, forming the barrel column. In a previous study (R. Egger et al., 2012), the aforementioned 24 barrels were reconstructed across 12 barrel cortices using staining, high resolution imaging and automated image processing techniques that were optimized for precise reconstruction of barrel cortices. The average model from those barrel cortices was termed as the standard barrel field (SBF).

Figure 3.27 compares the barrel cortex reference frame (presented in this thesis) with the SBF (reported in (R. Egger et al., 2012)) with respect to the following parameters: depth of the barrel center from Pia, height of the barrel column and orientation of the barrel column. For each of these parameters, the Figure 3.27

shows the distribution of means of 24 barrels for the two studies (N=4 vs N=12). Additionally, the mean of means and the mean of SDs of 24 barrels are also shown as error bars. The barrel column orientations were measured with respect to the D2 and C2 reference columns respectively in the current and the SBF studies. The results were similar across the two studies (current vs (R. Egger et al., 2012)) with the average barrel center depth being 617 µm ± 113 µm vs 683 µm ± 52 µm, the average barrel column height being 1769 µm ± 148 µm vs 1888 µm± 98 µm and the average barrel column orientation being 8° ± 6.2° vs 8.4°±4.1°. However, the variability (as expressed by the mean SD) of the SBF was smaller compared to the barrel cortex reference frame of the current study; owing to the precise reconstruction of barrels in the former study.

3.3.4 The morphologies registered to the vM1 reference frame

Having described the geometry and the cellular organization of the vM1 reference frame in the previous subsections, in this subsection I delineate its morphological organization by presenting neuronal morphologies that have been registered to the vM1 reference frame. The method for registering morphologies has been described in 2.3.3. Using this method 3D morphologies of 90 neurons were registered to the vM1 reference frame (LHS). The locations of these registered neuronal somata as well as dendrites have been visualized in the vM1 reference frame's top view in Figure 3.28 A,B. In addition to the morphologies, the rabies-positive neuron somata of Animal 1-3 (1567) that have been registered to the vM1 reference frame are visualized as a density map (see 3.28 A). The density image volume was generated using a grid resolution (voxel size) of 400 μm^3. The iso-contours corresponding to different lower density thresholds were generated similar to those generated for the individual animals (see 3.14). As visualized in Figure 3.28 A and quantified in Figure 3.28 D, all 90 registered morphologies lied within the vM1 reference frame. 84% (76), 27% (24) and 7% (6) registered morphologies lied within 10%, 50% and 100% iso-contours respectively.

After surface to surface registration of the morphologies (step 1 of registration), the difference in soma depth from Pia (and height from WM) before and after reg-

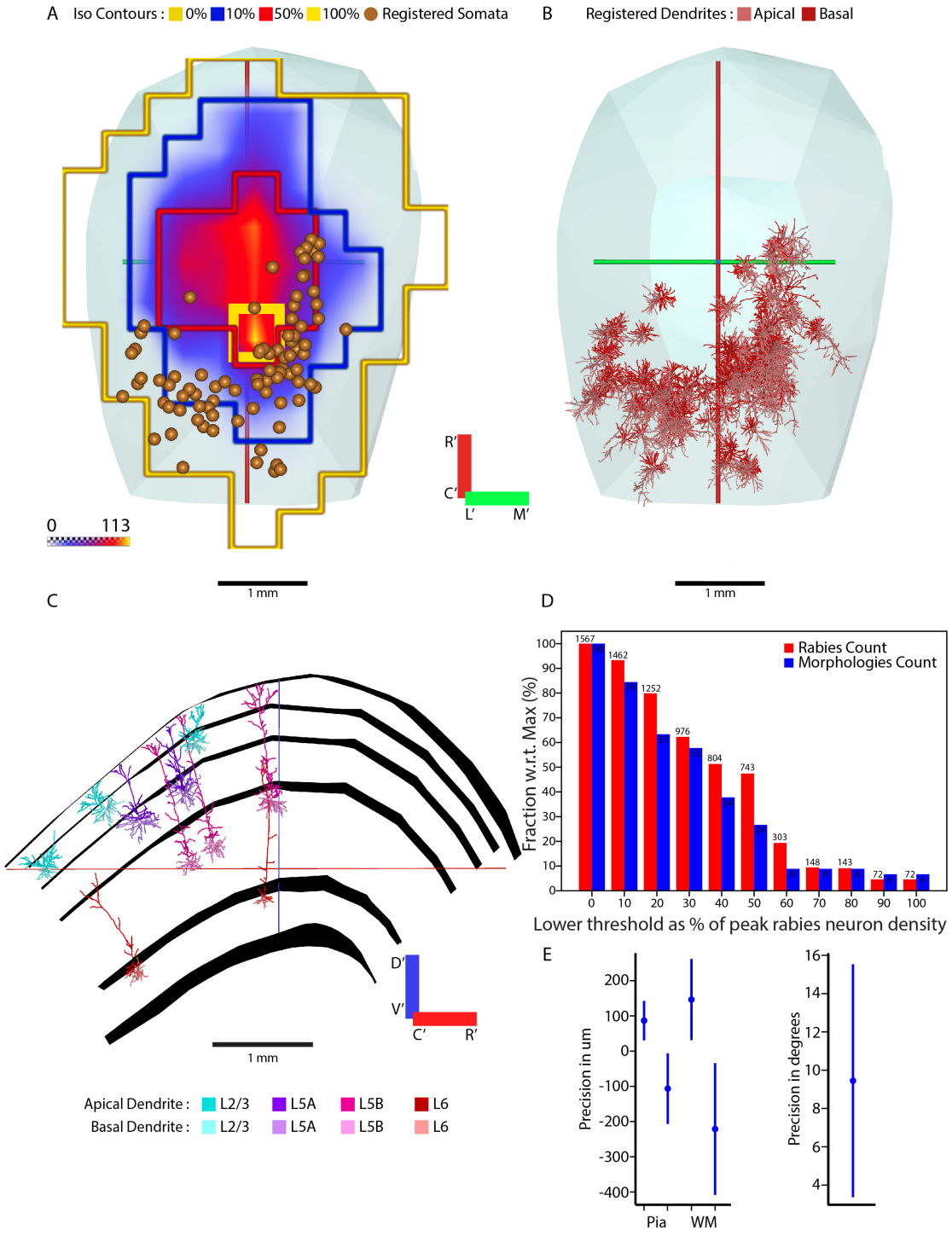

Figure 3.28. The morphologies registered to the vM1 reference frame. A. Top view of the vM1 reference frame (LHS). Somata of all registered morphologies are shown. Rabies-positive neuronal somata from Animal 1-3 that have been registered to the vM1 reference frame are shown as a density heat map. Iso-contours corresponding

Figure 3.28. to lower density thresholds of 0%, 10%, 50% and 100% of peak density are shown with color coding. Somata of all registered morphologies lie within the vM1 reference frame. 84% and 27% of registered somata respectively lie within 10% and 50% iso-contours. B. Top view of the vM1 reference frame showing dendrites of registered morphologies. C. Example dendrites of registered morphologies shown in the sagittal view of the reference frame. The layer border surfaces, clipped around the central axis, are also shown. D. Quantification of registered morphologies with respect to the density map of third-order rabies-positive neurons shown in panel A. E. Precision of surface-surface registration of morphologies. The difference between original and registered soma depths were 101 µm ± 91 µm and difference in heights were 199 µm ± 174 µm. The neuronal axes of registered neurons changed their orientation by 9.5° ± 6°.

istration were measured. Similarly, the difference in orientation of neuron axis was also measured. These quantities are plotted in Figure 3.28 E. For 23 morphologies, their soma depth decreased by 87 µm ± 56 µm, whereas their height decreased by 146 µm ± 115 µm. For remaining neurons, their soma depth and height increased by 107 µm ± 100 µm and 221 µm ± 187 µm respectively after registration. On average the precision of soma depth and height respectively were 101 µm ± 91 µm and 199 µm ± 174 µm. The difference in the orientation of neuron axis before and after the surface based registration were 9.5° ± 6°.

The registered morphologies were assigned to their respective layers based on the depth of their somata. The mean layer borders of the vM1 reference frame described in the previous subsection were used to determine the layer membership of the registered morphologies (except for L1 and L5B where mean - SD was used as the lower border). A few registered dendrites belonging to different layers are visualized in the sagittal view of the vM1 reference frame in Figure 3.28 C. Additionally, clipped layer border surfaces are also shown. Appendix A (see 4.5) shows the layer-wise galleries of registered dendritic morphologies, in the sagittal view of their local reference frame.

3.4 The Precisions of global and local reference frames

In the previous sections, I have presented local reference frames for three brain regions (anatomical landmarks), namely: barrel cortex, facial nucleus and vibrissal motor cortex. In this section, I will discuss the precisions of cortical local reference frames presented thus far by comparing them with the precisions obtained using global methods. Specifically, I quantify the precision of three anatomical landmarks: the cortical hemisphere, the vM1 reference frame and the barrel cortex reference frame. In order to do so, I utilize the left cortical hemispheres of three third-order rabies injected rats discussed in the previous section. Precision is given by the standard deviation of means; and is hence a measure of how close together (or far apart) are the centroids (means) of anatomical landmarks after alignment. Therefore, for each anatomical landmark, the precision is measured as the misalignment error of registering anatomical landmarks of different animals with each other. The precision and the misalignment error have an inverse relationship (lower the measured misalignment error higher the precision of alignment and vice versa). The euclidean precision is measured as the mean of 3D distances of individual landmark centers from the mean of those centers; and is quantified at the center, the Pia and the WM for each anatomical landmark. The angular precision for each landmark is measured at uniformly sampled locations through out the landmark and then averaged across those measurements. At any given location, the precision is measured as the mean of angles made by individual animal's orientations with their mean at that location. The procedures by which these precisions are quantified has been detailed in the methods section (see 2.3.1). The precision measurements are illustrated for the vM1 and the barrel cortex reference frames in Figure 3.29 A,B respectively.

The precisions are quantified following the alignment of landmarks using different alignment methods. In the global alignment method, landmarks are aligned by minimizing the surface error between cortical surfaces of the three rats. This global method is further refined by aligning landmarks using the centers of motor and sensory rabies clusters; and further by using the rabies cluster surfaces instead

of using the cortical surface. In addition to these global methods, landmarks are also aligned using the local reference frames. In the case of the vM1 reference frame, landmarks are aligned by minimizing the error between the surfaces of respective vM1 rabies clusters. In the case of the barrel cortex reference frame, the landmarks are aligned by minimizing the error between centers of respective barrels of individual rats. The procedures used for these alignments are described in the methods section (see 2.3.1).

The euclidean misalignment error (precisions) for different alignment types measured at the center, the Pia and the WM are quantified in the Figure 3.29 C-E; whereas the panel F shows the angular (orientational) precisions for the same. When the landmarks were aligned using the global alignment method, that is using the hemispheric surfaces, the average euclidean misalignment error (mean ± SD) - averaged across quantifications at the center, Pia and WM - of aligning cortical surfaces to each other was 344 µm ± 97 µm and the angular misalignment error was 10° ± 4°. During this global alignment, the error at the vM1 reference frame was 560 µm ± 204 µm (average euclidean) and 14° ± 6° (angular); whereas the error at the barrel cortex reference frame was 718 µm ± 130 µm and 15° ± 1°. When the centers of motor and sensory rabies clusters were used for aligning landmarks instead of cortical hemispheric surfaces, the misalignment errors at the vM1 and the barrel cortex reference frames reduced to 321 µm ± 112 µm (7° ± 4°) and 329 µm ± 60 µm (5° ± 1°) respectively; while the error at the hemispheric surface increased to 493 µm ± 199 µm (15° ± 5°). Furthermore, when the surface of the motor and sensory rabies cluster volume was used for aligning landmarks instead of the cluster centers, there was a further reduction in the misalignment errors with the vM1 and the barrel cortex reference frames having errors of 195 µm ± 63 µm (5° ± 2°) and 273 µm ± 56 µm (5° ± 0.4°) respectively; while the error at the hemispheric surface also reduced to 428 µm ± 171 µm (13° ± 4°).

When landmarks were aligned by aligning the vM1 reference frames with each other, best precision was obtained at the vM1 reference frames with error being 141 µm ± 42 µm (2° ± 1°). This also lead to the maximum alignment errors at barrel cortex reference frame (1036 µm ± 89 µm, 15° ± 2°) and hemispheric surface (661 µm ± 210 µm, 23° ± 9°). When landmarks were aligned by aligning the barrel cortex reference frames with each other, least error of 111 µm ± 61 µm (3° ± 0.3°)

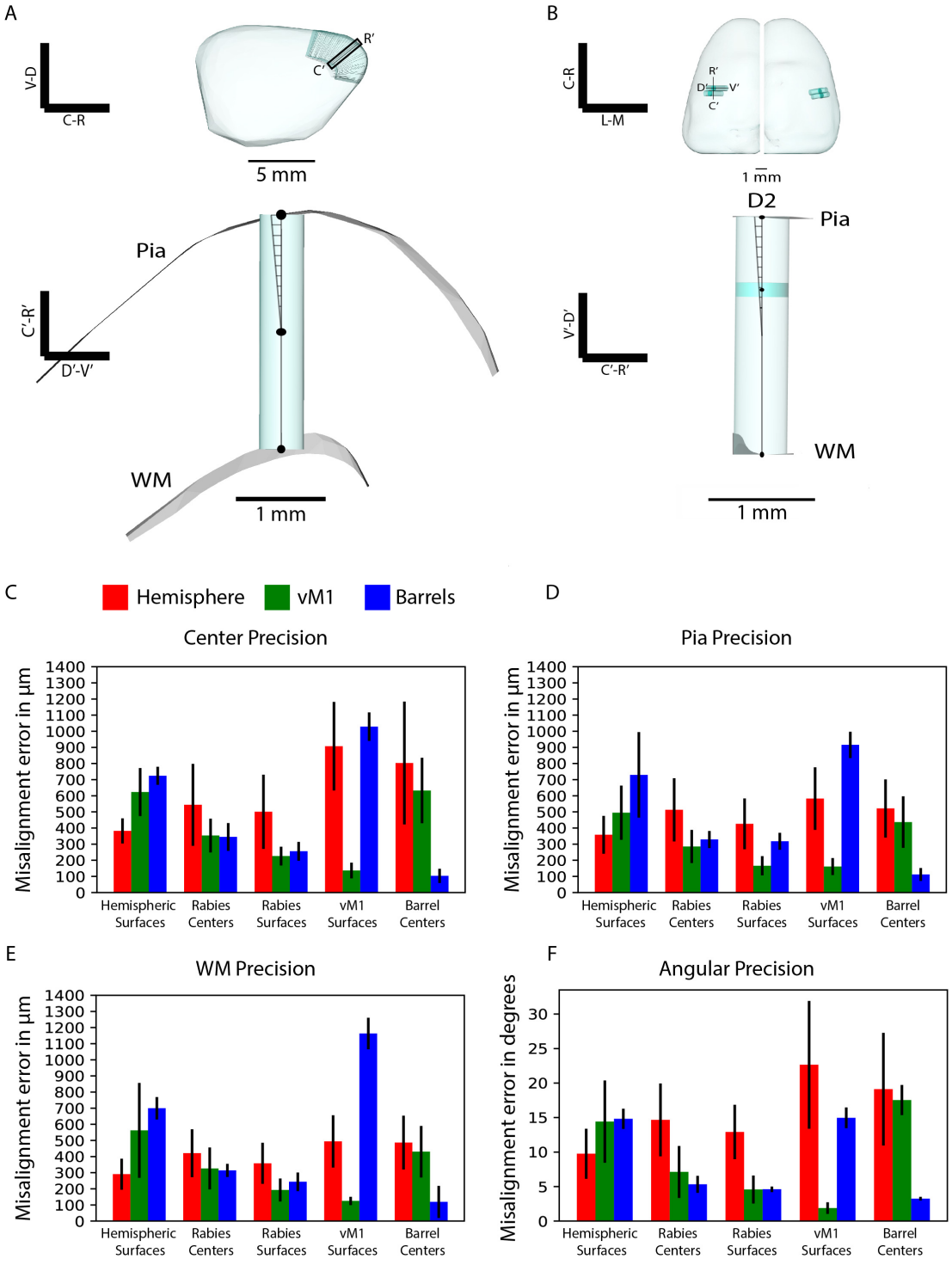

Figure 3.29. Comparing the precisions of global and local reference frames. A. Illustration of quantifying precision of vM1 reference frame. Top: Sagittal view of average left hemisphere (of three third-order animals) with standard vM1 reference

Figure 3.29. frame. The axis field of the vM1 reference frame is shown along with its central axis (highlighted). Bottom: Zoom-in of central axis of standard vM1 reference frame shown in side view of its local reference frame, where the central axis is visualized as a cylindrical column. Pia and WM surfaces are also shown. The precisions at the center of the axis, Pia and WM intersections of the central axis are shown as error ellipsoids. The angular precision is shown as the shaded area around the central axis. B. Illustration of quantifying precision of barrel cortex reference frame. Top: Top view of Pia surface of a coronally sliced rat cortex with registered C2 and D2 barrel columns shown. Bottom: Zoom-in of D2 barrel column of left hemisphere in its local reference frame. The precisions at the center of the D2 barrel, Pia and WM intersections of the barrel axis are shown as error ellipsoids. The angular precision is shown as the shaded area around the barrel axis. C-F. Quantification of precisions (mean ± SD) measured at the center, Pia and WM as well as angular precisions. Each precision is measured for three anatomical landmarks: cortical hemisphere, vM1 reference frame, barrel cortex reference frame (color coded as red, green and blue respectively). Precisions were evaluated when landmarks were aligned to each other by aligning the following: cortical hemisphere surfaces, centers of motor and sensory rabies clusters, surfaces of motor and sensory rabies clusters, vM1 rabies cluster surfaces and barrel centers. There is a six-fold improvement in the precision of vM1 and barrel cortex reference frames when landmarks were aligned using the respective local reference frames, as opposed to when landmarks were aligned using cortical hemispheres (global method).

was obtained at the barrel cortex reference frame; while high errors were seen at the hemispheric surface (604 µm ± 243 µm, 19° ± 8°) and the vM1 reference frame (500 µm ± 174 µm, 18° ± 2°).

In summary, there is a six-fold improvement in the precision (reduction in misalignment error) of aligning the brain region of interest when its local reference frame is used for alignment instead of the entire brain. Particularly, there was a four-fold improvement in the euclidean precision and seven-fold improvement in the angular precision (six-fold on average) of the vM1 reference frame when its local reference frame was used instead of global alignment. Similarly, seven-fold improvement in the euclidean precision and five-fold improvement in the angular precision (six-fold on average) of the barrel cortex reference frame was achieved when its local reference frame was used instead of global alignment.

4 | Discussion

In this thesis, I introduced the concept of local reference frames for precise neuroanatomical modeling of brain regions and its advantages over global reference frames in precisely modeling the geometric, cellular, morphological and synaptic organization of brain regions. I illustrated this with the example of the 3D local reference frame of the rat barrel cortex (SBF) that has been previously developed. As an application of the SBF, the dense statistical connectome model of the SBF and its connectivity predictions (between pairs of neurons) were introduced. In order to compare these predictions with the empirical data, I developed an algorithm for detecting putative synaptic contacts between *in vivo* labeled pairs of neurons and applied them to 45 pairs of 3D neuronal morphologies of the rat barrel cortex belonging to different cell types, which yielded 49 putative synapses. The number and distribution of the synaptic contacts thus obtained were in-line with the predictions made by the connectome model of the SBF, further underscoring the importance and validity of the 3D local reference frames. Therefore, I extended the 3D local reference framing approach to two more regions of the rat brain: the FN and the vM1.

I defined the FN using the size differential between the somata of the FN compared to the somata of neighboring neurons. For three rats, I approximated the geometry of the FN with an ellipsoid which covered 84% of the FN volume. The FN volumes varied by only 5% across animals. I generated an average (standard) 3D local reference frame of the rat FN which had a precision of 120 µm (euclidean) and 4.6° (angular). I applied the FN reference frame to delineate the cellular (specifically vMN) and morphological organization. FN had a neuron density of $6743\,\mathrm{mm}^{-3}$ on average and the vMNs were located in the ventro-lateral part of the

FN. Injection of mono-synaptic retrograde tracers into the intrinsic whisker muscles showed whisker specific labeling of vMNs. I registered 13 FN to the standard FN reference frame, along with labeled vMNs resulting from 36 whisker injections; which revealed whisker row-specific organization of vMNs in the rat FN. Hence, I generated standard row-specific vMN slabs. I registered the 3D morphologies of the vMN dendrites (N=3) to the FN reference frame, which revealed that on average 64% of dendrites remained within the FN and projected in the rostral and medial direction to their row-specific slabs.

Both in the case of SBF as well as the FN, the criteria used to define them were based on the salient anatomical features that distinguished them from their surrounding. For brain regions lacking such anatomical landmarks, an alternative way of defining the brain region is necessary. Here, I developed a novel approach to defining a brain region of interest: using its synaptic distance from a terminal muscle. In order to achieve this, I employed the retrograde trans-synaptic rabies virus tracing to detect the neuronal population that are a fixed synaptic distance away from the intrinsic whisker muscles. I applied the FN reference frame to validate the accurate targeting of the virus and quantified its subsequent progression. The first progression of the virus labeled exclusively vMN of the FN, which directly innervate the intrinsic whisker muscle. Second trans-synaptic progression labeled regions of the brain stem that were pre-synaptic to the FN. Third-order progression labeled neurons in the cortex exclusively in the layer 5. Fourth-order and beyond, the virus progression spread to other layers of the cortex.

I defined vM1 as the left hemispheric cortical region spanning the layer 5 rabies labeled neurons in the rostral region of the third-order animals. The vM1 volume thus defined was $30\,\mathrm{mm}^3 \pm 3\,\mathrm{mm}^3$ (N=3) and varied only 10% across animals; hence I generated an average reference frame which had a precision of 137 µm (euclidean) and 6° (angular). I counted the number of neurons contained within the vM1 and the LHS contained 2.4 ± 0.4 million neurons (CV=17%). I further derived the layer borders of the vM1 using neuronal density profiles, which had an average precision of 30 µm. I registered 90 3D neuronal morphologies to the vM1 reference frame, which had a precision of 101 µm (10°) in terms of the depth of their somata after surface based registration. Finally, I compared the precisions of global and local reference frames by aligning the anatomical landmarks using the cortical

hemispheric surface (global), the vM1 reference frame and the vS1 reference frame and measuring the precisions at the center of the reference anatomy, Pia surface and WM surface for each alignment method. Registration using local reference frames were on average six times more precise than using the global reference frame.

In the subsequent sections, I will discuss the implications of the work presented in this thesis with respect to other similar works along with their limitations and future directions.

4.1 Putative synapse detection between *in vivo* labeled neurons

In vitro electrophysiology is a popular method for investigating functional connectivity between neurons; wherein, pre-synaptic neurons are electrically stimulated and the electrical response of the post-synaptic neurons are measured to infer connectivity between neurons in acute tissues slices (Deuchars & Thomson, 1996; Schubert, Kötter, Luhmann, & Staiger, 2006; Frega, Tedesco, Massobrio, Pesce, & Martinoia, 2014; Qi, Radnikow, & Feldmeyer, 2015). However, this method is prone to be biased towards finding strongly connected neurons (in number and/or strength of synapses) in lieu of weakly connected ones. Additionally, the morphological identity of the neurons is not known, unless this method is used in combination with other staining methods for morphological reconstruction. Even then, the reconstruction (and hence the cell type identification) of the neurons is hampered by the potential loss of neuronal arbors due to slicing. The loss of arbors is more pronounced in axons, which has extensive arborization compared to the dendrites. The *in vivo* synapse detection method presented in this thesis overcomes these limitations as follows. First, the method is unbiased and detects even the weak synapses. Second, *in vivo* labeling in the live animal and the subsequent procedures ensure that the full 3D morphology of the neuron is reconstructed with all its dendritic and axonal arborization intact. Therefore, loss of the neuronal structures - and the possible loss of synaptic contacts as a result - are avoided. *In silico* simulations conducted by Dr. Udvary, where the *in vitro* slicing effects are

applied to the *in vivo* morphologies, showed that there can be a loss of 14% to 50% of putative synapses, depending on the cell type, due to the clipping of neural structures (Slabik, 2018).

In addition to the number of synapses, the current method provides the location of detected synapses along with the pre (axon) and post (dendrite) synaptic structures. Further, the morphological cell type identification of pre and post synaptic neurons, makes it possible to analyze the number and distribution of synapses between classes of neurons.

The limitation of the *in vivo* putative synapse detection method is that it provides the upper limit of actual number of synapses, not the actual number of synapses. In order to obtain real synapses, the putative synapses need to be inspected under an electron microscope (Peters, White, & Fairén, 1977; Peters & Proskauer, 1980). Correlated light and electron microscopy studies, where the putative synapses detected using light microscopy are verified using electron microscopy, can reveal real synapses eliminating the false positives (Muller-Reichert & Verkade, 2012; De Boer, Hoogenboom, & Giepmans, 2015). In a pervious such study 87.5% of putative synapses turned out to be real synapses (Schoonover et al., 2014). The current method can be augmented using synapse markers (such as Synapsin, Synaptophysin, VGlu) to further reduce false positives from the putative synapses (Thiel, 1993; Calhoun et al., 1996). A study showed that about 95% of VPM boutons identified in the vS1 were positive for a bouton marker (VGlu2) (R. Egger et al., 2020).

Even though, the putative synapses need to be further inspected to obtain actual synapses, the current method systematically reduces the number of potential locations to be inspected (under an electron microscope) by several (6-7) orders of magnitude - from tens of millions of potential locations to thousands of proximity zones to tens of touch points to less than ten putative contacts per cell pair. Thus, saving the time and effort required for obtaining unbiased, cell type specific synapses between *in vivo* labeled pairs of neurons.

4.2 Organization of vMNs within the rat FN

Mono-synaptic tracers (CTB) injected into the intrinsic whisker muscle labeled vMNs in the FN. I registered FN of 18 rats, containing labeled vMNs resulting from a total of 36 tracer injections, into the FN reference frame. All registered vMNs occupied the ventro-lateral region of the FN reference frame and formed whisker row-specific slabs along the R-C extent of the FN. Both these observations are consistent with the findings of previous anatomical (Klein & Rhoades, 1985) and functional studies (Herfst & Brecht, 2008) of the FN. Furthermore, we estimated that each intrinsic whisker muscle is represented by 58 ± 6 vMNs, which is within the range of 50-100 vMNs per intrinsic whisker muscle previously reported (Klein & Rhoades, 1985).

The trans-synaptic rabies virus injected into the intrinsic muscle of the C3 whisker consistently labeled a handful of vMNs within the C-row slab of the FN reference frame. As the virus progressed (labeling neuronal populations that are upstream from the vMNs), there were no new vMNs labeled within the ventro-lateral part of the FN. This lack of local synaptic connectivity within the ventro-lateral FN observed here is consistent with a previous study (Herfst & Brecht, 2008) that has shown that the vMNs innervating the intrinsic whisker muscle do not send axonal projections collaterally. However, this observation did not extend to the entire FN, as the third and fourth order animals showed additional labeling outside the ventro-lateral part of the FN.

The sparse labeling of the vMNs by the rabies virus allowed reconstruction of its dendrite morphologies. The registered dendrites of the vMNs show large variability in terms of the row specific slabs they overlap with, as well as the location at which they terminate, even though they innervate the same intrinsic whisker muscle (C3 whisker). This specificity of the vMNs suggests that these vMNs receive inputs from different pre-synaptic populations in the brain stem, depending on which starter vMNs were labeled at first order; which in turn may result from the specific muscle fibers targeted during the virus injection. This is borne out by the large variability observed in the labeling of pre-synaptic populations upstream from the vMNs across the second-order animals. The pre-synaptic nuclei reported here are largely in-line with the previous reports (Takatoh et al.,

2013; Sreenivasan et al., 2015). These variabilities in the dendrite morphologies and their pre-synaptic populations together suggest that the vMNs integrate different synaptic inputs, even when innervating the same intrinsic whisker muscle. This structural observation is supported by the functional observation reported by (Herfst & Brecht, 2008), where each vMN evoked a cell-specific whisker movement.

4.3 The rabies defined vM1 reference frame

The replication-competent rabies virus has been previously employed as a retrograde trans-synaptic tool to trace the poly-synaptic hierarchical network of neurons that are involved in motor control (Kelly & Strick, 2000, 2003; Klingen et al., 2008; Ugolini, 1995, 2010, 2008; Tang et al., 1999). In the work presented in this thesis, the rabies virus has been injected into the intrinsic whisker muscle of rats to trace the motor control neural network that terminate at this single muscle; followed by a detailed quantitative analysis of the spread of the virus. This is a novel application of the rabies virus as a network tracing tool. Additionally, the rabies infected dendrites of the vMNs have been reconstructed in 3D, which is also a first. Since the initial uptake of the virus across the neuromuscular junction is variable across animals, the animals are classified based on the synaptic distance that the virus has progressed from the terminal muscle, instead of using just the survival time of the animals. This allowed accurately identifying the synaptic order of spread of the virus in each infected animal. The animals which showed labeling only in the layer 5 of their cortex (no labeling anywhere else in the cortex), were defined as third order animals. I used the rabies labeled layer 5 neurons in the motor cortex to define the vM1 region. Using the rabies virus for defining a brain region is, to the best of my knowledge, a novel application of the tool. Furthermore, defining a functional brain region based on its synaptic distance (three synapses in this case) from a terminal point, is a novel way of identifying and defining a brain region; and a unique contribution of this thesis. This is specifically useful while defining regions where no anatomical landmarks exist that clearly demarcate the region of interest. A limitation of the trans-synaptic rabies tracing tool is that when there are multiple pre-synaptic populations labeled that are upstream from a specific region, we might need prior knowledge and/or further experiments (perhaps using

mono-synaptic tracers) to disentangle the order of synaptic spread of the virus amongst these pre-synaptic regions.

Amongst the cortical regions labeled by the rabies in the third-order animals, the volume labeled in the LHS of motor cortex region was most consistent across animals, having a variability (CV) of 10%. This region overlapped with the M1 and M2 regions when compared with the Paxinos rat brain atlas (Paxinos & Watson, 2006). Thus, I defined this as the vM1 and generated its local reference frame which had a precision of 137 µm (euclidean) and 6° (angular). This reference frame was then applied to obtain the cellular and laminar organization of the vM1, which were also consistent across animals. The layer borders on average varied by 30 µm and the number of neurons contained within the vM1 varied by 17% (CV). The 2D cell counts of the vM1 were first used to obtain the neuronal density profile, which were then used to derive the layer borders. These borders were in-line with the borders reported before (Hooks et al., 2011). Following this, the 2D cell counts were scaled in a layer-specific manner to obtain the 3D cell counts of the vM1 region, instead of using a single scaling factor across all layers. The 90 morphologies that were registered to the vM1 were sampled across all layers and they resembled the morphologies of the SBF. These morphologies were classified based on their registered cortical depth and visualized in layer specific galleries (see "Appendix A"). Future analysis can yield the classification of these morphologies based on their axo-dendritic features and allow a thorough comparison with their SBF counterparts. This would also shed light on the degree to which the canonical cell typing can be generalized across the sensory and motor cortices.

4.4 Precise modeling of brain regions using the local reference frames

In this thesis, I have presented one previously developed and two new local reference frames: SBF, FN and vM1. These brain regions were observed to be well preserved across animals, varying by 11.5%, 5.5% and 10% respectively. Number of neurons contained within these regions were also consistent across animals varying by 7%, 17% and 17% respectively. For the FN and the vM1 the cell counts

were estimated from 2D counts, which might have resulted in increased variability compared to the SBF, where neurons were counted in 3D. The geometric precisions of registering new anatomical data into these reference frames were ∼90 µm (∼±45 µm), ∼120 µm (∼±60 µm) and ∼140 µm (∼±70 µm) respectively; whereas the orientational (angular) precisions were 4.5°, 5° and 6° respectively. For the two cortical regions the SBF and the vM1, the variability of the laminar organization was 50 µm and 30 µm respectively. Going from the SBF to the vM1 reference frame, the volume increased by a factor of ∼5 and the precision worsened by a factor of ∼1.5. Continuing with the same logic, the volume of the cortical hemisphere (175 mm^3, (Mengler et al., 2014)) is ∼27 times that of the SBF, which could result in a precision that is 8 times worse than the precision of the SBF. I experimentally tested this intuition by registering anatomical data using the barrel cortex (vS1), the vM1 and the cortical hemisphere as reference anatomical landmarks. The precision obtained when using cortical hemisphere for registration was on average ∼6 times worse when compared with registration using local landmarks (vS1 and vM1). This underscores the importance of 3D local reference frames when precise modeling of geometric, cellular, morphological and synaptic organization of a specific brain region is required.

4.5 Summary and outlook

A brief summary of the work presented in this thesis are as follows. I first developed an algorithm to detect putative synaptic contacts between *in vivo* labeled neurons, whose morphological cell types are known. This tool reduces the time and effort required to detect putative synapses by several orders of magnitude compared to other methods. The number and distribution of putative synapses found using this tool were in-line with the connectivity predictions made by the dense statistical connectome model of the rat barrel cortex (SBF). This further verified and underscored the utility of the local reference framing approach and I proceeded to extend this approach to the rat facial nucleus (FN). The precise model of the FN (120 µm), allowed modeling of the row-specific organization of the vMNs that innervate intrinsic whisker muscles as well as their dendritic organization. I applied the FN reference frame to validate a technique for tracing the

poly-synaptic motor control networks that terminate at a single intrinsic whisker muscle using the trans-synaptic rabies virus. The time-dependent retrograde progression of the virus allowed defining the infected animals as: first-order (where the virus is restricted to the vMNs), second (where additionally pre-synaptic populations of the vMNs were labeled), third-order (where the virus has spread to layer 5 of the cortex) and fourth-order and beyond (where the virus has spread to other layers of the cortex). Inspired by this rabies tracing tool, I came up with a novel criteria for defining a functional brain region, based on its synaptic distance from a terminal muscle, so that local reference framing approach can be extended to regions without salient anatomical landmarks that help define them. Using this criteria, I defined vibrissal motor cortex (vM1) as the region containing neurons that are three synapses upstream from the terminal muscle. I identified vM1 as the region spanned by the third-order rabies labeled neurons in the motor (rostral) region of the cortex. I generated a precise model of the vM1 (140 µm) and applied it to model the cellular, laminar and morphological organization of the reference frame. With the help of the third-order cortical hemisphere, where the barrel (vS1) and motor (vM1) cortices were identified, I elucidated that the local reference frames (vS1 and vM1) provide at least six times more precision while modeling brain regions as compared to global reference framing approaches.

The local reference framing approach presented here can be extended to other suitable brain regions, whenever their precise geometric, cellular, morphological and synaptic modeling is required. Furthermore, the dense statistical connectome models can also be developed for desired brain regions following the blueprint of the SBF reference frame.

References

Ahrens, M. B., Li, J. M., Orger, M. B., Robson, D. N., Schier, A. F., Engert, F., & Portugues, R. (2012). Brain-wide neuronal dynamics during motor adaptation in zebrafish. *Nature*, *485*(7399), 471–477.

Ankerst, M., Breunig, M. M., Kriegel, H.-P., & Sander, J. (1999). Optics: Ordering points to identify the clustering structure. *ACM Sigmod record*, *28*(2), 49–60.

Benskey, M., & Manfredsson, F. (2016, 01). Intraparenchymal stereotaxic delivery of raav and special considerations in vector handling. In (Vol. 1382, p. 199-215). doi: 10.1007/978-1-4939-3271-9_14

Berg, R. W., & Kleinfeld, D. (2003). Vibrissa movement elicited by rhythmic electrical microstimulation to motor cortex in the aroused rat mimics exploratory whisking. *Journal of neurophysiology*, *90*(5), 2950–2963.

Besl, P., & McKay, N. (1992). *A method for registration of 3-d shapes, ieee t. pattern anal., 14, 239–256.*

Bowyer, A. (1981, 01). Computing Dirichlet tessellations*. *The Computer Journal*, *24*(2), 162-166. Retrieved from https://doi.org/10.1093/comjnl/24.2.162 doi: 10.1093/comjnl/24.2.162

Bruno, R. M., Hahn, T. T., Wallace, D. J., de Kock, C. P., & Sakmann, B. (2009). Sensory experience alters specific branches of individual corticocortical axons during development. *Journal of Neuroscience*, *29*(10), 3172–3181.

Calhoun, M. E., Jucker, M., Martin, L. J., Thinakaran, G., Price, D. L., & Mouton, P. R. (1996). Comparative evaluation of synaptophysin-based methods for quantification of synapses. *Journal of neurocytology*, *25*, 821–828.

Coulon, P., Derbin, C., Kucera, P., Lafay, F., Prehaud, C., & Flamand, A. (1989).

Invasion of the peripheral nervous systems of adult mice by the cvs strain of rabies virus and its avirulent derivative avo1. *Journal of virology*, *63*(8), 3550–3554.

De Boer, P., Hoogenboom, J. P., & Giepmans, B. N. (2015). Correlated light and electron microscopy: ultrastructure lights up! *Nature methods*, *12*(6), 503–513.

De Kock, C., Bruno, R. M., Spors, H., & Sakmann, B. (2007). Layer-and cell-type-specific suprathreshold stimulus representation in rat primary somatosensory cortex. *The Journal of physiology*, *581*(1), 139–154.

Dercksen, V. J., Hege, H.-C., & Oberlaender, M. (2014). The filament editor: an interactive software environment for visualization, proof-editing and analysis of 3d neuron morphology. *Neuroinformatics*, *12*(2), 325–339.

Deuchars, J., & Thomson, A. (1996). Ca1 pyramid-pyramid connections in rat hippocampus in vitro: dual intracellular recordings with biocytin filling. *Neuroscience*, *74*(4), 1009–1018.

Dum, R. P., Levinthal, D. J., & Strick, P. L. (2016). Motor, cognitive, and affective areas of the cerebral cortex influence the adrenal medulla. *Proceedings of the National Academy of Sciences*, *113*(35), 9922–9927.

Egger, R., Dercksen, V. J., Udvary, D., Hege, H.-C., & Oberlaender, M. (2014). Generation of dense statistical connectomes from sparse morphological data. *Frontiers in neuroanatomy*, *8*, 129.

Egger, R., Narayanan, R. T., Guest, J. M., Bast, A., Udvary, D., Messore, L. F., ... Oberlaender, M. (2020). Cortical output is gated by horizontally projecting neurons in the deep layers. *Neuron*, *105*(1), 122–137.

Egger, R., Narayanan, R. T., Helmstaedter, M., de Kock, C. P., & Oberlaender, M. (2012). 3d reconstruction and standardization of the rat vibrissal cortex for precise registration of single neuron morphology. *PLoS computational biology*, *8*(12), e1002837.

Egger, V., Nevian, T., & Bruno, R. M. (2008). Subcolumnar dendritic and axonal organization of spiny stellate and star pyramid neurons within a barrel in rat somatosensory cortex. *Cerebral cortex*, *18*(4), 876–889.

Feldmeyer, D., Brecht, M., Helmchen, F., Petersen, C. C., Poulet, J. F., Staiger, J. F., ... Schwarz, C. (2013). Barrel cortex function. *Progress in neurobiol-*

ogy, *103*, 3–27.

Ferrara, M., Lugano, G., Sandinha, M. T., Kearns, V. R., Geraghty, B., & Steel, D. H. (2021). Biomechanical properties of retina and choroid: a comprehensive review of techniques and translational relevance. *Eye*, *35*(7), 1818–1832.

for Brain Science (2004). Allen Mouse Brain Atlas [dataset]. Available from mouse.brain-map.org.Allen Institute for Brain Science (2011). Allen Reference Atlas – Mouse Brain [brain atlas]. Available from atlas.brain map.org., A. I. (2011). Allen institute for brain science. *Allen Institute for Brain Science*.

Frega, M., Tedesco, M., Massobrio, P., Pesce, M., & Martinoia, S. (2014). Network dynamics of 3d engineered neuronal cultures: a new experimental model for in-vitro electrophysiology. *Scientific reports*, *4*(1), 5489.

Guest, J. M., Seetharama, M. M., Wendel, E. S., Strick, P. L., & Oberlaender, M. (2017). 3d reconstruction and standardization of the rat facial nucleus for precise mapping of vibrissal motor networks. *Neuroscience*, *368*, 171–186.

Harms, M. P., Wang, L., Csernansky, J. G., & Barch, D. M. (2013). Structure–function relationship of working memory activity with hippocampal and prefrontal cortex volumes. *Brain Structure and Function*, *218*, 173–186.

Hattox, A. M., Priest, C. A., & Keller, A. (2002). Functional circuitry involved in the regulation of whisker movements. *Journal of Comparative Neurology*, *442*(3), 266–276.

Hawrylycz, M., Ng, L., Feng, D., Sunkin, S., Szafer, A., & Dang, C. (2014). The allen brain atlas. *Springer Handbook of Bio-/Neuroinformatics*, 1111–1126.

Herfst, L. J., & Brecht, M. (2008). Whisker movements evoked by stimulation of single motor neurons in the facial nucleus of the rat. *Journal of neurophysiology*, *99*(6), 2821–2832.

Honey, C. J., Kötter, R., Breakspear, M., & Sporns, O. (2007). Network structure of cerebral cortex shapes functional connectivity on multiple time scales. *Proceedings of the National Academy of Sciences*, *104*(24), 10240–10245.

Hooks, B., Hires, S. A., Zhang, Y.-X., Huber, D., Petreanu, L., Svoboda, K., & Shepherd, G. M. (2011). Laminar analysis of excitatory local circuits in vibrissal motor and sensory cortical areas. *PLoS biology*, *9*(1), e1000572.

Hubel, D. H., & Wiesel, T. N. (1959). Receptive fields of single neurones in the

cat's striate cortex. *The Journal of physiology*, *148*(3), 574.

Jackson, A. C. (2002). Rabies pathogenesis. *Journal of neurovirology*, *8*(4), 267–269.

Johnson, H. J., McCormick, M. M., & Ibanez, L. (2015). Template:the itk software guide book 1: Introduction and development guidelines-volume 1 [Computer software manual]. Kitware, Inc.

Julien, J.-F., Samama, P., & Mallet, J. (1990). Rat brain glutamic acid decarboxylase sequence deduced from a cloned cdna. *Journal of neurochemistry*, *54*(2), 703–705.

Kaufman, D. L., McGinnis, J. F., Krieger, N. R., & Tobin, A. J. (1986). Brain glutamate decarboxylase cloned in λgt-11: fusion protein produces γ-aminobutyric acid. *Science*, *232*(4754), 1138–1140.

Kelly, R. M., & Strick, P. L. (2000). Rabies as a transneuronal tracer of circuits in the central nervous system. *Journal of neuroscience methods*, *103*(1), 63–71.

Kelly, R. M., & Strick, P. L. (2003). Cerebellar loops with motor cortex and prefrontal cortex of a nonhuman primate. *Journal of neuroscience*, *23*(23), 8432–8444.

Khalsa, S., Mayhew, S. D., Chechlacz, M., Bagary, M., & Bagshaw, A. P. (2014). The structural and functional connectivity of the posterior cingulate cortex: Comparison between deterministic and probabilistic tractography for the investigation of structure–function relationships. *Neuroimage*, *102*, 118–127.

Klein, B. G., & Rhoades, R. W. (1985). Representation of whisker follicle intrinsic musculature in the facial motor nucleus of the rat. *Journal of Comparative Neurology*, *232*(1), 55–69.

Klingen, Y., Conzelmann, K.-K., & Finke, S. (2008). Double-labeled rabies virus: live tracking of enveloped virus transport. *Journal of virology*, *82*(1), 237–245.

Kobayashi, Y., Kaufman, D. L., & Tobin, A. J. (1987). Glutamic acid decarboxylase cdna: nucleotide sequence encoding an enzymatically active fusion protein. *Journal of Neuroscience*, *7*(9), 2768–2772.

Levinthal, D. J., & Strick, P. L. (2012). The motor cortex communicates with the kidney. *Journal of Neuroscience*, *32*(19), 6726–6731.

Logothetis, N. K. (1999). Vision: a window on consciousness. *Scientific American*,

281(5), 68–75.

Lorensen, W. E., & Cline, H. E. (1987). Marching cubes: A high resolution 3d surface construction algorithm. *ACM siggraph computer graphics*, *21*(4), 163–169.

MacQueen, J. (1967). Classification and analysis of multivariate observations. In *5th berkeley symp. math. statist. probability* (pp. 281–297).

Marsden, M. (1974). Cubic spline interpolation of continuous functions. *Journal of Approximation Theory*, *10*(2), 103-111. Retrieved from https://www.sciencedirect.com/science/article/pii/0021904574901099 doi: https://doi.org/10.1016/0021-9045(74)90109-9

Mengler, L., Khmelinskii, A., Diedenhofen, M., Po, C., Staring, M., Lelieveldt, B. P., & Hoehn, M. (2014). Brain maturation of the adolescent rat cortex and striatum: changes in volume and myelination. *Neuroimage*, *84*, 35–44.

Meyer, H. S., Egger, R., Guest, J. M., Foerster, R., Reissl, S., & Oberlaender, M. (2013). Cellular organization of cortical barrel columns is whisker-specific. *Proceedings of the National Academy of Sciences*, *110*(47), 19113-19118. Retrieved from https://www.pnas.org/doi/abs/10.1073/pnas.1312691110 doi: 10.1073/pnas.1312691110

Meyer, H. S., Schwarz, D., Wimmer, V. C., Schmitt, A. C., Kerr, J. N., Sakmann, B., & Helmstaedter, M. (2011). Inhibitory interneurons in a cortical column form hot zones of inhibition in layers 2 and 5a. *Proceedings of the National Academy of Sciences*, *108*(40), 16807–16812.

Meyer, H. S., Wimmer, V. C., Hemberger, M., Bruno, R. M., de Kock, C. P., Frick, A., ... Helmstaedter, M. (2010). Cell type–specific thalamic innervation in a column of rat vibrissal cortex. *Cerebral cortex*, *20*(10), 2287–2303.

Mountcastle, V. B. (1957). Modality and topographic properties of single neurons of cat's somatic sensory cortex. *Journal of neurophysiology*, *20*(4), 408–434.

Mullen, R. J., Buck, C. R., & Smith, A. M. (1992). Neun, a neuronal specific nuclear protein in vertebratesxs. *Development*, *116*(1), 201–211.

Muller-Reichert, T., & Verkade, P. (2012). *Correlative light and electron microscopy*. Academic Press.

Mysore Seetharama, M. (2015). *Automatic detection of boutons in in-vivo labeled neurons* (master thesis). Hochschule Ostwestfalen-Lippe University of

Applied Sciences, Lemgo.

Narayanan, R. T., Egger, R., Johnson, A. S., Mansvelder, H. D., Sakmann, B., De Kock, C. P., & Oberlaender, M. (2015). Beyond columnar organization: cell type-and target layer-specific principles of horizontal axon projection patterns in rat vibrissal cortex. *Cerebral cortex*, *25*(11), 4450–4468.

Narayanan, R. T., Mohan, H., Broersen, R., de Haan, R., Pieneman, A. W., & de Kock, C. P. (2014). Juxtasomal biocytin labeling to study the structure-function relationship of individual cortical neurons. *JoVE (Journal of Visualized Experiments)*(84), e51359.

Oberlaender, M., Boudewijns, Z. S., Kleele, T., Mansvelder, H. D., Sakmann, B., & de Kock, C. P. (2011). Three-dimensional axon morphologies of individual layer 5 neurons indicate cell type-specific intracortical pathways for whisker motion and touch. *Proceedings of the national academy of sciences*, *108*(10), 4188–4193.

Oberlaender, M., Broser, P., Sakmann, B., & Hippler, S. (2009). Shack-hartmann wave front measurements in cortical tissue for deconvolution of large three-dimensional mosaic transmitted light brightfield micrographs. *Journal of Microscopy*, *233*(2), 275–289.

Oberlaender, M., Bruno, R. M., Sakmann, B. J., & Broser, P. J. (2007). Transmitted light brightfield mosaic microscopy for three-dimensional tracing of single neuron morphology. *Journal of biomedical optics*, *12*(6), 064029.

Oberlaender, M., de Kock, C. P., Bruno, R. M., Ramirez, A., Meyer, H. S., Dercksen, V. J., ... Sakmann, B. (2012). Cell type–specific three-dimensional structure of thalamocortical circuits in a column of rat vibrissal cortex. *Cerebral cortex*, *22*(10), 2375–2391.

Oberlaender, M., Dercksen, V. J., Egger, R., Gensel, M., Sakmann, B., & Hege, H.-C. (2009). Automated three-dimensional detection and counting of neuron somata. *Journal of neuroscience methods*, *180*(1), 147–160.

Park, H. P. (2018). *Rabies-virus-based mapping of whisker-muscle-related cortical areas* (master thesis). Center of Advanced European Studies and Research (CAESAR), Germany.

Paxinos, G., & Watson, C. (2006). *The rat brain in stereotaxic coordinates: hard cover edition*. Elsevier.

Perich, M. G., & Rajan, K. (2020). Rethinking brain-wide interactions through multi-region 'network of networks' models. *Current opinion in neurobiology*, *65*, 146–151.

Peters, A., & Proskauer, C. C. (1980). Synaptic relationships between a multipolar stellate cell and a pyramidal neuron in the rat visual cortex. a combined golgi-electron microscope study. *Journal of neurocytology*, *9*, 163–183.

Peters, A., White, E. L., & Fairén, A. (1977). Synapses between identified neuronal elements. an electron microscopic demonstration of degenerating axon terminals synapsing with golgi impregnated neurons. *Neuroscience Letters*, *6*(2-3), 171–175.

Petersen, C. C. (2007). The functional organization of the barrel cortex. *Neuron*, *56*(2), 339–355.

Pinault, D. (1996). A novel single-cell staining procedure performed in vivo under electrophysiological control: morpho-functional features of juxtacellularly labeled thalamic cells and other central neurons with biocytin or neurobiotin. *Journal of neuroscience methods*, *65*(2), 113–136.

Qi, G., Radnikow, G., & Feldmeyer, D. (2015). Electrophysiological and morphological characterization of neuronal microcircuits in acute brain slices using paired patch-clamp recordings. *JoVE (Journal of Visualized Experiments)*(95), e52358.

Schoonover, C. E., Tapia, J.-C., Schilling, V. C., Wimmer, V., Blazeski, R., Zhang, W., ... Bruno, R. M. (2014). Comparative strength and dendritic organization of thalamocortical and corticocortical synapses onto excitatory layer 4 neurons. *Journal of Neuroscience*, *34*(20), 6746–6758.

Schroeder, W., Martin, K., Lorensen, B., & Kitware, I. (2006). *The visualization toolkit: An object-oriented approach to 3d graphics*. Kitware. Retrieved from https://books.google.de/books?id=rx4vPwAACAAJ

Schubert, D., Kötter, R., Luhmann, H., & Staiger, J. (2006). Morphology, electrophysiology and functional input connectivity of pyramidal neurons characterizes a genuine layer va in the primary somatosensory cortex. *Cerebral cortex*, *16*(2), 223–236.

Shenoy, K. V., & Kao, J. C. (2021). Measurement, manipulation and modeling of brain-wide neural population dynamics. *Nature communications*, *12*(1),

633.

Slabik, D. A. (2018). *Putative synaptische verbindungen zwischen kortikalen nervenzellen in vivo* (phdthesis). Eberhard-Karls-Universität Tübingen, Germany.

Smyth, A. (2015). *Automated detection of putative synaptic contacts between pairs of in vivo labeled neurons* (bachelor thesis). Eberhard-Karls University Tübingen, University of Stuttgart.

Sreenivasan, V., Karmakar, K., Rijli, F. M., & Petersen, C. C. (2015). Parallel pathways from motor and somatosensory cortex for controlling whisker movements in mice. *European Journal of Neuroscience*, *41*(3), 354–367.

Stalling, D., Westerhoff, M., & Hege, H. (2005). Amira-an object oriented system for visual data analysis. *Visualization Handbook, Academic Press, CR Johnson and CD Hansen, Eds.*

Stanford, L., & Sherman, S. M. (1984). Structure/function relationships of retinal ganglion cells in the cat. *Brain research*, *297*(2), 381–386.

Swanson, L. (2004). *Brain maps: structure of the rat brain.* Gulf Professional Publishing.

Takatoh, J., Nelson, A., Zhou, X., Bolton, M. M., Ehlers, M. D., Arenkiel, B. R., ... Wang, F. (2013). New modules are added to vibrissal premotor circuitry with the emergence of exploratory whisking. *Neuron*, *77*(2), 346–360.

Tang, Y., Rampin, O., Giuliano, F., & Ugolini, G. (1999). Spinal and brain circuits to motoneurons of the bulbospongiosus muscle: retrograde transneuronal tracing with rabies virus. *Journal of Comparative Neurology*, *414*(2), 167–192.

Taubin, G., Zhang, T., & Golub, G. (1996). Optimal surface smoothing as filter design. In B. Buxton & R. Cipolla (Eds.), *Computer vision — eccv '96* (pp. 283–292). Berlin, Heidelberg: Springer Berlin Heidelberg.

Thiel, G. (1993). Synapsin i, synapsin ii, and synaptophysin: marker proteins of synaptic vesicles. *Brain Pathology*, *3*(1), 87–95.

Udvary, D. (2021). *Three-dimensional reverse engineering of neuronal microcircuits: The barrel cortex in silico* (phdthesis). Universität Tübingen.

Udvary, D., Harth, P., Macke, J. H., Hege, H.-C., de Kock, C. P., Sakmann, B., & Oberlaender, M. (2022). The impact of neuron morphology on cortical

network architecture. *Cell Reports*, *39*(2).

Ugolini, G. (1995). Specificity of rabies virus as a transneuronal tracer of motor networks: transfer from hypoglossal motoneurons to connected second-order and higher order central nervous system cell groups. *Journal of Comparative Neurology*, *356*(3), 457–480.

Ugolini, G. (2008). Use of rabies virus as a transneuronal tracer of neuronal connections: implications for the understanding of rabies pathogenesis. *Developments in biologicals*, *131*, 493–506.

Ugolini, G. (2010). Advances in viral transneuronal tracing. *Journal of neuroscience methods*, *194*(1), 2–20.

Watson, D. F. (1981, 01). Computing the n-dimensional Delaunay tessellation with application to Voronoi polytopes*. *The Computer Journal*, *24*(2), 167-172. Retrieved from https://doi.org/10.1093/comjnl/24.2.167 doi: 10.1093/comjnl/24.2.167

Welker, C. (1976). Receptive fields of barrels in the somatosensory neocortex of the rat. *Journal of Comparative Neurology*, *166*(2), 173–189.

Woolsey, T. A. (2016). Re: Woolsey ta, van der loos h. 1970. the structural organization of layer iv in the somatosensory region (si) of mouse cerebral cortex. brain res. 17: 205–242. *Brain Research*, *1645*, 22–24.

Yin, J., Shen, Y., Si, Y., Zhang, Y., Du, J., Hu, X., ... Xing, Y. (2020, 10). Knockdown of long non-coding rna sox2ot downregulates sox2 to improve hippocampal neurogenesis and cognitive function in a mouse model of sepsis-associated encephalopathy. *Journal of Neuroinflammation*, *17*. doi: 10.1186/s12974-020-01970-7

Yuste, R. (2015). From the neuron doctrine to neural networks. *Nature reviews neuroscience*, *16*(8), 487–497.

Zhang, Z. (1994). Iterative point matching for registration of free-form curves and surfaces. *International journal of computer vision*, *13*(2), 119–152.

Appendix A

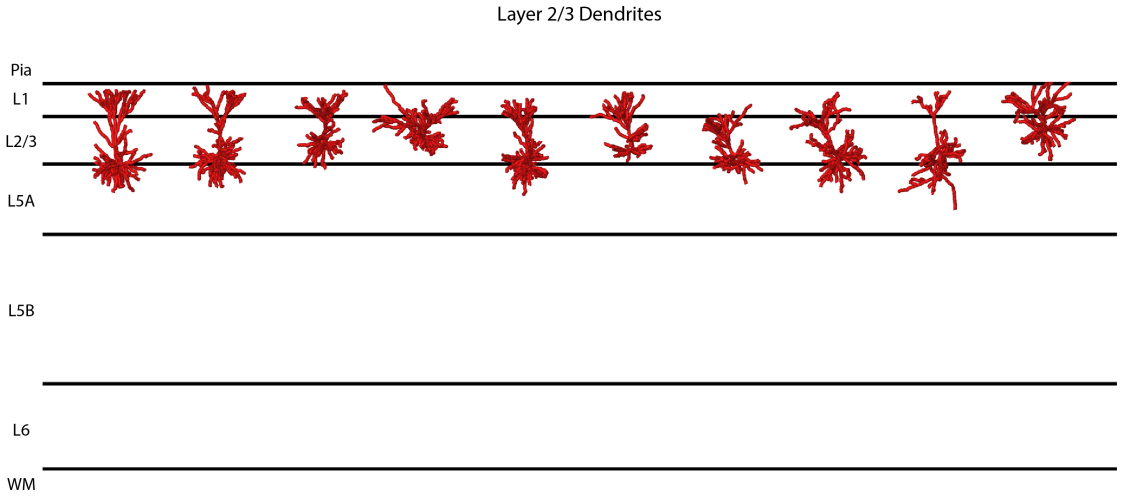

Figure A1. Gallery of vM1 registered layer 2/3 dendrites.

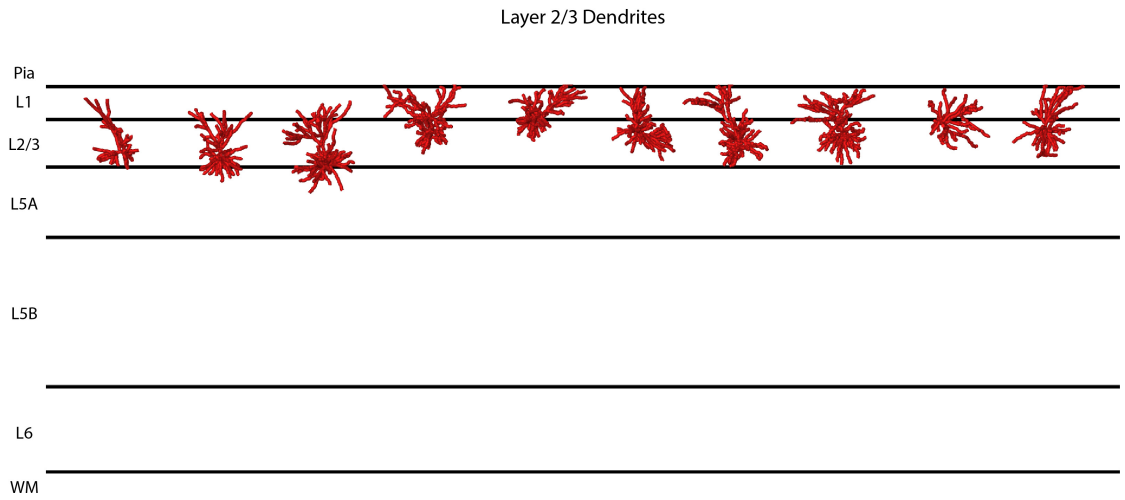

Figure A2. Gallery of vM1 registered layer 2/3 dendrites.

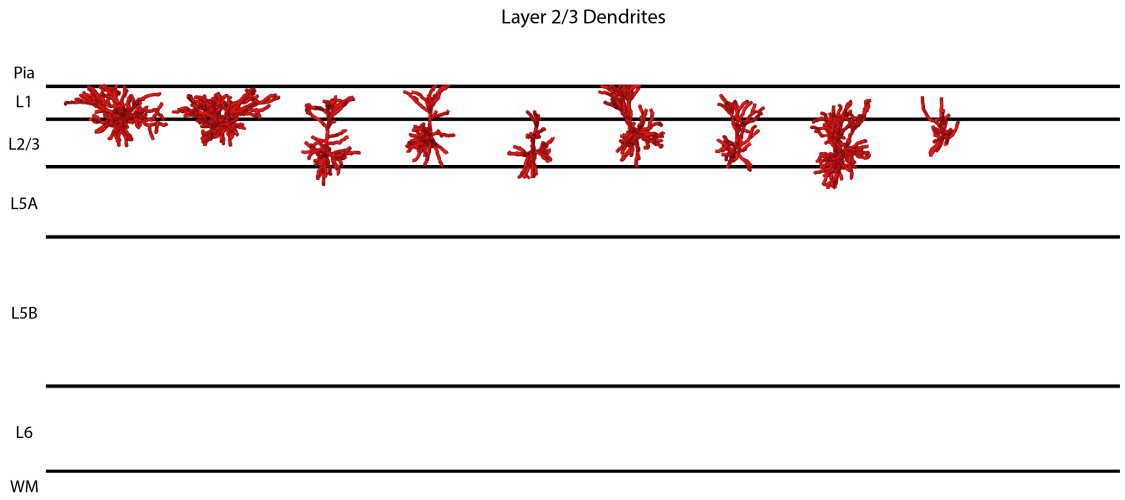

Figure A3. Gallery of vM1 registered layer 2/3 dendrites.

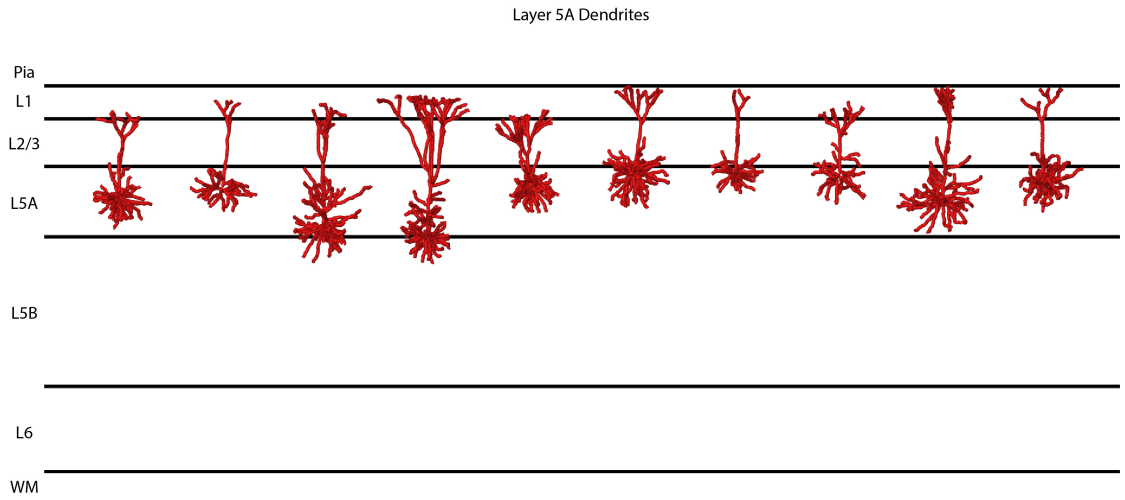

Figure A4. Gallery of vM1 registered layer 5A dendrites.

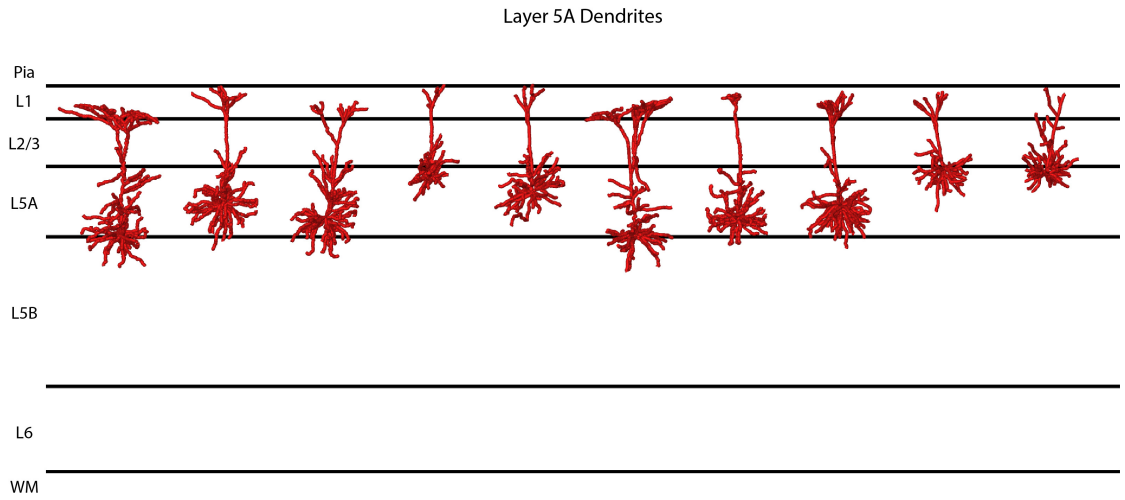

Figure A5. Gallery of vM1 registered layer 5A dendrites.

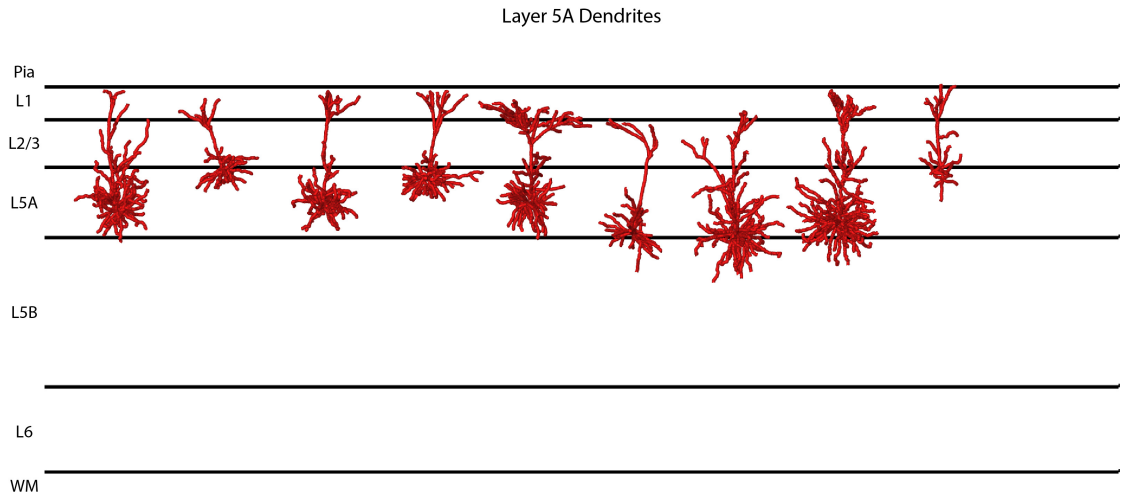

Figure A6. Gallery of vM1 registered layer 5A dendrites.

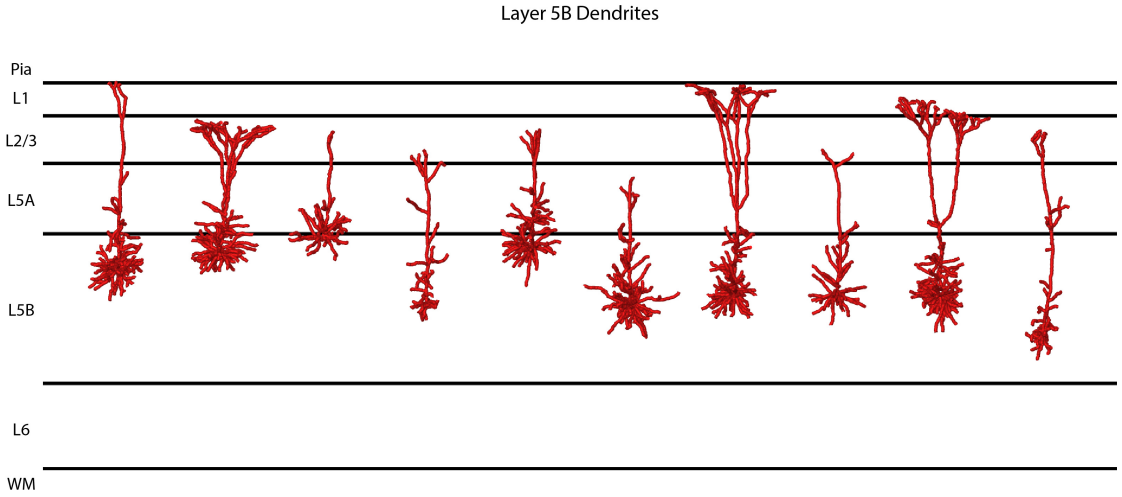

Figure A7. Gallery of vM1 registered layer 5B dendrites.

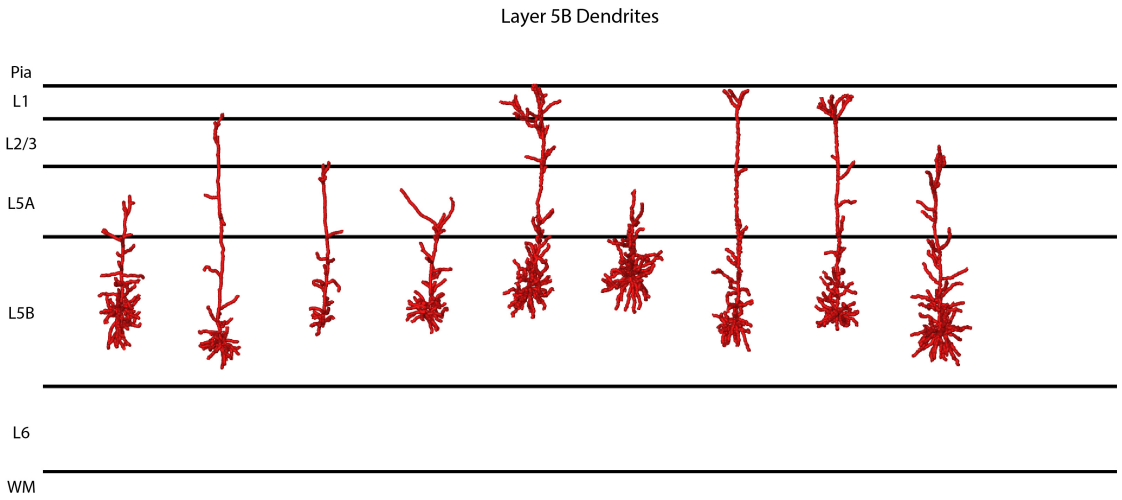

Figure A8. Gallery of vM1 registered layer 5B dendrites.

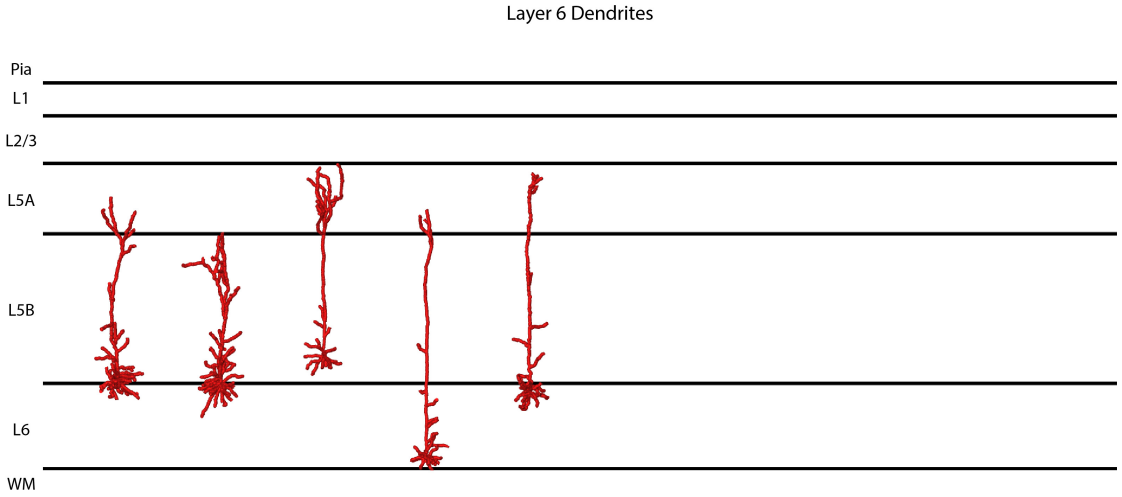

Figure A9. Gallery of vM1 registered layer 6 dendrites.